ERDA/JPL 954355/76-11
Distribution Category UC-63

Mobil Tyco Solar Energy Corporation
16 Hickory Drive
Waltham, Massachusetts 02154

LARGE AREA SILICON SHEET BY EFG

by

A. D. Morrison, K. V. Ravi, C. V. Hari Rao, T. Surek
D. F. Bliss, L. C. Garone and R. W. Hogencamp

Annual Progress Report - Subcontract No. 954355

Covering Period: October 29, 1975 - September 30, 1976

September 15, 1976

"This work was performed for the Jet Propulsion Laboratory, California Institute of Technology, under NASA Contract NAS7-100 for the U. S. Energy Research and Development Administration, Division of Solar Energy.

The JPL Low Cost Silicon Array Project is funded by ERDA and forms part of the ERDA Photovoltaic Conversion Program to initiate a major effort toward the development of low-cost solar arrays."

BIBLIOGRAPHIC DATA SHEET	1. Report No. ERDA/JPL 954355/76-11	2.	3. Recipient's Accession No.
4. Title and Subtitle LARGE AREA SILICON SHEET BY EFG			5. Report Date 15 Sept. 1976 6.
7. Author(s) A.D. Morrison, K.V. Ravi, C.V. Hari Rao, T. Surek D.E. Bliss, L.C. Carone and R.W. Hogencamp			8. Performing Organization Rept. No. C-500
9. Performing Organization Name and Address Mobil Tyco Solar Energy Corporation 16 Hickory Drive Waltham, Massachusetts 02154			10. Project/Task/Work Unit No. 11. Contract/Grant No. NAS7-100 ERDA/JPL 954355/76-11
12. Sponsoring Organization Name and Address Jet Propulsion Laboratory 4800 Oak Grove Drive Pasadena, California 91103			13. Type of Report & Period Covered Annual - 29 Oct. 1975 - 30 Sept. 1976 14.

15. Supplementary Notes

16. Abstracts

At the end of one year the program is on schedule. EFG ribbon growth system JPL No. 2 is being used to perform meaningful growth rate and ribbon thickness experiments. The new, wide ribbon growth system is in operation. A theoretical study of stresses in ribbons is reported. EFG ribbons have been observed to exhibit a characteristic defect structure which is orientation dependent in the early stages of growth.

17. Key Words and Document Analysis. 17a. Descriptors

Solar cells
Silicon
EFG crystal growth

17b. Identifiers/Open-Ended Terms

Solar generation of electricity
Continuous growth of silicon ribbons

17c. COSATI Field Group

18. Availability Statement	19. Security Class (This Report) UNCLASSIFIED	21. No. of Pages 107
	20. Security Class (This Page) UNCLASSIFIED	22. Price

ABSTRACT

At the end of one year the program is on schedule. EFG ribbon growth system JPL No. 2 is being used to perform meaningful growth rate and ribbon thickness experiments. The new, wide ribbon growth system is in operation. A theoretical study of stresses in ribbons is reported. EFG ribbons have been observed to exhibit a characteristic defect structure which is orientation dependent in the early stages of growth.

Table of Contents

SECTION	PAGE
ABSTRACT	iii
INTRODUCTION	1
TECHNICAL DISCUSSION	3
Apparatus	3
Thermal Profiles and Thermal Stresses in the Growth of Ribbon Crystals	11
Thin Ribbon Growth	54
Characterization	59
Problems	93
Plans	93
REFERENCES	95
APPENDICES	99

List of Illustrations

Figures		Page
1	'Thin/fast' EFG ribbon growth system	4
2	'Wide ribbon' growth system JPL No. 1	6
3	JPL No. 1 water jacketed horizontal growth chamber	7
4	JPL No. 1 growth chamber	8
5	(a) Quartz 'trough shaped' crucible and graphite crucible, (b) JPL No. 1 control console	9
6	(a) x/y/ϕ pull head with microswitch push and pull protection, (b) Die holder-thermal trimmer cartridge	10
7	(a) Portion of buckled ribbon showing ripples on ribbon surface. (b) Portion of scribed and split ribbon with a residual stress of ~7000 psi	13
8	Schematic of thermal expansion of adjacent longitudinal elements of the ribbon	15
9	Thermal model used in the calculation of the vertical temperature profile in the ribbon	18
10	Calculated vertical temperature profiles in ribbon for radiation into 0° K environment	20
11	Typical examples of hot and cold afterheater blocks	22
12	Temperature profile in ribbon for hot afterheater block	24
13	Temperature profile in ribbon for cold afterheater block	25
14	Coordinate system used in the calculation of thermal stress in the ribbon	29

List of Illustrations (continued)

Figures		Page
15	Vertical temperature profile in ribbon for radiation into 0^0 K environment	34
16	Thermal stress component σ_{xx} in the ribbon for radiation into a 0^0 K environment	35
17	Thermal stress component σ_{yy} in the ribbon for radiation into a 0^0 K environment	36
18	Thermal stress component σ_{xy} in the ribbon for radiation into a 0^0 K environment	37
19	Finite element grid for numerical calculation of the thermal stress in the ribbon	43
20	Shapes of the solid-liquid interface and die top in EFG ribbon growth	48
21	Cooling/afterheating block for fast, stress-free ribbon growth	52
22	(a) SiC growth at the bottom of the die. (b) Carbide layer and infiltrated zone in one capillary wall	57
23	A typical used die showing the effective increase in t_d due to SiC crystal growth	58
24	Die top during ribbon growth	60
25	Ribbon thickness vs. meniscus height	62
26	Ribbon thickness vs. meniscus height	63
27	Ribbon thickness vs. meniscus height	64
28	Schematic of twinning in diamond cubic structure	66
29	Dislocation arrays between twin boundaries	68
30	Schematic of principal twin systems in silicon	72
31	Laue photographs of ribbon two feet from seed	73
32	Electron channeling patterns from 'equilibrium' structure	74
33	Orientation of ribbons grown from various seed orientations	75

List of Illustrations (continued)

Figures		Page
34	Structure of ribbon near (111) [110] seed	76
35	Structure of ribbon near (111) [211] seed	77
36	Structure of ribbon near (110) [211] seed	79
37	Structure of ribbon near ribbon seed	80
38	Primary twins in ribbon near (111) [110] seed	81
39	Secondary electron and EBIC images of a solar cell	83
40	Secondary electron and EBIC images of linear boundaries	84
41	Schematic of spreading resistance measurement	88
42	Carrier concentration in ribbon grown from unbaked graphite components	89
43	Carrier concentration in ribbon grown from baked graphite components	90
44	Effect of solar cell fabrication on carrier concentration in ribbon	91
45	Correlation between carrier concentration and defect structure	92
46	Correlation between carrier concentration and electrical activity of defects	94
47	Pedestal base	101
48	Susceptor shell	102
49	Die holder plug	103
50	Die holder	104
51	Quartz crucible (short)	105
52	Notched cold shoes	106
53	Cooled graphite block	107

List of Tables

Tables		Page
I	Maximum Ribbon Growth Rate as a Function of Ribbon Thickness	21
II	Maximum Shear Stress (in kg/mm^2) as a Function of Position in the Ribbon, and Temperature and Yield Stress as a Function of Vertical Distance	39
III	Resolved Shear Stresses for (111) $[11\bar{2}]$ Ribbon Growth	40
IV	Stress Relaxation Times as a Function of Temperature for Various Activation Energies	49
V	Meniscus Height Versus Ribbon Thickness	61
VI	Expected Ribbon Surface Orientations and Growth Directions after Twinning	70

I. INTRODUCTION

The objectives of this program are to produce at high speed, thin, wide sheets of silicon of the quality needed to fabricate 10% efficient solar cells. This is part of a total Mobil Tyco Solar Energy Corporation objective to produce silicon ribbon for solar cells at a cost which will allow their wide scale use for generation of electrical power. The edge-defined, film-fed growth process was developed for the commercial production of continuous shaped single crystals of sapphire from the melt and was applied to growth of silicon ribbon for solar cells partly under NSF Grant GI37067X via Harvard University, JPL Contract 953365, and under NSF Grant GI43873. The basic feasibility of the application of EFG to the growth of silicon ribbon has been proven and the theoretical base for extending the technique to the efficient production of sheet silicon has been established.

The two major tasks in this program to produce large area silicon sheet by EFG are: the growth of thin ribbon at high speeds in existing apparatus and the design and construction of a system for the growth of wide ribbons. These two tasks will be combined toward the end of the program to achieve the ultimate program goal. Concurrent with the development of the growth process and ribbon growth apparatus will be material and solar cell characterization programs and theoretical studies of various aspects of EFG silicon sheet growth including melt replenishment, the effect of h_{eff} and aspects of heat flow in the EFG silicon growth system.

At the end of one year the program is on schedule. Work is progressing along several fronts. Details of the progress achieved in the areas of thin/fast growth, "wide" system engineering and assembly, characterization, and theoretical studies follow in the Technical Discussion.

II. TECHNICAL DISCUSSION

A. Apparatus

One major task of this program is to grow thin (~0.1 mm) silicon ribbon at high growth rates (7.5 cm/min). These goals are being pursued in a resistance heated EFG system designated JPL No. 2 (Fig. 1). The system was modified at the beginning of this program to incorporate all current state-of-the-art EFG silicon ribbon technology. This modification included planning and building of a variable top heater assembly, the design of the power supplies and controller for the new top heater assembly, the design of specific crucible holder parts and an improved crucible support pedestal assembly and a general debugging, rewiring and system alignment effort.

The final configuration of the furnace chamber is virtually indistinguishable from the growth system previously described and illustrated.[1] The puller is a ballscrew driven fixed stroke machine capable of pulling ribbon at up to 12.7 cm/min. The furnace itself is comprised of a vertical cylindrical graphite crucible heating element insulated with concentric carbon and graphite felt heat shields. Die heaters or 'trimmers' include ribbon face heaters wired in parallel and end heaters controlled independent of the face heaters and independent of one another. Molybdenum and graphite shields and the graphite fiberform package complete the top insulation. Real control of ribbon spreading and left-right temperature balance is achieved with the end heaters. All of this is packaged in a water-jacketed stainless steel furnace chamber.

To achieve the thermal gradients necessary to grow low stress ribbons at high growth rates, an afterheater is currently being designed for this growth system. The layout is nearly complete. The heater will be flexible to provide various gradients as desired.

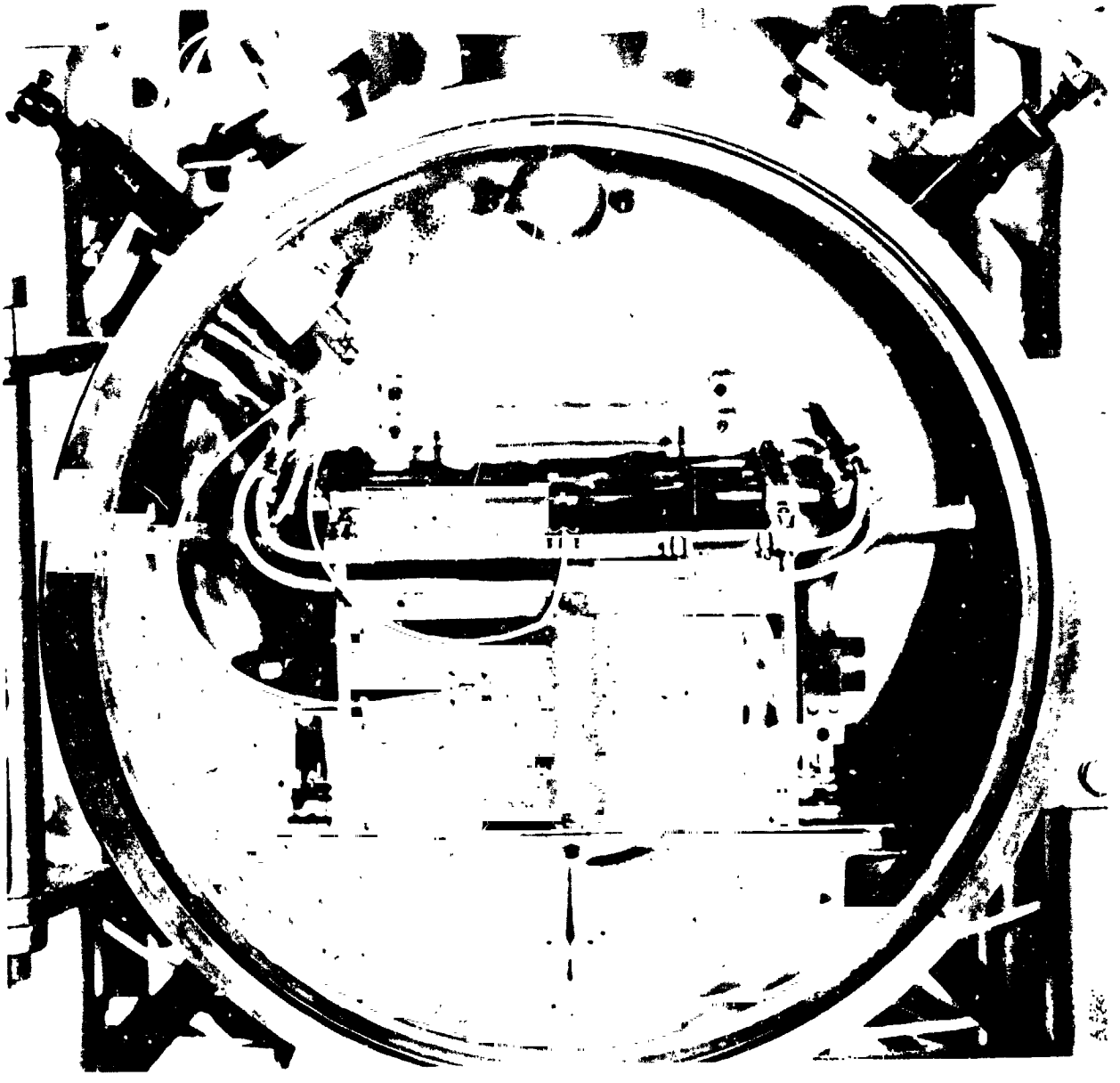

Fig. 1. 'Thin fast' EFG ribbon growth system, JPL No. 2 (from Ref. 1).

A new ribbon growth system, designated JPL No. 1 is designed to have the capacity to produce 125 cm long, 7.5 cm wide, 0.1 mm thick silicon ribbon at speeds of up to 7.5 cm/min. Experience with JPL No. 2 has contributed substantially to the design of JPL No. 1. We expect that new thin fast/growth technology developed on JPL No. 2 will contribute to experiment planning on the new machine as well.

JPL No. 1 was operational before the end of this reporting period (Fig. 2). It is comprised of three elements; the puller, the furnace chamber, and the electrical system. The puller is a 192 cm fixed stroke dovetailed slid with saddles which are ballscrew driven. The screw is driven by a closed loop controlled torque motor. The furnace chamber is a horizontal, water-jacketed, stainless steel (Fig. 3) can containing concentric semicylindrical molybdenum and tungsten heat shields (Fig. 4), high purity graphite heating element and crucible holder, and trough shaped quartz crucibles (Fig. 5a). The horizontal furnace geometry was selected so that the geometry of the physical system and of the thermal gradients more closely approximate the geometry of the product. The power is supplied to the main heating element from an SCR controlled 25 kW transformer. Independently controlled die heater/trimmers and an active afterheater are powered by an additional 10 kW supply (Fig. 5b).

Though simple and dependable, the resulting system should be flexible enough to accommodate the host of experimental variables including 2.5 to 7.5 cm wide ribbon growth at speeds up to 7.5 cm/min as well as supplementary studies including continuous melt replenishment.

The JPL No. 1 design and procurement efforts of the first three quarters of this year have been reported. During the last quarter all the major components were received and assembled. Details and debugging have been attended to. A seed holder was designed (Fig. 6a), radiation shields for the windows, water-cooling for top and bottom flanges and puller slide protection circuits have been designed and installed. SCR firing circuit and temperature controller malfunction have been repaired. The main heating element has been heated up to 1800°C. Heat shield warping observed has been minimized by adding tungsten nuts and bolts and spacers. The die holder/gradient controlling cartridge was assembled (Fig. 6b).

The system has been run up past 1400°C repeatedly. Temperatures inside the shield package are essentially uniform. Except for the ends of the molybdenum bolts, the outside of the shield package never exceeds ~ 350°C. A 300 g silicon charge was melted using less than 30% of the available 25 kW power. The third growth attempt yielded ribbon ~4.6 cm wide using less than 15 kW in the main heater, die heaters, and afterheaters total.

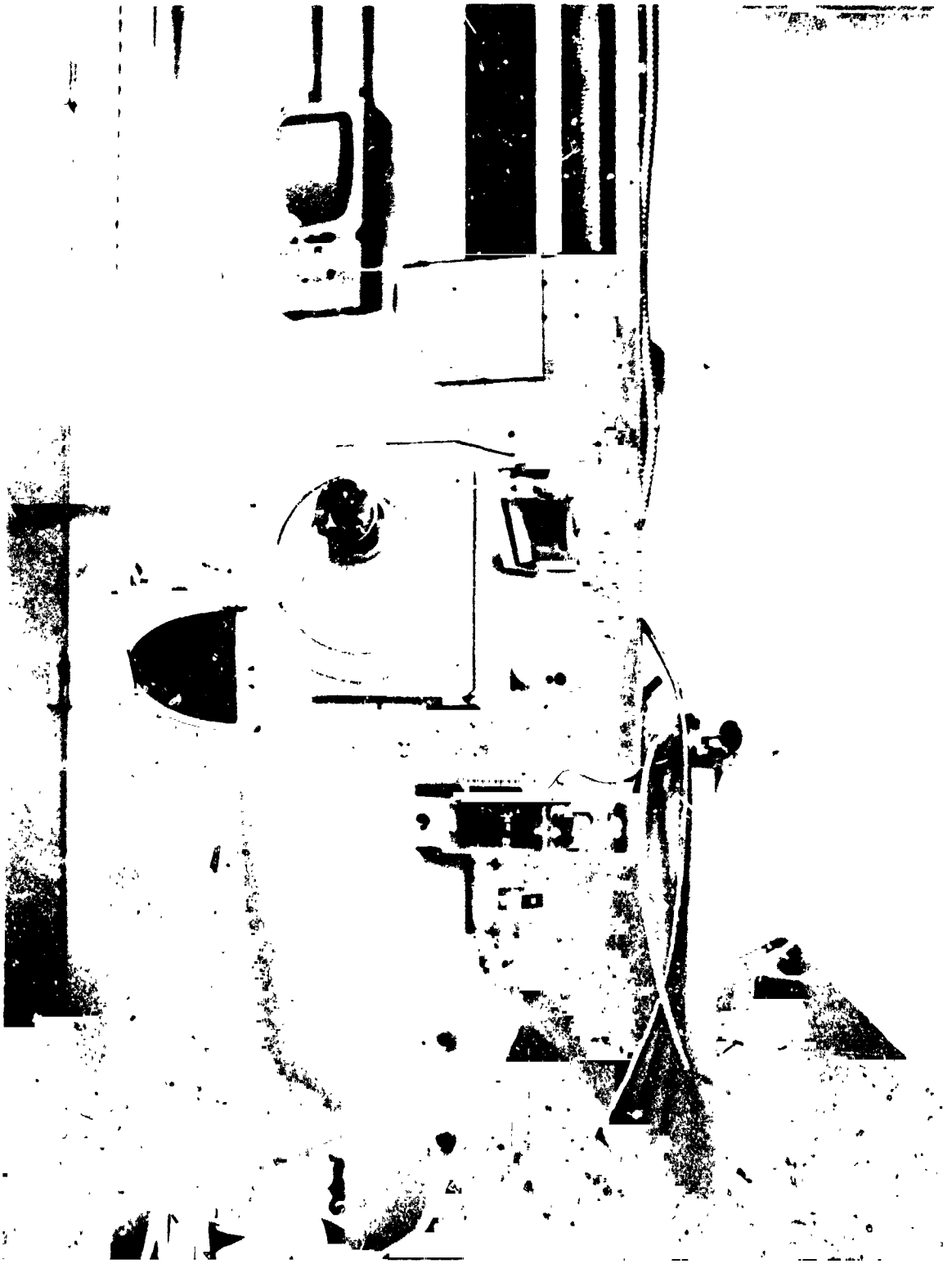

Fig. 2. 'Wide ribbon' growth system JPL No. 1 showing chamber, slide saddles, and torque motor drive.

Fig. 3. JPL No. 1 water jacketed horizontal growth chamber; torque motor drive and control console are seen at left and right, respectively.

Fig. 4. JPL No. 1 growth chamber showing bottom and top molybdenum shield sets.

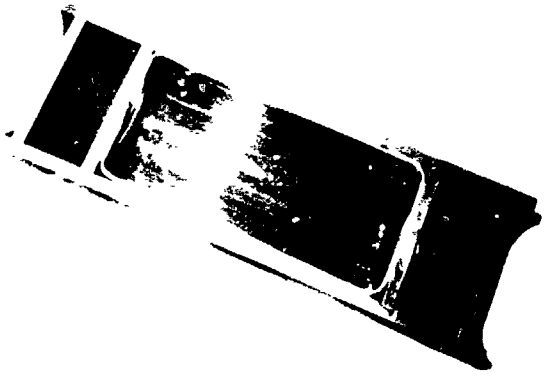

(a)

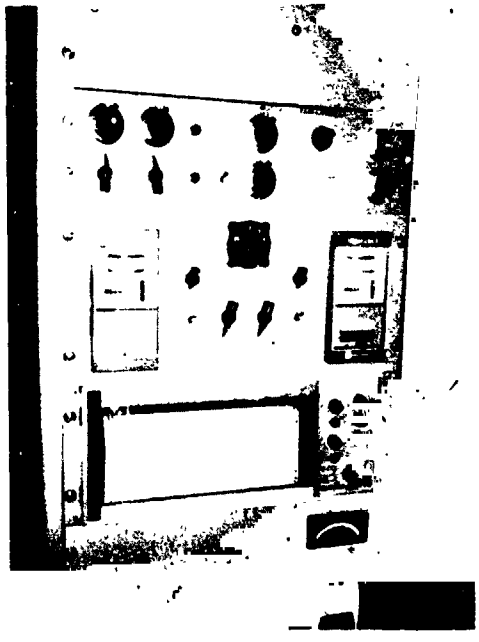

(b)

Fig. 5. (a) Quartz 'trough shaped' crucible and graphite crucible holder. (b) JPL No. 1 control console containing closed loop motor speed, afterheater, and die heater controls and power supply and main heater cortrol.

(a)

(b)

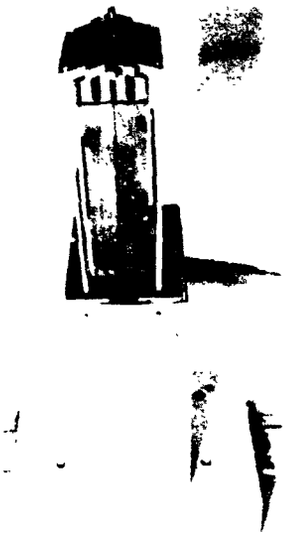

Fig. 6. (a) x/y/ϕ pull head with microswitch push and pull protection.
(b) Die holder-thermal trimmer cartridge.

B. Thermal Profiles and Thermal Stresses in the Growth of Ribbon Crystals

1. Introduction

Attempts to grow ribbon-shaped crystals of silicon from the melt by techniques such as EFG or laser recrystallization have encountered problems with residual stresses in the grown crystals. Experience with EFG silicon ribbon growth has indicated that the stress problem became worse as faster growth rates and larger ribbon widths were sought. Since increasing the growth rate and ribbon width are of primary importance in developing the EFG process to attain its full potential, we have undertaken to consider the origin of the residual stresses in ribbon-shaped crystals and to identify the parameters that determine their magnitude. The analysis described here, of course, applies equally to other sheet growth techniques of silicon from the melt such as the Inverted Stepanov technique, the Ribbon-to-Ribbon process by laser recrystallization, and web-dendritic growth; research on these techniques (as well as on EFG ribbon growth described here) is being currently sponsored by the Jet Propulsion Laboratory.[2]

An identification of the origin of the residual stresses is made in Section II.B.2; it is indicated that the stresses result from the plastic deformation which the crystals undergo at the high temperatures. The plastic deformation, in turn, is caused by the thermal stresses which arise as a result of non-uniform temperature distributions in the ribbon. The problem of thermal profiles in ribbon-shaped crystals is considered in Section II.B.3. The most useful approach to determining the temperature distribution in the ribbon turns out to be numerical modelling on the computer; the model permits close interaction between the theoretical calculations and the design of experimental hardware. In Section II.B.4, we apply thermoelasticity theory to predict the effects of the thermal profile on the thermal stresses in ribbon-shaped crystals. Of basic concern here are the two interrelated problems: one is to minimize the extent of plastic deformation and, therefore, the strain induced imperfections, the other is to reduce, to a tolerable level, the residual elastic stress in the crystal when it reaches room temperature. Various experimental approaches which are being undertaken to solve the thermal stress problem in EFG ribbon growth are discussed in Section II.B.4.d; a recent strategy which can lead to a minimization of both the plastic strain and the residual stress is also described. An oral version of the following text was presented[3] at a seminar sponsored by the Jet Propulsion Laboratory.

2. Origin of the residual stress

It is worthwhile to review here briefly some basic concepts concerning residual stress in crystalline materials. Residual stress is a stress system satisfying internal equilibrium with no external loads or temperature gradients; it is accompanied by an elastic strain distribution in the material. On a microscopic scale, residual stress is associated with the microstructure of the material such as dislocations, inclusions, deformation twins, and dislocation pile-ups; these residual stresses are short range, but the defects play a fundamental role in plastic deformation and in fracture of the material and in its electrical properties. Residual stresses on a macroscopic scale can be caused by mechanical effects (e.g., forced alignment of parts, or loads causing non-uniform plastic flow or creep), by thermal effects (e.g., thermal stress due to non-uniform changes in temperature causing plastic flow), and by chemical or compositional effects. The present analysis is concerned with the thermal stress in the growth of ribbon-shaped crystals, i.e., with the plastic strain induced imperfections and the residual stress in the grown crystal. Residual stresses can be generally relieved by small amounts of relaxation or plastic strain; if present, the stresses can cause or promote fracture, buckling, plastic flow and creep. Residual stress in silicon can be measured by X-rays or birefringence, or, more typically, by observing the strain during removal of material (e.g., by scribing and splitting the ribbon crystals and measuring the curvature after splitting[4] - see Fig. 7b).

The residual stresses we have measured in EFG silicon ribbons by such splitting technique were generally in the range 0 to 30,000 psi (the fracture stress of silicon at room temperature is approximately 80,000 psi[5]). Cutting into solar cell blanks is generally difficult if the stress exceeds ~5,000 psi; the uniformity of ribbon thickness also affects the ease of cutting. Spontaneous shattering of the ribbon during growth or handling, or excessive fracture during scribing is probably indicative of residual stresses in excess of 30,000 psi.

From the observed shapes of the split or buckled ribbons (see Fig. 7), we can already deduce some information on the elastic strain in the material. In essence, the ribbon is longer in a central longitudinal section than along the edges; on a microscopic scale, the length variation across the ribbon width is the result of extra half-planes of dislocations. A simple calculation of the dislocation density for a typical stress of 15,000 psi (which corresponds to a split of 0.52 in. over a ribbon length of 20 in. in a 1 in. wide ribbon) yields a density of 8×10^4 cm^{-2}. In

(a)

(b)

Fig. 7. (a) Portion of buckled ribbon showing ripples on ribbon surface.
(b) Portion of scribed and split ribbon with a residual stress of ~7000 psi.

the analysis of the thermal stress in the ribbon, we will point out how the plastic deformation during growth, in response to the thermal stress, can lead to the increase in the length at the ribbon center.

The basic question we must first consider is: what is the origin of the residual stresses in a non-uniform temperature gradient, and what are the parameters that determine their magnitude. When the ribbon is cooled from the melting point to room temperature, each portion or element of the ribbon will contract proportional to its own temperature fall. If adjacent elements contract differently, they will restrain each other's contraction, and hence stresses must result. External constraints to thermal contraction can also cause thermal stress, but this does not apply to the crystal growth situations treated here.

The effect of the temperature distribution along the ribbon length (or the "vertical" temperature profile) on the thermal stress is illustrated in Fig. 8. We consider the ribbon to consist of a number of narrower strips, as shown in Fig. 8a. If the ribbon is at a uniform temperature, the strips are parallel-sided (Fig. 8a) and there is no stress. If the ribbon is in a uniform temperature gradient, each strip tapers uniformly as a result of thermal contraction (assuming, of course, that the thermal expansion coefficient is independent of temperature). Figure 8b shows this, grossly exaggerated. Again, adjacent strips conform to each other without bending. Therefore, the ribbon is stress free, and will remain stress free as long as it is in the same temperature gradient. If the temperature gradient becomes non-uniform (i.e., non-linear), then the shape of each strip, if it were not attached to its neighbors, would be as shown in Fig. 8c. It is apparent that adjacent strips no longer conform to each other without bending; the strips can be made to fit by lateral deformation in their own plane, thus thermal stresses must arise. It is also apparent that the stress will be proportional to the curvature or bending that must be imposed to fit the strips together. The curvature is, of course, proportional to the rate of change of the temperature gradient, i.e., d^2T/dx^2, and also increases with increasing ribbon width. The explicit dependence of the thermal stress components on the derivatives of the vertical temperature profile T(x) and on the ribbon width will be derived in a later section. The important point to realize from this qualitative argument is that, in a realistic crystal growth situation, it is impossible to cool the ribbon to room temperature without developing stress in the ribbon at some point.

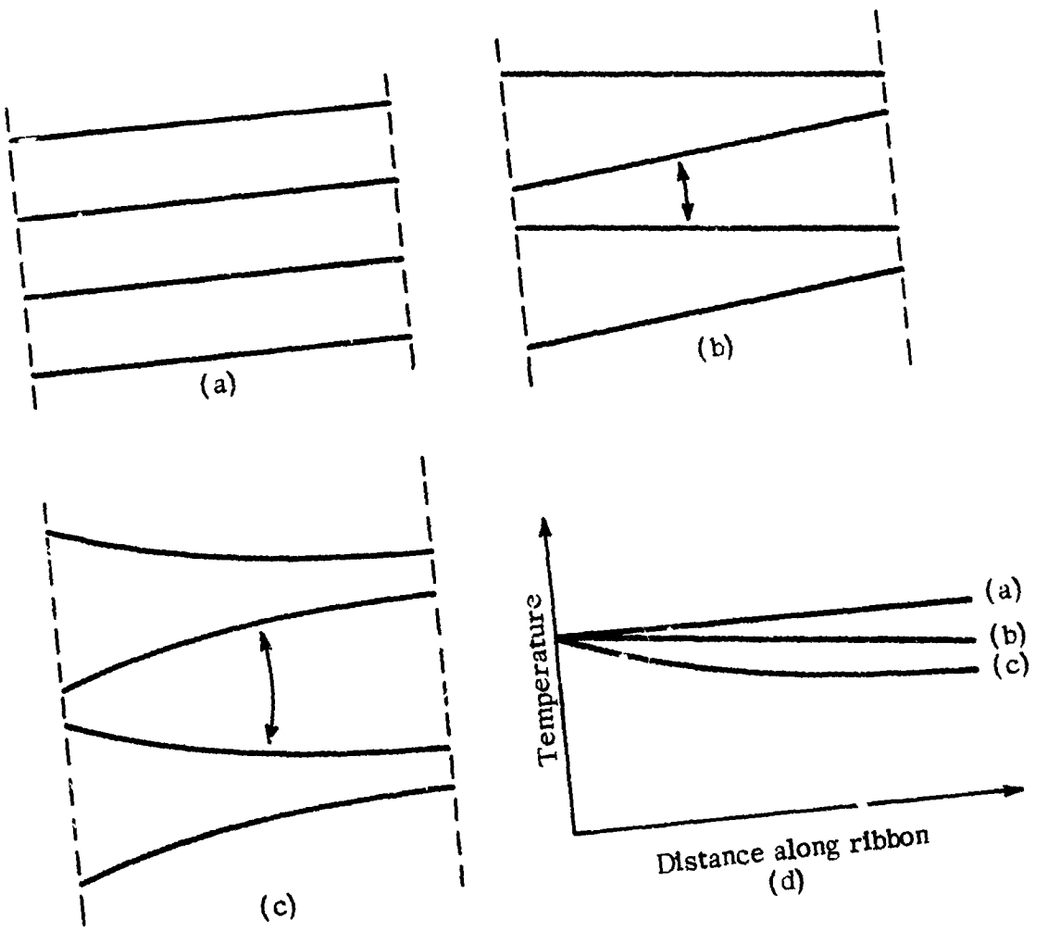

Fig. 8. Schematic of thermal expansion of adjacent longitudinal elements of the ribbon: (a) Ribbon at a uniform temperature; (b) Ribbon with linear temperature profile; (c) Ribbon with non-linear temperature profile; (d) Schematic of temperature profiles for cases (a), (b) and (c).

3. Thermal profiles in the growth of ribbon crystals

a. Analytic calculation of thermal profile

The first problem is to determine the temperature distribution in the ribbon under a variety of growth conditions. Extensive theoretical work was performed in a recently concluded NSF program[6] to obtain analytical solutions for the vertical temperature profile and to relate the ribbon thickness to the gradient in the meniscus and the growth rate. Numerical analyses of the horizontal (i.e., along the ribbon width) and transverse (i.e., through the ribbon thickness) temperature profiles were also carried out.

An analytic expression for the gradient in the vertical profile in the ribbon is given by the following:[7]

$$\frac{dT}{dx} = \left(\frac{\sigma\epsilon}{t\, k_m\, T_m}\right)^{\frac{1}{2}} \cdot \left\{T^6 - T^2\, T_o^4 \left[1 + 4 \ln (T/T_o)\right]\right\}^{\frac{1}{2}} . \qquad (1)$$

Here we have assumed that the heat flow is one-dimensional (i.e., along the vertical or x-direction), the ribbon width is much greater than the ribbon thickness (t), the thermal conductivity is proportional to 1/T, and the radiating environment seen by the ribbon is at a uniform temperature T_o.† Also, the heat carried by the moving ribbon has been neglected in calculating the steady-state temperature profile. The vertical temperature profile can be readily obtained by numerical integration of Eq. (1) with $T(0) = T_m$.

Equation (1), in conjunction with a steady-state heat balance condition at the solid-liquid interface, has been useful in relating the ribbon thickness to the growth rate and the gradient in the liquid; the effective environment temperature has been determined from correlations of experiment and theory. Other than describing the gradient at the interface, however, this analytic approach is insufficient to describe the vertical profile in the ribbon to the extent that useful determina-

† The other terms in the above expression are the Stefan-Boltzmann constant σ, the emissivity of the ribbon surface ϵ, and the thermal conductivity of solid silicon k_m at the melting temperature T_m.

tions of the thermal stresses can be made. The main problems are the oversimplification of the radiating environment and the assumption of a stationary ribbon in the analytic calculations. The inclusion of a more realistic thermal environment (which can also be readily correlated to the crystal growth setup) and of the specific heat transport in the ribbon into the solution must perforce involve numerical analysis on the computer. The remainder of this section describes a computer model developed on a previous Mobil Tyco funded program, and examines the predictions of this model relating to the current program's objectives of fast, wide and stress-free ribbon growth.

b. Numerical calculation of thermal profile

Figure 9a depicts schematically the geometry used in the numerical calculation of the temperature profile. Again, only one-dimensional heat flow is considered, i.e., the profile along the vertical (or crystal pulling) axis of the ribbon is calculated. The afterheater block dimensions x_B (height above the interface) and y_B (distance from ribbon surface), and the environment temperatures below, along and above the block are variable; a maximum of 10 temperature values can be specified along the afterheater. The steady-state temperature is calculated at 40 equally spaced incremental points along the ribbon; the length L, thickness and growth rate of the ribbon are variables in the program.

The model considers conductive and convective heat transport in the ribbon, and radiative and convective cooling at the ribbon surface. The heat balance condition for the ith element in the ribbon is given by (see Fig. 9b):

$$wt\left[k_i\left(\frac{T_{i-1}-T_i}{\Delta x}\right) - k_{i+1}\left(\frac{T_i - T_{i+1}}{\Delta x}\right)\right] + \rho\, CV_g\, wt\left[\left(\frac{T_i + T_{i-1}}{2}\right) - \left(\frac{T_{i+1}+T_i}{2}\right)\right]$$
$$- 2\Delta x\,(w+t)\cdot\left[Q_i^{RAD} + Q_i^{CONV}\right] = 0 \quad . \qquad (2)$$

In the above expression, w is the ribbon width, C is the specific heat of solid silicon, V_g is the crystal growth rate, and $k_i = 2\,k_m\,T_m/(T_i + T_{i-1})$ is the average thermal conductivity for the i^{th} and $(i-1)^{th}$ elements. The radiative heat loss from the i^{th} element (Q_i^{RAD}) is a function of T_i and ϵ, and of the emissivities, temperatures and angle factors of the surfaces which comprise the environment (i.e., the afterheater block). The convective heat loss from the i^{th} element is given by $Q_i^{CONV} = h\,(T_i - T_g)$, where $h = Nu \cdot k_g/y_B$ is the heat transfer coefficient, T_g is the effective gas temperature at the i^{th} element (assumed to be intermediate to T_i and the after-

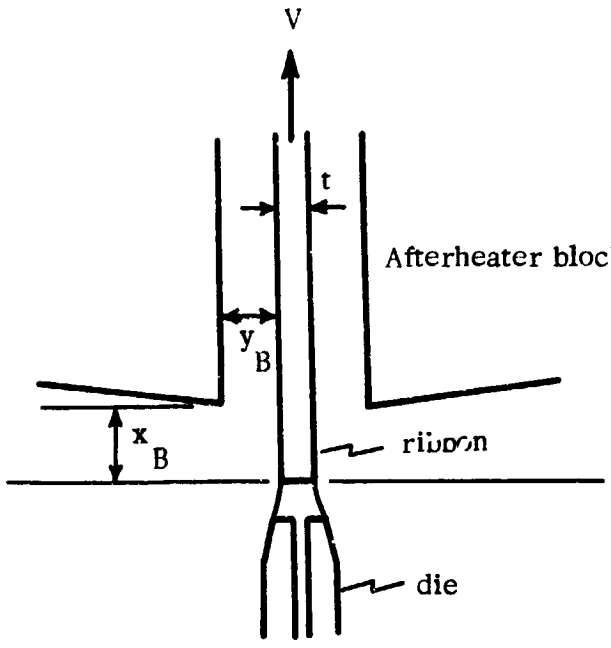

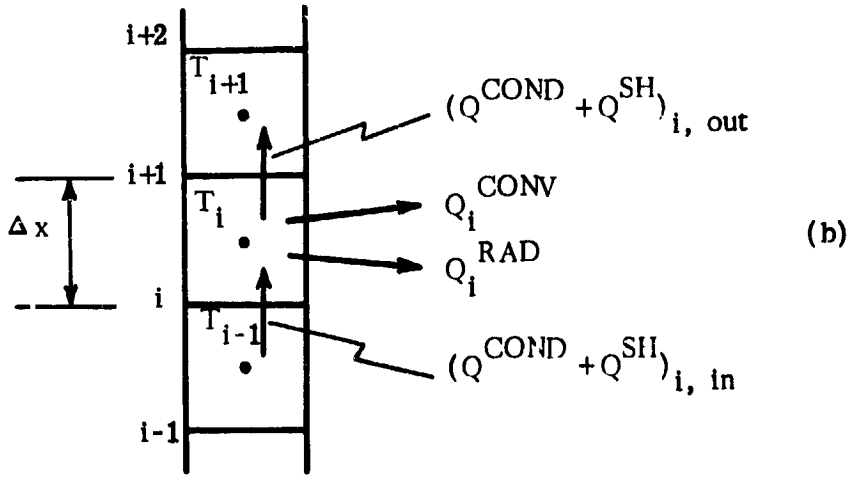

Fig. 9. (a) Schematic of thermal model used in the calculation of the vertical temperature profile in the ribbon. (b) Heat flow terms at the i^{th} element in the ribbon (Q^{COND} = conductive heat, Q^{SH} = specific heat convection, Q^{CONV} = gas convection heat loss, Q^{RAD} = radiative heat loss).

heater temperature at that point), k_g is the thermal conductivity of the gas phase,† and Nu is the Nusselt number for the convective heat transfer. Based on some heat transfer calculations,[9] a value of Nu = 6 has been used in most of the calculations; in essence, the heat loss is assumed to be ~6 times that by straight conduction through the gas. The convective heat is not actually carried away by the flowing gas; rather, there is a heat exchange between the ribbon and the afterheater block at each point. The Nusselt number is clearly an adjustable parameter in the calculations; its appropriate value for a given growth system should be obtainable from experimental measures of the thermal profiles and comparison to theory.

The boundary conditions to the numerical calculations are that the interface temperature $T(0) = T_m$, and that the temperature at the cold end of the ribbon $T(L) = T_e$ = constant. Fixing the cold-end temperature allows one to obtain a convergent solution more rapidly; the effects of T_e on the vertical profile are readily examined in the model. The numerical solution uses the Gauss-Seidel technique with accelerated relaxation; a converged solution is found after approximately 100 iterations.

The output of the numerical calculations includes a graphical printout of the temperature profile and a prediction of the maximum growth rate for the given "experimental" conditions. The temperature values at the incremental points can be directly input into a numerical program which calculates the thermal stress in the ribbon. Some examples of the calculated profiles will be given in the following to show the effects of specific heat transport in the ribbon and the effectiveness of gas cooling of the ribbon surface.

c. Effect of specific heat transport

A significant refinement to the earlier analysis[6,7] which gave Eq. (1) has been the inclusion of the specific heat carried by the moving ribbon into the numerical calculation of the vertical temperature profile. The effect of this term on the thermal profile turns out to be quite important, as illustrated in Fig. 10. Fig. 10a shows the temperature distribution in a stationary ($V_g = 0$) ribbon 4 cm long, 0.025 cm (~10 mils) thick for radiation into a 0°K environment, whereas Fig. 10b is the steady-

†The temperature dependence of the gas thermal conductivity (e.g., Ref. 8) has been accounted for in the calculations.

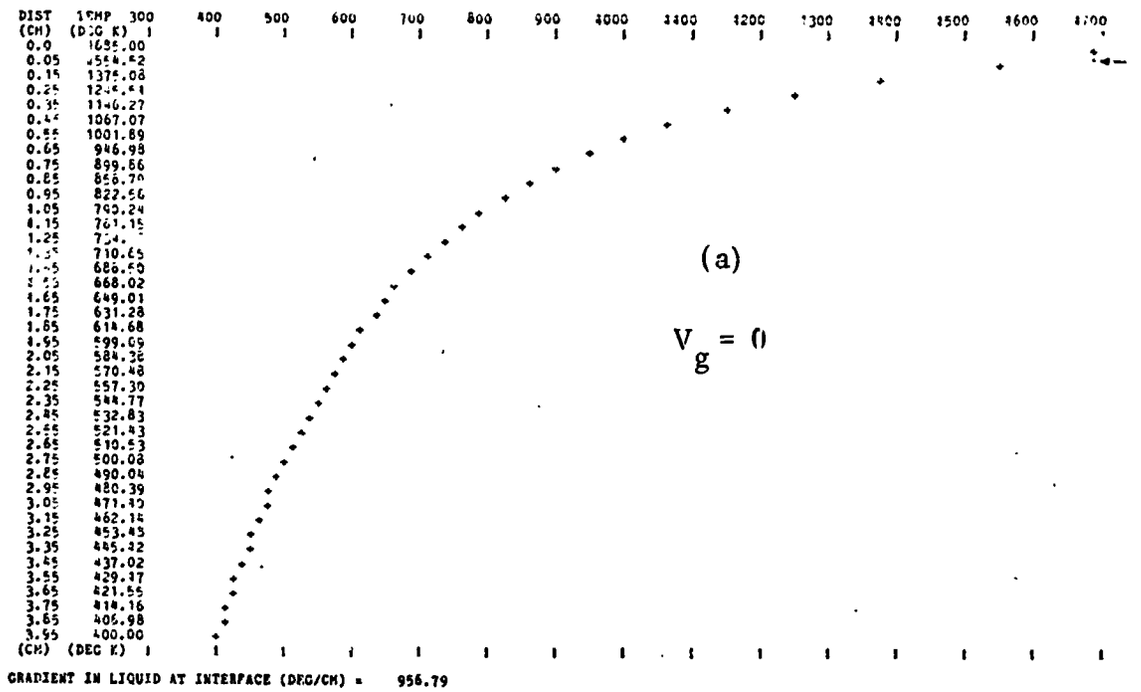

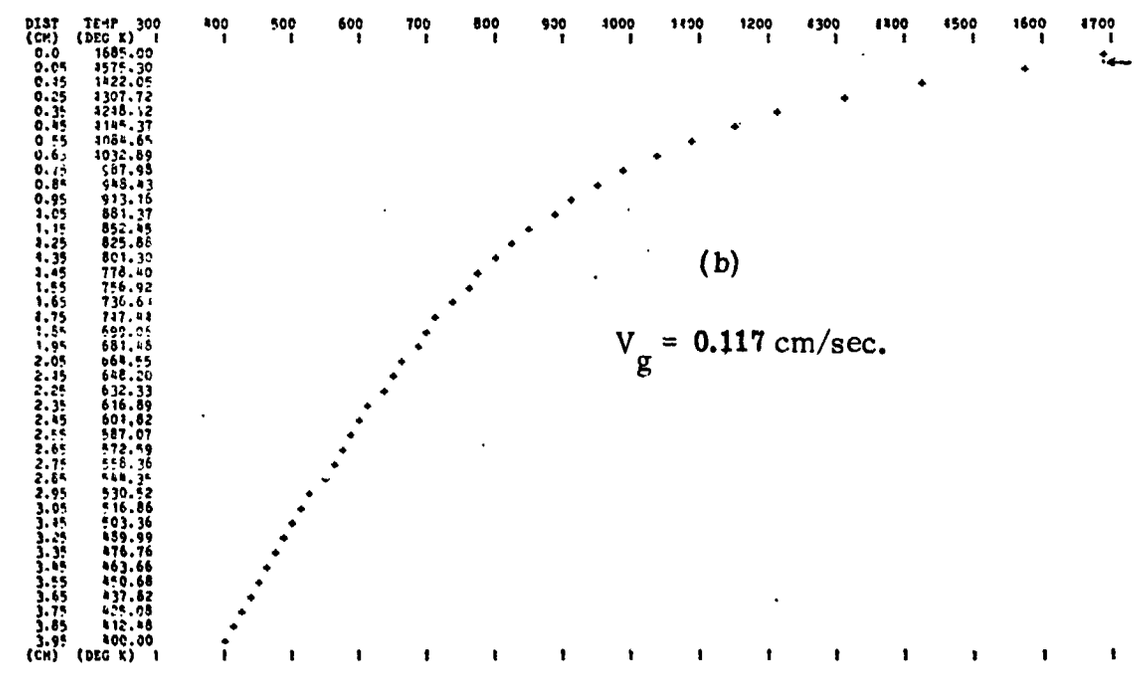

Fig. 10. Calculated vertical temperature profiles in a 0.025 cm thick, 4 cm long ribbon for (a) $V_g = 0$ and (b) $V_g = 0.117$ cm/sec. The convective heat transport is included in the calculations. Radiation into a $0^{\circ}K$ environment is assumed; the temperature at the far end of the ribbon is fixed to $400^{\circ}K$. The arrow denotes the position of the growth interface on the printout.

state profile for a ribbon growing at 0.117 cm/sec (~2.76 in./min). The latter rate corresponds to the condition where the gradient in the liquid is approximately zero, and is therefore the maximum ribbon growth rate for a 0.025 cm thick ribbon. The previous theory[6, 7] which neglects the convective heat transport predicts, on the other hand, that the maximum growth rate is 0.146 cm/sec. Table I lists the values of the maximum growth rate as a function of ribbon thickness based on the earlier theory and on the current numerical calculations. The latter values are seen to be approximately 20% lower in each case. The same result is obtained for cases where the environment temperature is different from 0°K; the maximum growth rates based on the thermal profiles in the stationary ribbon (i.e., $V_g = 0$) are typically 10 to 20% higher than the rates obtained from the actual profiles in the moving ribbon.

Table I. Maximum Ribbon Growth Rate as a Function of Ribbon Thickness

t (cm)	$(V_g)_{max}$, cm/sec (using Eq. (16) in Ref. 7)	$(V_g)_{max}$, cm/sec (corrected value)*
0.01	0.231	0.179
0.02	0.163	0.130
0.025	0.146	0.117
0.03	0.133	0.107
0.04	0.116	0.094
0.05	0.103	0.084

*The corrected value is obtained by numerical solution of the steady-state temperature profile; the model includes the convective heat transport (i.e., specific heat) by the moving ribbon. Radiation into a 0°K environment is assumed.

d. Effects of afterheater block and gas cooling

The effectiveness of the heat exchange between the ribbon surface and the afterheater block can be best illustrated by some specific examples. Figure 11a shows schematically a typical "hot" afterheater block configuration. The hot portion of the block (1 cm in length) has a linear temperature gradient from 1300°K to 1000°K; the temperatures below and above the block are 1300°K and 500°K, respectively. The

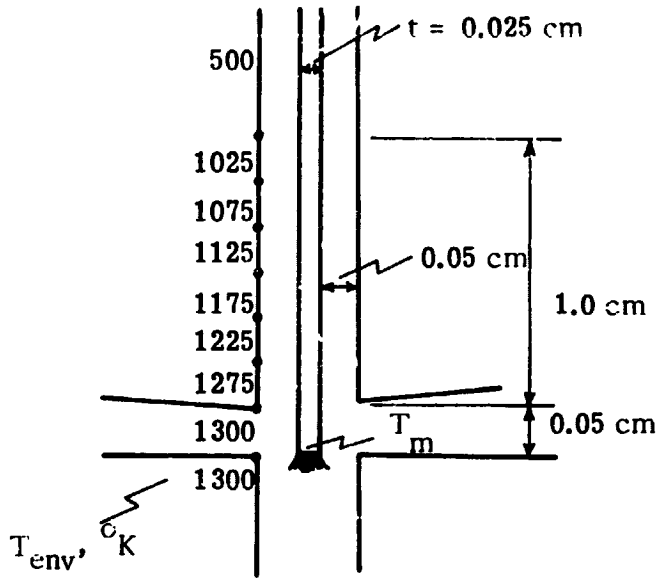

(a)

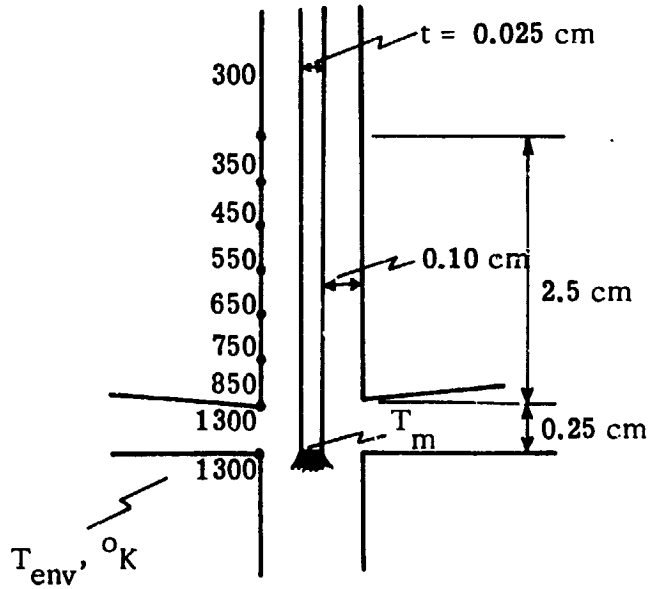

(b)

Fig. 11. Typical examples of hot (a) and cold (b) afterheater blocks. The thermal environment of the ribbon is determined by the positioning of the block with respect to the ribbon and the growth interface, and by the temperature values below, along and above block.

block is located 0.05 cm (~20 mils) from the ribbon surface on either side and 0.05 cm above the growth interface. The temperature profile in a 0.025 cm thick ribbon at zero growth rate is shown in Fig. 12a for the case where heat exchange between the ribbon and the afterheater is by radiation only (i.e., no gas cooling or heating). Figure 12b shows the profile for combined radiation and argon gas cooling. The tendency of the profile to be more linear within the block in the argon case is readily apparent from the figures. From the zero growth rate profiles in Fig. 12, one can obtain an estimate for the maximum growth rates in these systems (for a 0.025 cm thick ribbon). The values are found to be 2.36 in./min and 3.08 in./min for the no-gas and argon cases, respectively; using helium as the heat exchange medium, one obtains a maximum growth rate of 5.79 in./min (as explained earlier, the actual maximum rates are about 10 to 20% lower than the above values as a result of the convective heat transport in the ribbon).

An example of a typical "cold" afterheater block is shown in Fig. 11b. Here the block is assumed to have a gradient of 240°K/cm over a 2.5 cm length. The block is located 0.25 cm above the growth interface and 0.1 cm from the ribbon surface. Temperature values below and above block are 1300°K and 300°K, respectively. The temperature profiles in a 0.025 cm thick ribbon are shown in Figs. 13a and 13b for no gas and helium, respectively. In the latter case, the profile in the ribbon is seen to attain the linear profile in the block over the last 2 cm of the block. The maximum growth rates from these $V_g = 0$ profiles are estimated to be 2.70 in./min, 3.20 in./min and 4.90 in./min for no gas, argon, and helium, respectively.

The important outcome of this numerical analysis is that we have a means of manipulating the thermal profile within the ribbon, which is important insofar as the control of the thermal stresses. Clearly, there can be a direct correlation made between these calculations and the design of the experimental hardware. The effects of heat exchange between the ribbon and the block via a gas phase were demonstrated by the above examples; means of controlling the profile by varying the gas composition, for example, are also apparent. From the growth rates predicted for the afterheaters in Fig. 11, it is felt that the program objective of 3 in./min growth rate should be readily achieved using relatively simple cooling designs. The numerical program allows one to consider trade-offs between the growth rate and the thermal profile desired for low stress. Of course, the theoretical calculations must be reinforced with experimental measures of growth rates, thermal profiles and the boundary conditions which enter the thermal model.

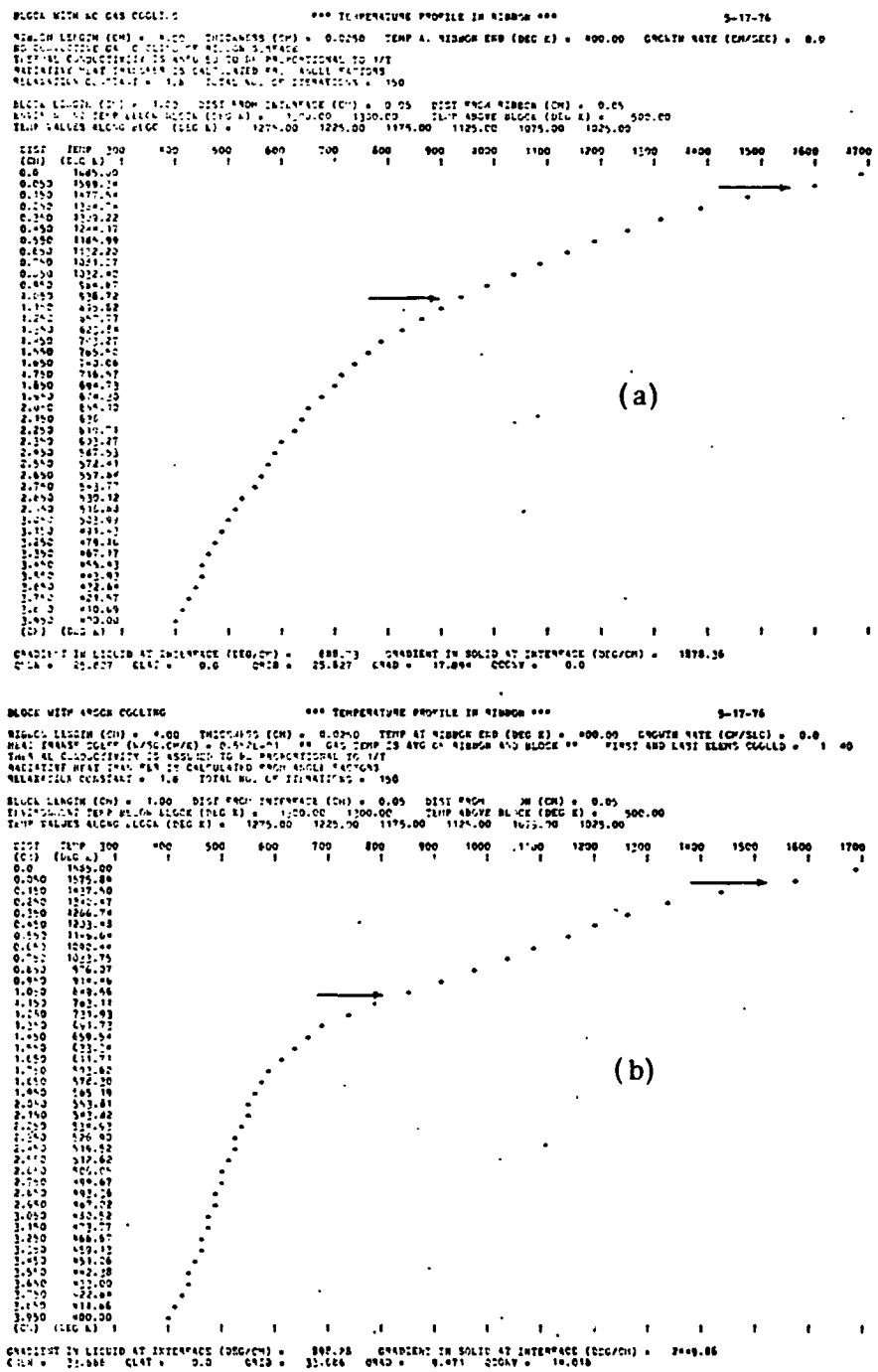

Fig. 12. Temperature profile in a 0.025 cm thick ribbon at zero growth rate for the hot afterheater block in Fig. 11a. (a) Heat loss by radiation only (i.e., no gas); (b) Heat loss by radiation and convection through argon. The arrows denote position of the block ralative to the profile.

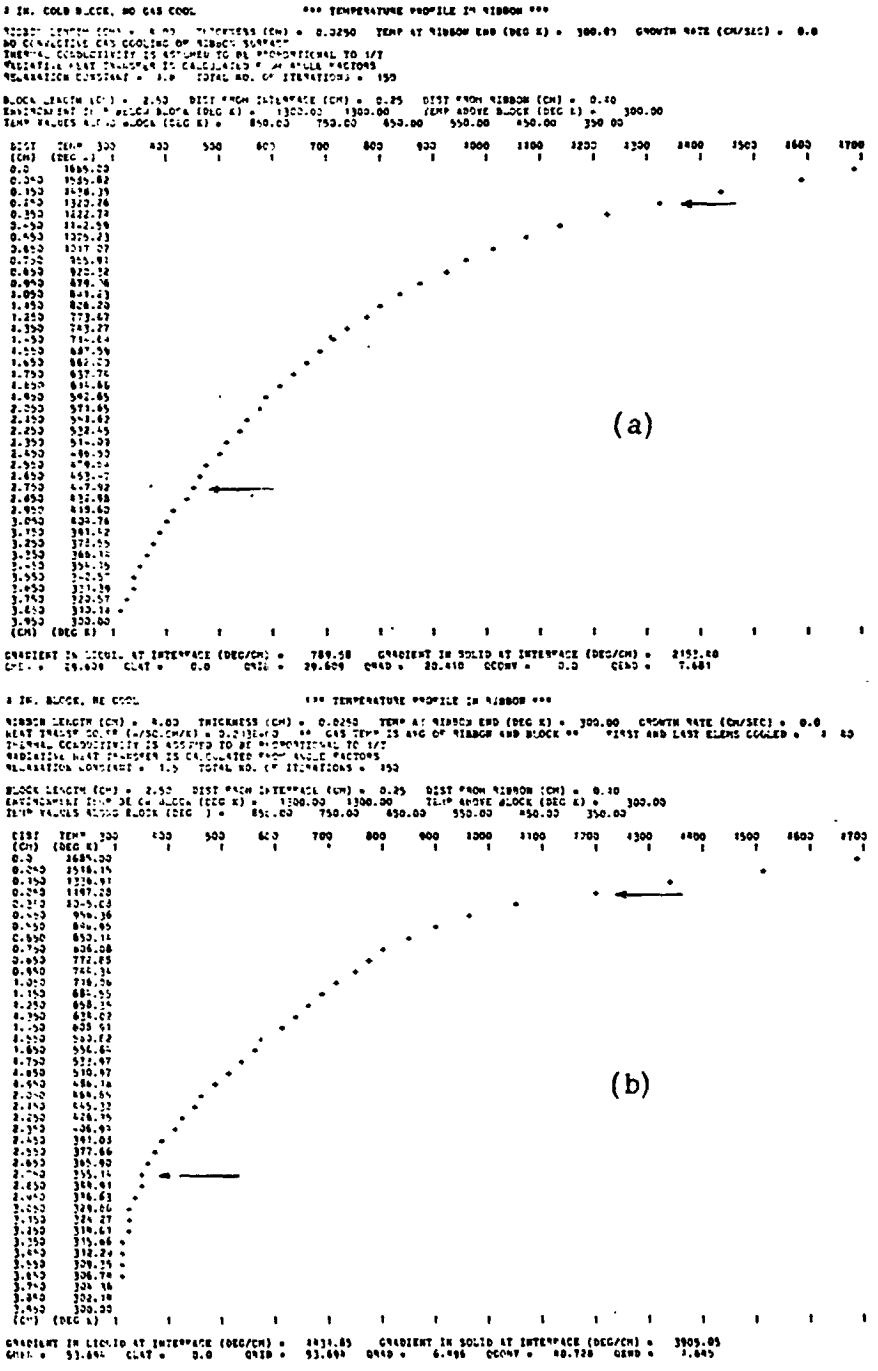

Fig. 13. Temperature profile in a 0.025 cm thick ribbon at zero growth rate for the cold afterheater block in Fig. 11b: (a) No gas in system; (b) Helium gas cooling. The arrows denote position of the block relative to the profile.

e. Horizontal and transverse temperature profiles

The analysis thus far has neglected gradients in temperature along the ribbon width (i.e., the horizontal profile) and through the ribbon thickness (i.e., the transverse profile). Clearly, more heat is lost at the ribbon edges because of the greater surface to volume ratio. Also, since heat is lost at the ribbon surface by radiation and convection, there must be a gradient through the ribbon thickness. An analysis of the three-dimensional temperature distribution in the ribbon was made on an earlier NSF program.[6] The calculations showed that the transverse gradients and the horizontal gradients at the ribbon edges were much smaller than the gradients in the vertical temperature profile at a given point. For example, the typical maximum temperature variation across the ribbon thickness is ~2° to 5°; the thermal stress associated with this variation is much less than that which results from the non-linear vertical profile. In a later section, we will show how the horizontal temperature profile can be varied purposely along the entire width of the ribbon in order to control the thermal stresses.

f. Linear vertical profile

Finally, a brief discussion is given here on the prospects of obtaining a linear vertical profile in the ribbon which, according to the qualitative analysis in Fig. 8 is expected to lead to a condition of no thermal stress. We consider the element of volume between T_i and $T_{i+1} < T_i$ in Fig. 9b. Even if the element were perfectly insulated (i.e., $Q_i^{CONV} = Q_i^{RAD} = 0$), the gradient at T_{i+1} would be less than at T_i because of the 1/T dependence of the thermal conductivity. If additional heat is lost by the element (by radiation or convection), d^2T/dx^2 will be even more positive. Therefore, in order to obtain a linear gradient, heat must actually be put into each element of volume (a small net heat input results from considering the specific heat transport in the ribbon). This, of course, would limit the rate of growth as the convective and radiative heat losses from the ribbon surface at the high temperatures help to carry away the latent heat which originates at the interface. It is important to bear in mind in designing the cooling/heating environment that a growth rate of 3 in./min for a 0.025 cm thick ribbon requires a vertical gradient of ~2400°K/cm in the ribbon at the growth interface. Clearly, a linear gradient of this magnitude cannot be maintained in practice over much of the ribbon length; basically, the quantity of heat associated with this gradient cannot be transferred from the ribbon at the lower temperatures.

4. Thermal stresses in the growth of ribbon crystals

This section summarizes the current status of the theoretical and experimental efforts relating to the thermal stress problem in EFG silicon ribbons. An excellent description of the theoretical formalism of thermoelastic problems is given in Chapter 8 of Ref. 10; therefore, after presenting some general remarks, we proceed to describe here the methods of solution and results only for the ribbon-shaped geometry of interest. First, we present an analytical solution for the thermal stresses in the ribbon, and discuss the limitations of this solution. We then describe a numerical method for calculating the stresses, and present the solutions for some simple temperature distributions. Procedures are described for determining the plane and magnitude of the maximum shear stress at every point in the ribbon, and for calculating the resolved shear stress in the slip planes and slip directions of the dislocations for a given growth orientation. Experimental approaches to the thermal stress problem and some experimental results are also described.

a. General remarks

The basic assumptions in the theoretical formulation of thermoelastic problems (see Chapter 8 of Ref. 10) are: that the temperature can be determined independently of the deformations of the body, that the deformations are small, and that the material behaves elastically at all times. Also, it is assumed that the body is isotropic, and that the Young's modulus and thermal expansion coefficient are independent of temperature (the latter assumptions are not necessary in the numerical calculation of the stresses). As described in an earlier section, thermal stresses arise as a result of non-uniform temperature distributions in the body (as well as stresses caused by external constraints). In the general three-dimensional problem, there are 15 unknowns: the three displacements (u, v, w), the six strain components (ϵ_{ij}), and the six stress components (σ_{ij}). These variables are related by 15 equations: three equilibrium equations (i = x, y, z)

$$\frac{\partial \sigma_{ix}}{\partial x} + \frac{\partial \sigma_{iy}}{\partial y} + \frac{\partial \sigma_{iz}}{\partial z} + F_i = 0 , \qquad (3)$$

where F_i is the i^{th} component of the body forces; six stress-strain relations

$$\epsilon_{xx} = \frac{1}{E}\left[\sigma_{xx} - \nu(\sigma_{yy} + \sigma_{zz})\right] + \alpha T, \text{ etc.} \tag{4}$$

and

$$\epsilon_{xy} = \left(\frac{1+\nu}{E}\right)\alpha_{xy}, \text{ etc.,} \tag{5}$$

where E is Young's modulus, ν is Poisson's ratio and α is the thermal expansion coefficient; and the six usual strain-displacement relations (e.g., p. 248 of Ref. 10). In addition, boundary conditions (surface tractions or displacements) are specified on the bounding surfaces. It should be noted from Eqs. (4) and (5) that the thermal expansion contributes only normal strains (i.e., no shearing strains).

A principal prediction of thermoelasticity theory is that if the temperature varies linearly with a set of rectangular Cartesian space coordinates, then all the stress components are identically zero throughout the body (provided that surface tractions, body forces and displacement discontinuities are absent). Conversely, this is the only temperature distribution for which all stress components are identically zero. This concurs with the qualitative argument we presented in Fig. 8.

The general, three-dimensional thermoelasticity problem cannot be solved analytically; various methods of solving for the strains, stresses or displacements are described in Ref. 10. However, the problem of calculating the stresses in the ribbon is considerably simplified by recognizing that the concept of plane stress is applicable in this case. Here we have the temperature T = T (x, y), and the thickness t in the z-direction small with respect to the other dimensions (see Fig. 14); therefore, it follows that

$$\sigma_{zz} = \sigma_{xz} = \sigma_{yz} = 0 . \tag{6}$$

The remaining stress components are obtained from the stress function ϕ (x, y) which is a solution of the following differential equation:

$$\nabla^4 \phi(x,y) = \frac{\partial^4 \phi}{\partial x^4} + 2\,\frac{\partial^4 \phi}{\partial x^2 \partial y^2} + \frac{\partial^4 \phi}{\partial y^4}$$

$$= -E\alpha\left(\frac{d^2T}{dx^2} + \frac{d^2T}{dy^2}\right) . \tag{7}$$

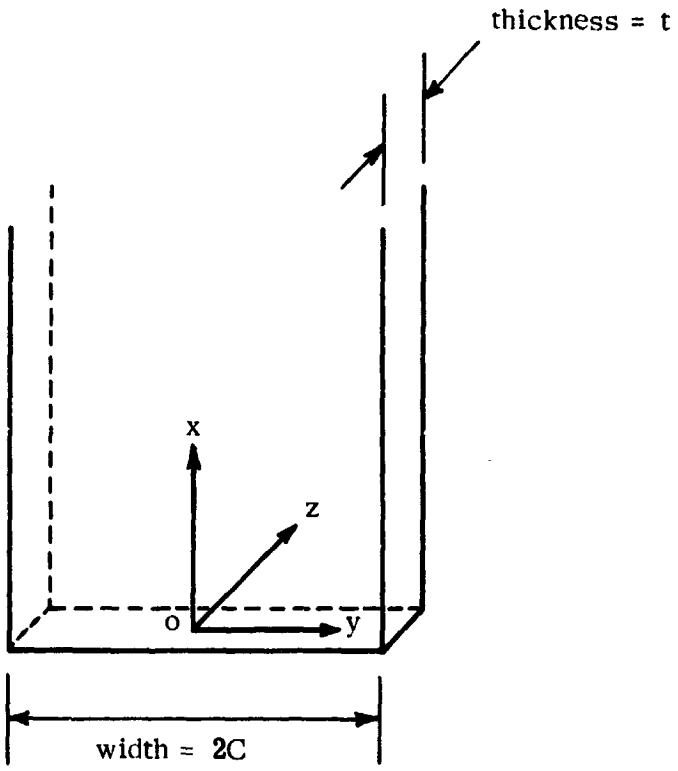

Fig. 14. Definition of coordinate system used in the calculation of the thermal stress in the ribbon. The plane stress solution is applicable for $t << C$ and $t << L$, where L is the ribbon length.

The boundary conditions for traction-free surfaces (which is the case of interest to us) are given by $\varphi = \frac{\partial \varphi}{\partial n} = 0$, where n denotes the normal direction to the bounding surface. The stresses are given by:

$$\sigma_{xx} = \frac{\partial^2 \varphi}{\partial y^2}, \quad \sigma_{yy} = \frac{\partial^2 \varphi}{\partial x^2}$$

and

$$\sigma_{xy} = - \frac{\partial^2 \varphi}{\partial x \partial y} . \tag{8}$$

In terms of the stress components, the boundary conditions are that $\sigma_{xx} = \sigma_{xy} = 0$ at $x = 0$, and that $\sigma_{yy} = \sigma_{xy} = 0$ at $y = \pm C$, where C is one-half of the ribbon width.

b. Analytic solution for the stress in the ribbon

Boley and Weiner[10] present a solution for the stress function φ for the case of a thin rectangular beam (see Fig. 14) of width 2C and length L with $C/L << 1$. The temperature in the beam is an arbitrary function of the coordinate y across the ribbon width, but it is a somewhat restricted function of x, as discussed in more detail below. The solution to Eq. (7) and traction-free surface boundary conditions is obtained as an infinite series $\varphi = \varphi_1 + \varphi_2 + \varphi_3 + \ldots$; successive terms of this series depend on successively higher derivatives of T with respect to x. For example, φ_i depends on $\partial^{2(i-1)} T / \partial x^{2(i-1)}$. Therefore, the series will converge rapidly if the temperature variation with x is sufficiently smooth, i.e., if it is expressible in a sufficiently rapidly convergent power series. The solutions for φ_i up to $i = 3$ are given in Ref. 10 for the general case where $T = T(x, y)$.

When the temperature is a function of the vertical coordinate x only, the first three terms in the solution are given by

$$\varphi_1 = 0, \quad \varphi_2 = - \frac{\alpha E}{24} (y^2 - C^2) \cdot \frac{d^2 T}{dx^2}$$

and

$$\varphi_3 = \frac{\alpha E}{360} (y^2 - C^2)^2 (y^2 - 3C^2) \cdot \frac{d^4 T}{dx^4} . \tag{9}$$

The leading terms for the stress components can be obtained from Eqs. (8) and (9):

$$(\sigma_{xy})_{th} = -\frac{\alpha E C^3}{6} \cdot \frac{y}{C} \cdot \left(1 - \frac{y^2}{C^2}\right) \cdot \frac{d^3T}{dx^3} \tag{10}$$

$$(\sigma_{xx})_{th} = \frac{\alpha E C^2}{6} \cdot \left(1 - \frac{3y^2}{C^2}\right) \cdot \frac{d^2T}{dx^2} \tag{11}$$

$$(\sigma_{yy})_{th} = -\frac{\alpha E C^4}{24} \cdot \left(1 - \frac{y^2}{C^2}\right)^2 \cdot \frac{d^4T}{dx^4} , \tag{12}$$

where the subscript "th" is used to denote the thermal component of the solution. From these equations, we see the qualitative dependence of the stress components on the ribbon width (w = 2C) and on the derivatives of temperature. In the qualitative discussion of the origin of thermal stresses in Fig. 8, we were essentially considering the σ_{xx} component of the stress.

(i) Corrections for non-zero tractions at interface

One of the problems with the above solution is that the requirement of zero traction at the end x = O (i.e., the solid-liquid interface) is not satisfied; rather the tractions are self-equilibrating there (i.e., no net forces or moments). According to Saint-Venant's principle (e.g., p. 345 in Ref. 10), the above solution is therefore valid only at distances $x > 2c$. However, most of the plastic deformation in the case of the ribbons occurs in the region $x < 2c$; hence we must add appropriate correction terms to the stresses in Eqs. (10) to (12) in order to account for the non-zero tractions at the interface.

The problem of the stresses arising from the application of self-equilibrating tractions on one end of a long, rectangular strip has been treated in a series of papers by Horvay.[11, 12] In order to obtain zero traction at the interface in the case of the ribbon, we must apply at x = O the normal stress (cf. Eq. (11))

$$\sigma^{\circ}_{xx}(y) = -\frac{\alpha E C^2}{6} \cdot \left.\frac{d^2T}{dx^2}\right|_{x=O} \cdot \left(1 - \frac{3y^2}{C^2}\right) \tag{13}$$

and the shear stress (cf. Eq. (10))

$$\tau^{\circ}_{xy}(y) = \frac{\alpha E C^3}{6} \cdot \left.\frac{d^3T}{dx^3}\right|_{x=O} \cdot \frac{y}{C} \cdot \left(1 - \frac{y^2}{C^2}\right) \cdot \tag{14}$$

The stresses which result from the application of the normal stress in Eq. (13) are given by[11, 12]

$$(\sigma_{xy})_{\sigma^\circ} = -\frac{\alpha E C^2}{6} \cdot \left.\frac{d^2T}{dx^2}\right|_{x=0} \cdot \left(\frac{\alpha_2^2 + \beta_2^2}{\beta_2}\right) \cdot \frac{y}{C} \cdot \left(1 - \frac{y^2}{C^2}\right) \cdot e^{-\alpha_2 x/C} \cdot \sin(\beta_2 x/C)$$

$$(\sigma_{xx})_{\sigma^\circ} = -\frac{\alpha E C^2}{6} \cdot \left.\frac{d^2T}{dx^2}\right|_{x=0} \cdot \left(1 - \frac{3y^2}{C^2}\right) \cdot e^{-\alpha_2 x/C} \cdot \left[\cos(\beta_2 x/C) + \frac{\alpha_2}{\beta_2} \sin(\beta_2 x/C)\right] \qquad (15)$$

$$(\sigma_{yy})_{\sigma^\circ} = -\frac{\alpha E C^2}{24} \cdot \left.\frac{d^2T}{dx^2}\right|_{x=0} \cdot \left(\alpha_2^2 + \beta_2^2\right) \cdot \left(1 - \frac{y^2}{C^2}\right)^2 \cdot e^{-\alpha_2 x/C} \cdot \left[\cos(\beta_2 x/C) - \frac{\alpha_2}{\beta_2} \sin(\beta_2 x/C)\right],$$

while the shear stress distribution in Eq. (14) leads to the stress components[11, 12]

$$(\sigma_{xy})_{\tau^\circ} = \frac{\alpha E C^3}{6} \cdot \left.\frac{d^3T}{dx^3}\right|_{x=0} \cdot \frac{y}{C} \cdot \left(1 - \frac{y^2}{C^2}\right) \cdot e^{-\alpha_2 x/C} \cdot \left[\cos(\beta_2 x/C) - \frac{\alpha_2}{\beta_2} \sin(\beta_2 x/C)\right]$$

$$(\sigma_{xx})_{\tau^\circ} = -\frac{\alpha E C^3}{6} \left.\frac{d^3T}{dx^3}\right|_{x=0} \cdot \frac{1}{\beta_2} \left(1 - \frac{3y^2}{C^2}\right) \cdot e^{-\alpha_2 x/C} \cdot \sin(\beta_2 x/C) \qquad (16)$$

$$(\sigma_{yy})_{\tau^\circ} = -\frac{\alpha E C^3}{12} \cdot \left.\frac{d^3T}{dx^3}\right|_{x=C} \cdot \alpha_2 \cdot \left(1 - \frac{y^2}{C^2}\right)^2 \cdot e^{-\alpha_2 x/C} \cdot \left[\cos(\beta_2 x/C) - \left(\frac{\alpha_2^2 - \beta_2^2}{2\alpha_2\beta_2}\right) \cdot \sin(\beta_2 x/C)\right],$$

where $\alpha_2 = 2.0751$ and $\beta_2 = 1.1429$. Similar correction terms for the higher order terms in the "thermal" solution in Eq. (9) have also been derived.[11, 12]

The total value of each thermal stress component is thus the sum of three terms, viz.,

$$(\sigma_{ij})_{\text{total}} = (\sigma_{ij})_{\text{th}} + (\sigma_{ij})_{\sigma^\circ} + (\sigma_{ij})_{\tau^\circ} \ . \tag{17}$$

Therefore, each stress component is a more complex function of the ribbon width and of the derivatives than given in Eqs. (10) to (12). The y-dependencies of the correction terms in Eqs. (15) and (16) are seen to be the same as those of the respective terms in Eqs. (10) to (12); the magnitude of the terms decrease exponentially along the vertical coordinate. An example is considered in the next section.

(ii) Thermal stress for radiation into 0°K environment

Consider the case of a ribbon which radiates into a 0°K environment. The temperature distribution is given by†

$$T(x) = \frac{1}{(a\,x + b)^{\frac{1}{2}}} \ , \tag{18}$$

where

$$a = \left[\frac{8\,(w+t)\,\sigma\,\epsilon}{3\,wt\,k_m\,T_m}\right]^{\frac{1}{2}} \qquad \text{and } b = 1/T_m^{\,2} \ .$$

We used the following values in the calculations: $w = 2$ cm, $t = 0.025$ cm, $\sigma = 5.67 \times 10^{-5}$ erg/cm^2 (°K)^4 sec, $k_m = 0.22 \times 10^7$ erg/cm °K sec, $\epsilon = 0.54$ and $T_m = 1685$°K. The resulting temperature distribution is shown in Fig. 15; it is readily seen that plastic deformation in response to the thermal stresses can be expected only in the region $x \lesssim 1$ cm where the temperature is in excess of ~600°C.

Figures 16 to 18 show the three stress components calculated for the temperature profile in Fig. 15. In each case, the contributions of the various terms in Eq. (17) to the total value of the stress component are shown. In the top part of each figure, we show the x-dependence of the maximum of each stress component, i.e., $\sigma_{xx}\big|_{y/C\,=\,1}$, $\sigma_{yy}\big|_{y/C\,=\,0}$ and $\sigma_{xy}\big|_{y/C\,=\,0.6}$ (in the latter case, the maximum

† The various terms in these expressions are defined in a previous section. The ribbon is assumed to be stationary for this calculation.

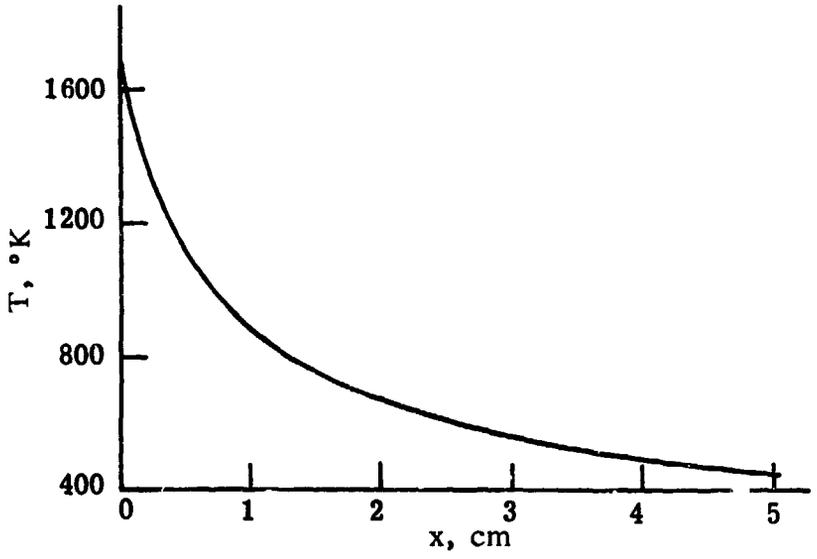

Fig. 15. Vertical temperature profile in ribbon for radiation into $0^{O}K$ environment.

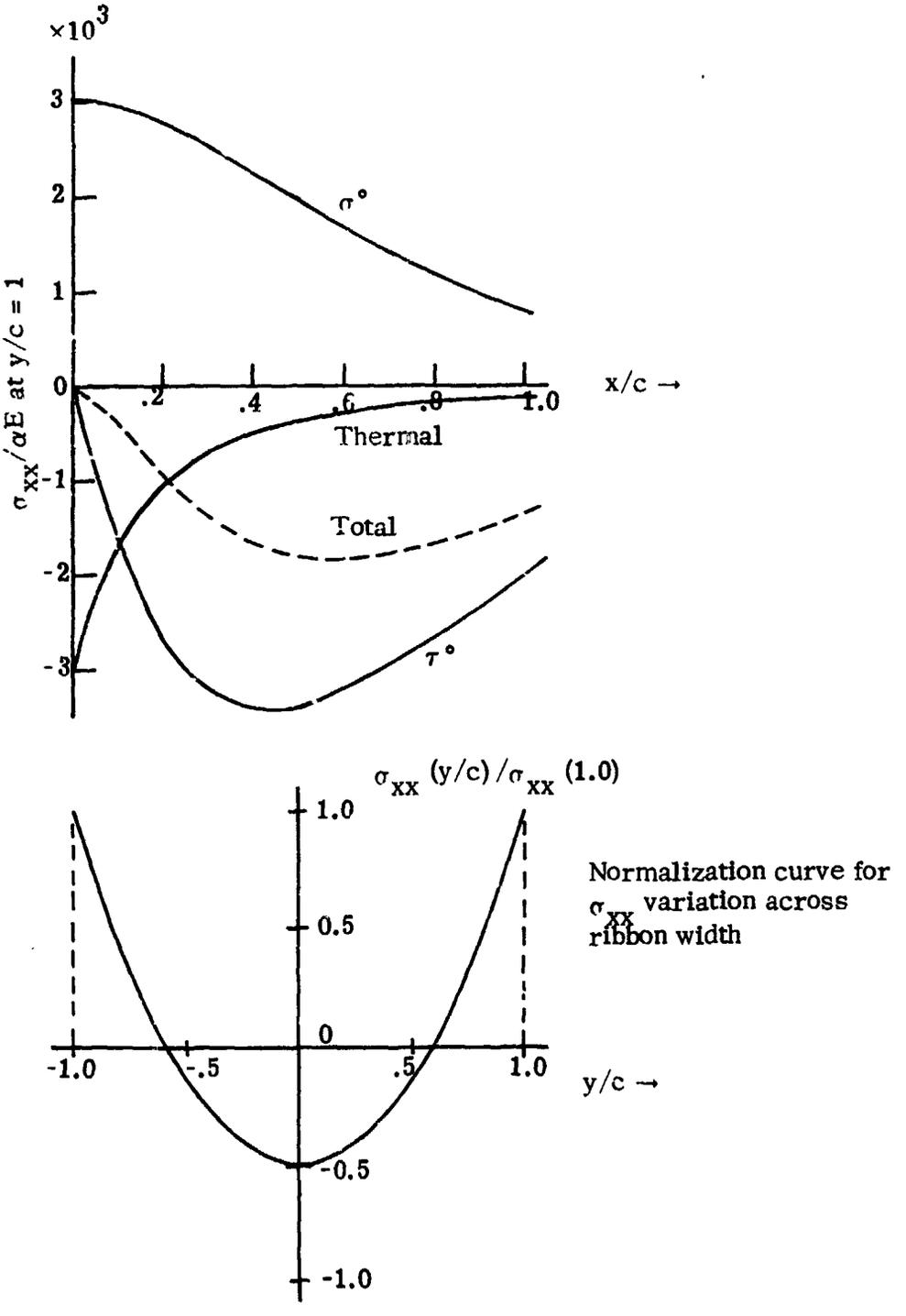

Fig. 16. Thermal stress component σ_{xx} in the ribbon for radiation into a 0°K environment.

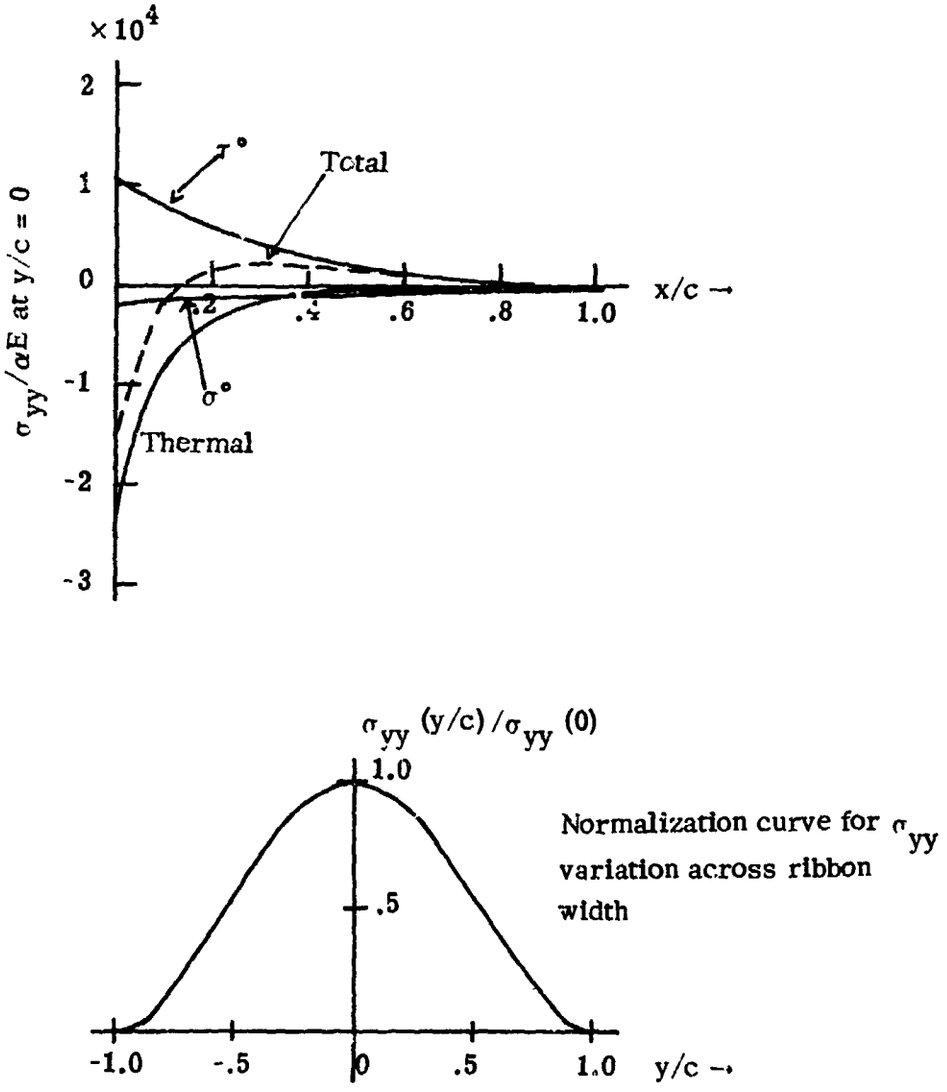

Fig. 17. Thermal stress component σ_{yy} in the ribbon for radiation into a $0^{\circ}K$ environment.

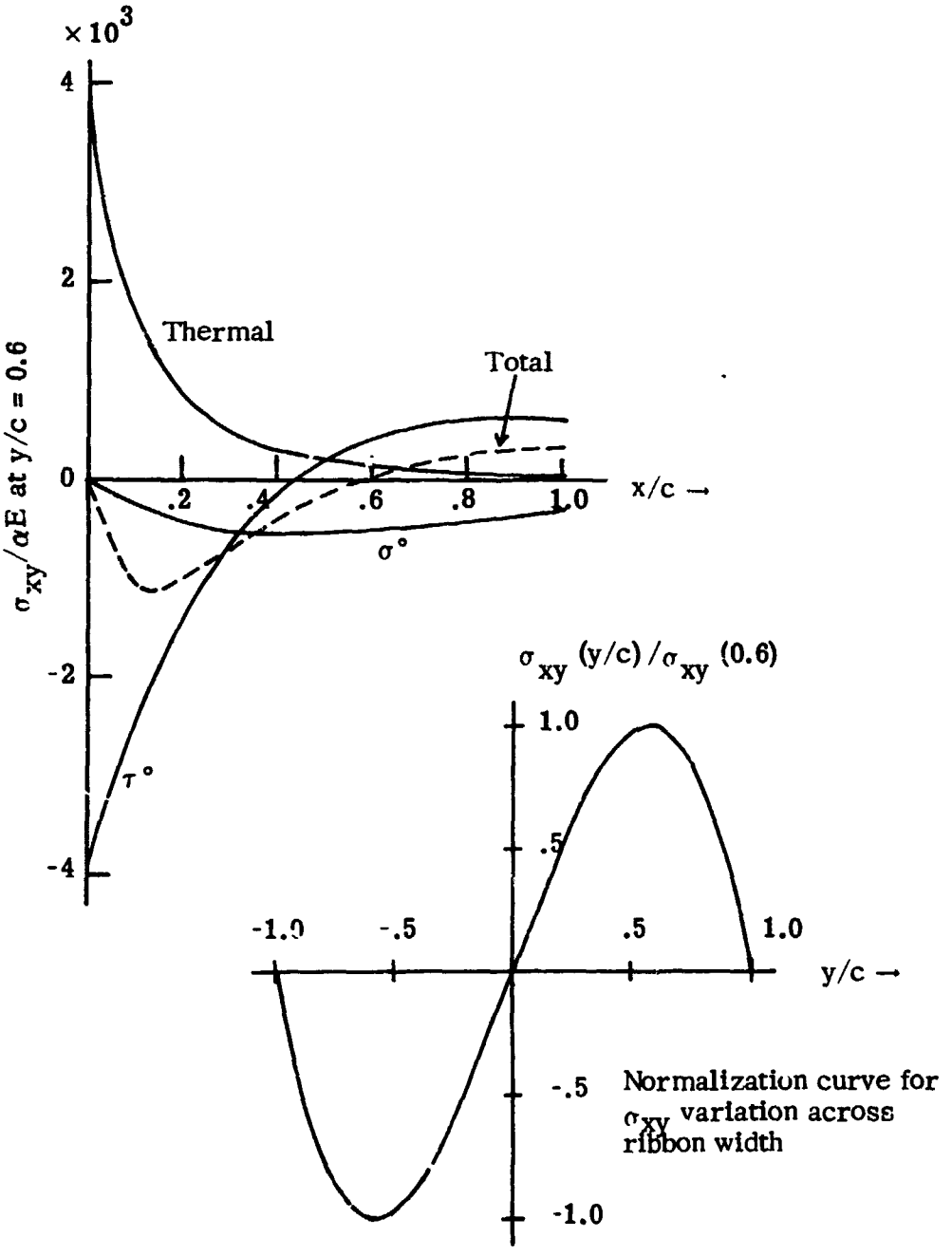

Fig. 18. Thermal stress component σ_{xy} in the ribbon for radiation into a 0°K environment.

actually occurs at $y/C = 1/\sqrt{3}$). The y-dependence of each stress component can be obtained by combining the top curves with the normalization curves in the lower parts of Figs. 16 to 18.

Considering the stress component σ_{xx} in Fig. 16, we see that the outer portion of the ribbon (i.e., $|y/C| > 0.6$) is in compression, whereas the inner portion is in tension. It is likely that the plastic deformation during growth, in response to these thermal stresses exceeding the yield stress, accounts for the "lengthening" of the ribbon in the central region, as observed from the residual stress in the ribbon (cf. Section II.B.2.).

(iii) Maximum and resolved shear stresses

Rather than discussing the above results in terms of the individual stress components, it is more useful to evaluate the maximum shear stress at each point in the ribbon and to determine the plane on which this stress acts.

As described in any standard text on elasticity, there exist two mutually perpendicular sets of axes on which the shear stress vanishes; the normal stresses on these planes are the "principal stresses" σ_1 and σ_2 which are given by

$$\sigma_{1,2} = \left(\frac{\sigma_{xx} + \sigma_{yy}}{2}\right) \pm \sqrt{\left(\frac{\sigma_{xx} - \sigma_{yy}}{2}\right)^2 + \sigma_{xy}^2} \quad . \tag{19}$$

The principal axes are at angles φ_1 and φ_2 to the x-axis, where

$$\tan \varphi_{1,2} = \frac{\sigma_{xy}}{\sigma_{xx} - \sigma_{1,2}} \quad . \tag{20}$$

The shear stress is maximum on a plane midway between φ_1 and φ_2, and also on a plane perpendicular to this plane. The maximum shear stress is given by

$$\tau_{max} = \frac{\sigma_1 - \sigma_2}{2} = \sqrt{\left(\frac{\sigma_{xx} - \sigma_{yy}}{2}\right)^2 + \sigma_{xy}^2} \quad . \tag{21}$$

Table II lists the values of τ_{max} (in kg/mm^2) as a function of position in the ribbon for the previous example of radiation into a 0°K environment; the plane on which this maximum shear stress acts varies from point to point in the table.†

† Values of $E = 1.94 \times 10^4$ kg/mm^2 and $\alpha = 5 \times 10^{-6}$ $°K^{-1}$ have been used in the calculations.

Table II. Maximum Shear Stress (in kg/mm^2) as a Function of Position in the Ribbon, and Temperature and Yield Stress as a Function of Vertical Distance.

x (cm)	y (cm) 0	0.3	0.6	1.0	T (°K)	σ_y* (kg/mm^2)
0	747	618	306	0	1685	0.03
0.2	52	83	103	45	1359	0.40
0.4	49	53	56	81	1170	1.70
0.6	6.1	9.8	25	89	1043	4.45
0.8	20	22	27	81	950	9.2
1	31	31	31	66	878	16.4
2	11.1	10.9	9.6	10.0	668	83
3	1.03	0.95	0.72	0.54	560	190
4	0.08	0.06	0.02	0.17	492	330
5	0.08	0.06	0.02	0.17	444	470

*Yield stress values were estimated from J. R. Patel and A. R. Chaudhuri, J. Appl. Phys. 34, 2788 (1963). Low temperature extrapolations probably exceed fracture stress.

The y = 0 values correspond to the central axis along the ribbon, y = 1 cm is the ribbon edge (a width of 2 cm was assumed). The table also lists the values of the temperature and of the yield stress of silicon at each temperature. It is seen that the thermal shear stress (if the material were to behave purely elastically) exceeds the yield stress in most of the region $x \lesssim 1$ cm, and hence plastic deformation will occur. The prediction of the residual stress in the grown ribbon is beyond the scope of the present analysis. Clearly, time dependent plasticity effects must also enter the problem; each portion of the ribbon at x = 0 must also experience the thermal stress at $x > 0$ as the ribbon cools down to room temperature.

Since dislocation glide is likely to be the predominant mechanism of plastic deformation, one should also calculate the resolved shear stresses on the slip planes and along the slip directions of the dislocations for a given crystal growth direction. Table III lists the resolved shear stresses for a ribbon growth orientation of (111) $[11\bar{2}]$. For randomly polycrystalline ribbons, such an analysis, of course, would not be very useful; recent evidence[19,20] suggests, however, that the ribbons attain a {110} <112> growth orientation and a steady-state defect structure.

Table III. Resolved Shear Stresses for (111) [11$\bar{2}$] Ribbon Growth

Plane	Direction	Resolved Shear Stress
(11$\bar{1}$)	<$\bar{1}$10>	$\frac{4}{\sqrt{17}}\ \sigma_{xy}$
(11$\bar{1}$)	<011>	$-\frac{4}{\sqrt{102}}\ (\sigma_{xx} - \sigma_{xy})$
(11$\bar{1}$)	<101>	$-\frac{4}{\sqrt{102}}\ (\sigma_{xx} + \sigma_{xy})$
($\bar{1}$1$\bar{1}$)	<011>	$-\frac{2}{3\sqrt{6}}\ (\sigma_{xx} - \sigma_{yy})$
($\bar{1}$1$\bar{1}$)	<10$\bar{1}$>	$\frac{2}{\sqrt{90}}\ (3\sigma_{xx} - \sigma_{yy} + 2\sigma_{xy})$
($\bar{1}$1$\bar{1}$)	<110>	$\frac{2}{3\sqrt{2}}\ (\sigma_{xx} + \sigma_{xy})$
(1$\bar{1}\bar{1}$)	<101>	$-\frac{2}{3\sqrt{6}}\ (\sigma_{xx} - \sigma_{yy})$
(1$\bar{1}\bar{1}$)	<0$\bar{1}$1>	$-\frac{2}{\sqrt{90}}\ (3\sigma_{xx} - \sigma_{yy} - 2\sigma_{xy})$
(1$\bar{1}\bar{1}$)	<110>	$\frac{2}{3\sqrt{2}}\ (\sigma_{xx} - \sigma_{xy})$

(iv) Limitations of the analytic solution

The major problem with the analytic solutions described in this section is that convergence of the solution occurs only if T(x) can be expressed as a polynominal in x. In the derivation of Eqs. (10) to (12), which we used in subsequent analyses and examples, we have already neglected the higher order terms (i.e., $i \geq 3$) in the solution. Thus we have neglected a d^4T/dx^4 term in σ_{xx} which would obtain from φ_3 in Eq. (9), whereas we included the same derivative in the calculation of σ_{yy} (from φ_2 in Eq. (9)). It turns out that the temperature distribution (Eq. (18)) for radiation into 0°K environment actually leads to increasingly higher values of the derivatives; for example, the thermal contribution to σ_{xx} from the i = 3 term is nearly an order of magnitude larger than the i = 2 term which we considered. Accordingly, the analytic approach outlined above

is only useful for temperature distributions which can be expressed in cubic (or less) power series in x. Otherwise, the solution gets even more complicated, as correction terms must be added for the higher order terms in σ_{xx} and σ_{xy} in order to have zero resultant tractions at the interface.

A further problem with the analytic solution is that it is not readily compatible with the numerical calculation of the temperature profile in the ribbon described in a previous section. For these reasons, we have developed a numerical program for calculating the thermal stress in the ribbon; this will be described in detail in a later section.

(v) Effect of horizontal temperature distribution

The analytic solution[10] extends to the case where the temperature is a function of the coordinate y along the ribbon width. Some preliminary calculations were therefore made to see the effect of curved isotherms on the thermal stresses. The following form was assumed for the temperature distribution in the ribbon:

$$T(x,y) = (1 - \beta y^2) \cdot T(x). \qquad (22)$$

Thus $\beta > 0$ corresponds to concave ("frowning") and $\beta < 0$ to convex ("smiling") isotherms. The calculations showed that $\beta > 0$ leads to lower stresses, while $\beta < 0$ leads to higher stresses than the $\beta = 0$ case. An approximate calculation also showed that the isotherm radius of curvature (with $\beta > 0$) must be of the order of the ribbon width in order to cancel the thermal stresses caused by the x-dependence of the temperature. A simple qualitative argument (as in Fig. 8) readily shows that the frowning isotherms should indeed lead to a reduction in the stress component σ_{xx} caused by the vertical temperature profile.

In view of these results, it is interesting to speculate on how the growth of zero dislocation density crystals is achieved in the Czochralski technique. There the growth interface is reported to attain a concave shape under the right growth conditions. It is conceivable that the combination of the radial temperature variation (i.e., frowning isotherms) and the smoother axial profile in the crystals leads to a condition where the thermal stresses during growth are negligible. There has been no general treatment of thermal stresses in Czochralski crystals caused by the combined effects of radial and axial temperature profiles.

c. Numerical calculation of the stress in the ribbon

It is apparent from the above that it will not be possible to obtain an analytic expression for the thermal stress in the ribbon which is of such a general form that it could deal with the temperature distributions of practical interest. We have therefore developed a computer program for determining the stresses by the method of finite differences.

At the point (i, j) in the ribbon (see Fig. 19), we can write Eq. (7) in the following finite difference form:

$$
\begin{aligned}
&20\left[\varphi\ (i,j)\right] - 8\left[\varphi\ (i,j+1) + \varphi\ (i+1,\ j) + \varphi\ (i,j-1) + \varphi\ (i-1,\ j)\right] \\
&+ 2\left[\varphi\ (i+1,\ j+1) + \varphi\ (i+1,j-1) + \varphi\ (i-1,\ j-1) + \varphi\ (i-1,\ j+1)\right] \\
&+ \varphi\ (i,\ j+2) + \varphi\ (i+2,\ j) + \varphi\ (i,\ j-2) + \varphi\ (i-2,\ j) \\
&= -\alpha E\delta^2\left[T\ (i,\ j+1) + T\ (i+1,\ j) + T\ (i,\ j-1)\right. \\
&\left. + T\ (i-1,\ j) - 4\ T\ (i,\ j)\right] . \qquad (23)
\end{aligned}
$$

Here we assumed that the nodal points are spaced equally in the x and y directions, i.e., that $\delta x = \delta y = \delta$. For example, we consider a ribbon 2 cm wide × 5 cm long, and set the increments $\delta = 0.1$ cm. Because of symmetry about the x-axis, we need to consider only half of the ribbon (see dark solid lines in Fig. 19). Since we would like to use the general form of the nodal equation (Eq. 23)) for all nodal points, we need to "extend" our grid beyond the ribbon (solid lines) in Fig. 19. Let's consider this extension by examining the boundary conditions.

Along the y-axis (i = 2), we have $\sigma_{xx} = 0$ and $\sigma_{xy} = 0$. Therefore, $\partial^2\varphi/\partial y^2 = 0$, $\partial\varphi/\partial y = A$ and $\varphi = Ay + B$. Also, $\partial^2\varphi/\partial x\partial y = 0$ and $\partial\varphi/\partial x = C$. The constants A, B and C can now be chosen arbitrarily, as this will not affect the magnitudes of the stresses. Therefore, we set $A = B = C = 0$, which leads to $\varphi\ (2,\ j) = 0$ and $\varphi\ (1,\ j) = \varphi\ (3,\ j)$ for all j. Similarly, we have $\varphi\ (i,\ 13) = 0$ and $\varphi\ (i,\ 14) = \varphi\ (i,\ 12)$ for all i. We also know that φ must be symmetric about the x-axis; therefore, $\varphi\ (i,\ 1) = \varphi\ (i,\ 5)$ and $\varphi\ (i,\ 2) = \varphi\ (i,\ 4)$.

At the far end of the ribbon (x = 5 cm), we suspect that φ must be some smooth function of x. We therefore impose the boundary condition that σ_{yy} = constant, i.e., $\partial^2\varphi/\partial x^2 = A$. Therefore, $\partial\varphi/\partial x = A\,x + B$ and $\varphi = Ax^2 + Bx + C$. We solve for the constants A, B and C by fitting the above quadratic equation to the

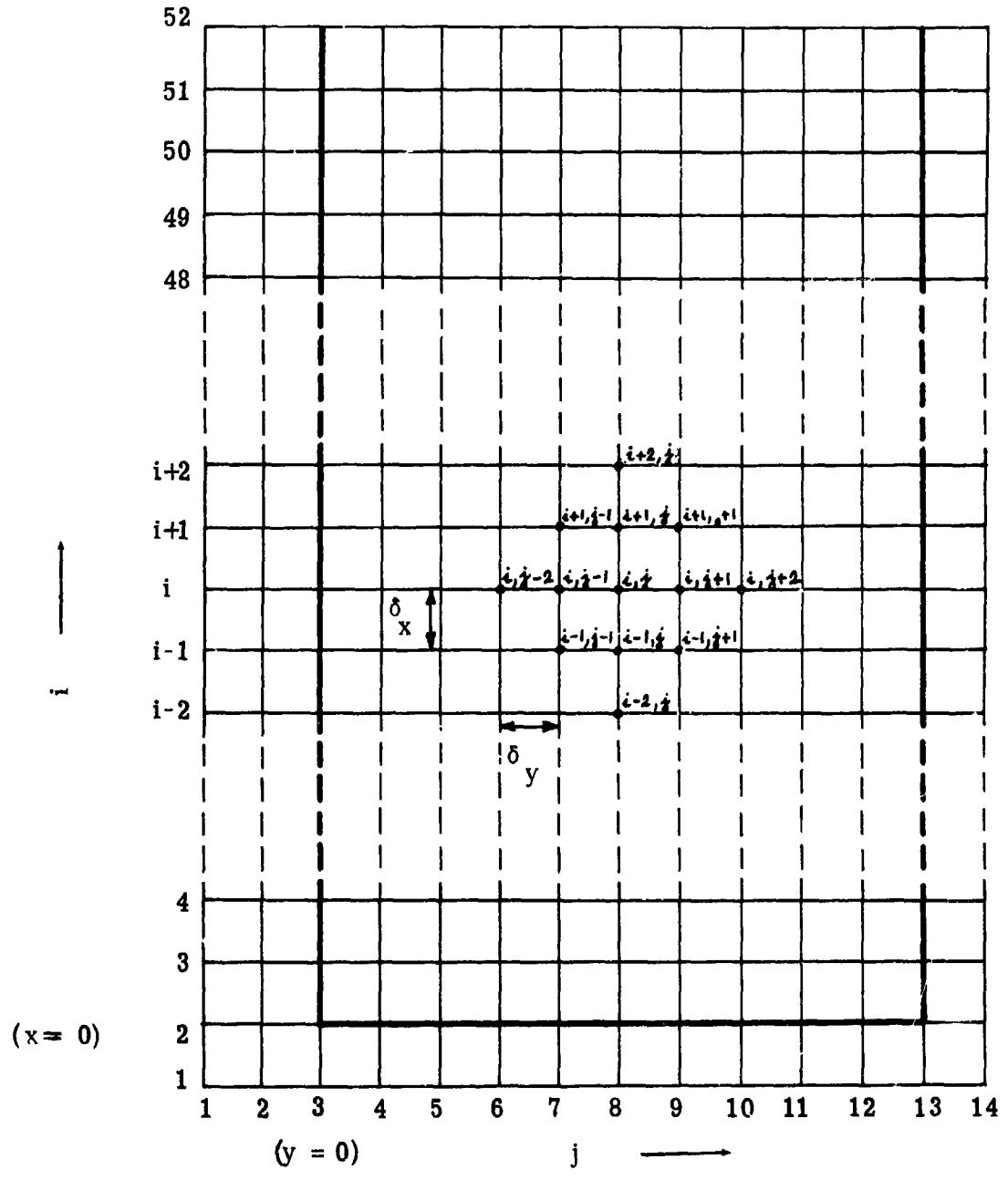

Fig. 19. Finite element grid for numerical calculation of the thermal stress in the ribbon. The dark lines denote one-half of the ribbon; j = 3 is the center axis, j = 13 is the ribbon edge, and i = 2 is the growth interface.

points i = 48, 49 and 50 (for each given j), then we extend the solution to φ (51, j) and φ (52, j). We can now write the nodal equation (23) for all i = 3 to 50 and j = 3 to 12.

(i) Method of solution

The solution of the nodal equations requires the specification of the temperatures T (i, j) and an initial guess solution of the stress function φ (i, j). We can then substitute a new value of φ (i, j) during each iteration, viz.,

$$\varphi_{new}(i, j) = \varphi_{old}(i, j) + R\left[\varphi_{func}(i, j) - \varphi_{old}(i, j)\right]. \qquad (24)$$

Here φ_{old} is the value of the stress function before the iteration, and φ_{func} is the value of φ (i, j) obtained from the nodal equation (23). R is the relaxation constant; R > 1 implies over-relaxation, and generally more rapid convergence. In our case, we found that R = 1.95 resulted in the fastest convergence; for R $\geq$ 2, the solution diverged. The operation indicated in Eq. (24) is carried out point by point (j = 3 to 12) and row by row (i = 3 to 50) during each iteration. It was found that the value of φ (i, j) remained constant to 5 significant figures after 5000 iterations. The stresses at (i, j) are then calculated from finite difference formulas equivalent to Eq. (8).

The form of the initial guess solution did not affect the results, except perhaps the speed of convergence during the first ~1000 iterations. Therefore φ (i, j) = O everywhere initially was used in most of the calculations.

(ii) Examples of numerical calculation of stress

The initial attempt to calculate stresses by the above numerical procedure was for the case of a ribbon radiating into a 0°K environment. As pointed out above, the analytic calculation gave only approximate results in this case because of neglecting the higher order terms in the solution. A comparison of the numerical and analytical solutions for this example shows that the qualitative nature of the analytical solution (i.e., the x-y spatial dependence and the relative magnitudes of the stress components at a given point) is correct, but that the stresses shown in Figs. 16 to 18 are too large by about an order of magnitude. This does not imply that the numerical solution is necessarily correct, however.

In order to examine the accuracy of the numerical calculation, we need to consider a temperature distribution for which the analytical procedure gives exact results. For simplicity, we assumed a quadratic form for T(x), i.e., $T(x) = A + Bx + C x^2$ (e.g., A = 1685, B = -560 and C = 56 were used). A comparison of the thermal stress components obtained by the numerical and analytical techniques showed that the former were consistently within $< 10\%$ of the correct analytical values. A slight problem with the numerical solution appears at the far end of the ribbon ($x \gtrsim 4$ cm); here the numerical solution begins to diverge from the analytic solution after many iterations. The problem undoubtedly lies in the far-end boundary condition used in the numerical calculations; this will require further investigation.

In conclusion, it is apparent from these results that, whereas the analytic solution was useful to show the qualitative dependence of the thermal stress on the spatial variables and the ribbon width, the numerical approach is far more useful for the practical cases of interest to us. For example, the numerical program can determine the stresses for any given T (x, y) in the ribbon, such as may be found in a given growth setup. The accuracy of the solution ($\sim 10\%$) is clearly sufficient for our purposes; some effort must still be made to improve the far-end boundary condition. The compatibility of the numerical stress calculation program to the thermal profile program described in Section II.B.3,is readily apparent; the ultimate usefulness of these programs would be, of course, to determine the T (x, y) (and the appropriate thermal environment which leads to it) such that, on the time-scale of EFG ribbon growth, no plastic strain occurs at any point in the ribbon. Although the thermoelasticity calculations described here are not sufficient to predict the residual stress in the ribbons, they do show the extent of plastic deformation which occurs and the temperature and ribbon regions where plastic flow is most severe. The inclusion of time-dependent plastic flow effects into the model would, in principle, allow one to calculate the residual stress in the ribbon. At the present time, there is not sufficient data on plastic flow in silicon to permit such a calculation.

d. Experimental approaches to thermal stress problems in EFG ribbons

The foregoing theoretical analyses of thermal profiles and stresses in ribbon-shaped crystals have greatly influenced the experimental program, particularly the design of the experimental equipment used to control the thermal environment of the ribbon. The detailed results of the experiments were presented in earlier reports on this program;[13, 14] a summary of the growth runs is given elsewhere in this report.

(i) Control of the vertical temperature profile

The vertical profile in the ribbon impacts both program objectives of fast and stress-free ribbon growth. For high crystal growth rates, we need to attain a high initial vertical gradient (i.e., at the growth interface) in the ribbon. This requires rapid cooling of the ribbon surface in this region, which will then lead to a large value of the second derivative of the vertical profile. The possible necessity for a trade-off between fast growth (large dT/dx and d^2T/dx^2) and low thermal stresses (small d^2T/dx^2) is therefore an immediate consideration.

The control of the vertical profile has been implemented by various passive and active afterheater block designs† (cf. Fig. 11). The extent of the hot (or cold) zone, the temperature profile along the block, and the location of the block with respect to the ribbon (i.e., distance from ribbon surface, and height above growth interface) have been the major variables in the experiments. Cooling of the blocks (by water flow) was also included in the designs. Typical growth rates which were achieved using "cold" afterheater blocks (e.g., Fig. 11b) were in excess of 2 in./min and, in some cases, approached the program goal of 3 in./min. These rates are not any higher, however, than what can be achieved by simply shielding hot surfaces and allowing the ribbon to radiate into an essentially 0°K environment. In addition, all the ribbons grown from the cooled blocks were excessively stressed. The use of insulating blocks[14] has resulted in lower growth rates (~1.2 in./min to 1.8 in./min) and still large residual stresses. Actively powered afterheater blocks have been designed and will be tested. To date, no afterheater block configuration has been used on this program which permitted growth rates in excess of ~1.2 in./min and resulted in tolerable residual stress in the ribbon. Later in this section, we will describe a recent design strategy which is expected to lead to fast, stress-free ribbon growth; the design makes extensive use of the theoretical modelling in Section II.B.3. to obtain successive manipulation of the vertical temperature profile in the ribbon.

(ii) Control of the horizontal temperature profile

The concept that concave (or frowning) isotherms in the ribbon should lead to a reduction in thermal stresses has been verified, to some extent,

†A "passive" block receives its heat from the environment (susceptor and crucible, die heaters, ribbon, etc.); an "active" block contains an independently powered heating element.

in some fast ribbon growth experiments on an earlier in-house program.[15] It was found that the tendency of the ribbon to buckle (cf. Fig. 7a) could be correlated to the shape of the solid-liquid interface. The latter was varied by changing the radius of curvature of the die top (in the plane of the die). At steady-state growth, the interface was either smiling (in the case of 12 in. radius of curvature dies) or frowning (in the case of flat-top dies); an example of each is shown in Fig. 20. The buckling of the ribbons after growth occurred with only the curved dies, i.e., with the smiling growth interface; the tendency to buckle can probably be associated with a larger residual stress in these ribbons. Of course, the shape of the interface is also that of the isotherms in the near vicinity, at least, of the interface. Hence the lower residual stress in the ribbons with the frowning isotherms provides support for the theoretically expected dependence of the thermal stress on the horizontal profile.

Attempts to vary the horizontal temperature profile (and to attain frowning isotherms) during the current experimental program have been two-fold; neither approach has been particularly successful thus far in reducing the residual stress. First, the use of reverse-curved (i.e., frowning) dies has been considered; initial experiments[14] with a 12 in. radius reverse-curved die encountered difficulties in attaining full-width (1 in.) growth, however. The residual stress measured in one 0.8 in. wide ribbon grown from this die was ~25,000 psi;[14] the small reverse curvature was clearly insufficient to affect the thermal stress in the ribbon (cf. Section II.B.4.b). A second approach has been to modify the cooling block to obtain preferential cooling near the edges of the ribbon. Although the horizontal isotherms were clearly affected, as evidenced by the fracture morphology of the seed or ribbon crystals, the residual stresses were still excessive. Clearly, further analytical work is required to identify the proper horizontal profile which would offset the effects of the vertical profile on the thermal stress in the ribbon.

(iii) Annealing of the residual stress

An obvious solution to the residual stress problem would be to subject the ribbons to a process of annealing at a high enough temperature such that stress relaxation, by the diffusion-controlled climb of dislocations, for example, can occur. Previous experience[16] with moderately stressed (i.e., < 20,000 psi) ribbons has indicated that the residual stress could be reduced to a negligible level by annealing the ribbons at 850°C for ~25 minutes. Similar experiments with the highly stressed ribbons grown on the current program has thus far proved to be unsuccessful; the ribbons would invariably shatter on being loaded into the annealing furnace. The

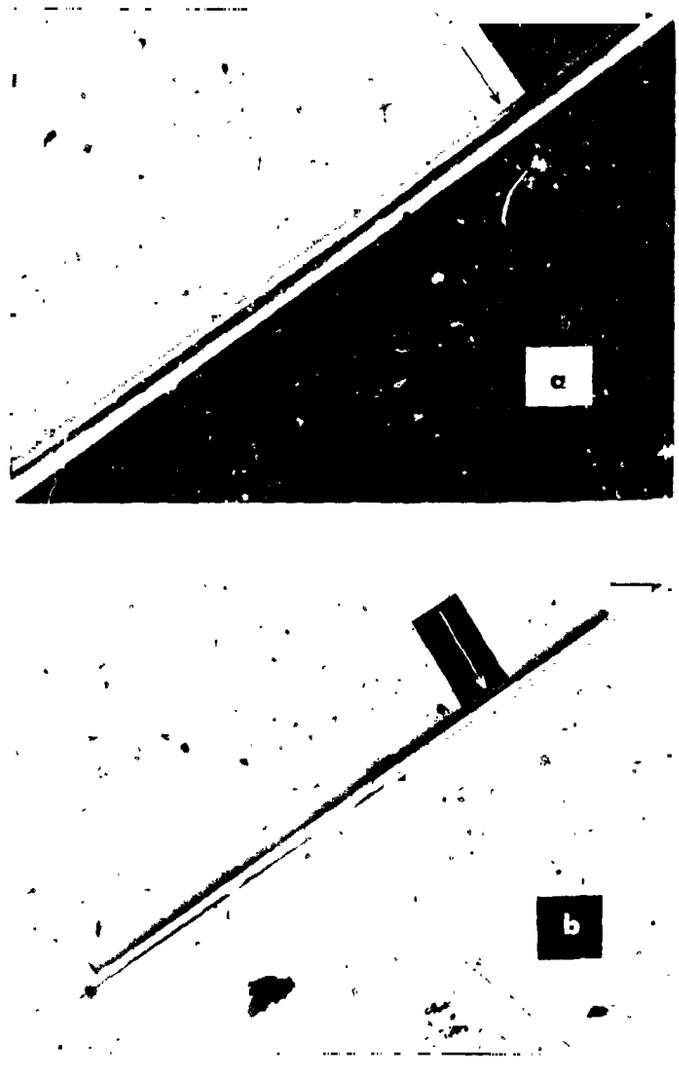

Fig. 20. Shapes of the solid-liquid interface (arrow) and die top in EFG ribbon growth. (a) Smiling interface with a 12 in. radius of curvature die; (b) frowning interface with a flat-top die.

fracture of these ribbons is probably caused by the additional mechanical and thermal stresses during the loading operation.

Assuming that the time-dependent relaxation process, in EFG ribbons containing dislocations, is likely to be the diffusion-controlled climb of dislocations, we can make an estimate of the annealing times, at various temperatures, which would be required to achieve complete stress relaxation. Using the experimental data at 850°C reported above, and possible activation energies[17, 18] of 2 eV, 4 eV or 5.1 eV for the relaxation process, we obtain the relaxation times given in Table IV. It is likely that the true activation energy falls somewhere between the limiting values we have assumed. It is readily seen from the table that stress relaxation occurs very rapidly at temperatures above ~1200°C and that it is very slow at temperatures below ~700°C. These findings have been instrumental in the development of a new strategy, described below, for reducing the residual stress in the ribbons during growth.

Table IV . Stress Relaxation Times as a Function of Temperature for Various Activation Energies

	Stress Relaxation Time (min)		
	Activation Energy		
T (°C)	2 eV	4 eV	5.1 eV
600	9400	3.5×10^6	9.2×10^7
700	609	1.5×10^4	8.6×10^4
800	66	172	293
850	25	25	25
900	10.3	4.3	2.6
1000	2.2	0.19	0.05
1100	0.58	0.013	0.002
1200	0.18	0.0013	0.0001
1300	0.067	0.0002	0.00001

(iv) A new strategy for minimizing residual stress in EFG ribbons†

The thermal stresses that arise as a result of non-linear temperature gradients in the ribbon during growth were discussed in detail earlier in this section. The theory described the forces that would tend to cause plastic deformation, and the dependence of the forces on the thermal profiles and on the ribbon geometry. If no plastic strain is permitted to occur during ribbon growth, then the above theory is immediately useful; it predicts that either the ribbon breaks in a region where the thermal stress is too high, or the ribbon emerges with no residual stress. On the other hand, if plastic deformation occurs, the calculation of the residual elastic strain in the grown ribbon requires a solution of the complete elastic-plastic problem; the latter involves the inclusion of the time-dependent plasticity effects into the theory.

At high temperatures, plastic deformation can occur by several distinct mechanisms; the important ones for this problem are the slip of dislocations and the climb of dislocations.

For slip to occur, dislocations must be present, and for more than a very small strain, dislocation sources must operate. For stresses above some level which is conveniently (but incorrectly) referred to as the "yield stress", deformation by dislocation slip is essentially instantaneous; that is to say, on the time scale of EFG ribbon growth, the strain rate is fast enough for the stress not to rise above the yield stress.

The process of dislocation climb allows plastic deformation to occur in response to any stress, however small. The rate of strain for a given stress, however, decreases very rapidly with decreasing temperature. For the present problem, this means that the stress in the ribbon does not remain at the yield stress, but is spontaneously relieved by the climb mechanism. This relief may be complete or partial depending on the time and temperature.

Thus we see that residual elastic strain in the ribbon can be avoided if there is either complete relaxation of stress or no relaxation of stress (i.e., no plastic strain) during the whole of the change of temperature of each element of the ribbon

† The collaboration in this work with B. Chalmers, A. R. Chaudhuri, M. C. Cretella, C. V. Hari Rao, D. N. Jewett, B. H. Mackintosh, A. I. Mlavsky and K. V. Ravi is gratefully acknowledged. The work described here was done on Mobil Tyco funded programs, and was not a part of this contract.

from the melting temperature to room temperature. We are therefore concerned with the minimum time required, at various temperatures, to allow complete relaxation, or the maximum time during which no relaxation occurs. From the relaxation times in Table IV, we see that stress relief in the ribbon would be effectively complete at any temperature above about 1200°C, and that almost no stress relief would occur below about 700°C.

The above considerations suggest that the vertical temperature profile in the ribbon, ideally, should consist of three zones. The first zone (from the melting temperature to ~1200°C) should consist of an initially large temperature gradient (~2400°C/cm for 3 in./min growth rate), and a very rapid decrease of the gradient away from the growth interface. This is required in order to achieve the desired high growth rate. Plastic strain in this zone should occur fast enough for the stress to be completely relieved. Of concern in this temperature region is the minimization of the plastic strain induced imperfections. This can be achieved by minimizing the second and higher order derivatives of the vertical profile, or by countering the effects of the vertical profile with an appropriate horizontal profile. The second zone should be a region of constant temperature gradient in which the stress-free ribbon cools from ~1200°C to below ~600°C; no stress or strain is introduced in the ribbon in this zone. The third zone should consist of a further decrease in gradient that is needed to reach zero gradient at room temperature. No plastic deformation can occur in this latter zone; therefore, if the ribbon is stress free when it enters it, it will again be stress free when it leaves this zone at room temperature. The crucial question in this third zone is the elastic (thermal) stress which is developed; if this stress does not fracture the ribbon, it will then disappear as the gradient becomes zero at room temperature.

The previously developed numerical thermal profile calculations played a major role in studying the feasibility of the above concept for the vertical profile in the ribbon, and in designing the hardware of the cooling/afterheating environments used to achieve the desired profile. An example of a cooling/afterheating block is shown in Fig. 21a. The distance above the growth interface is 0.102 cm (40 mils), while the distance from the ribbon is 0.076 cm (30 mils). The thermal profile along the block consists of a 0.127 cm (50 mil) cooling zone at 473°K, a same thickness insulating zone at 973°K, and an actively powered afterheating zone with a linear gradient of 35.4°K /cm starting at 1373°K. The calculated temperature profile in the first 1 cm of the ribbon is shown in Fig. 21b. The ribbon is assumed

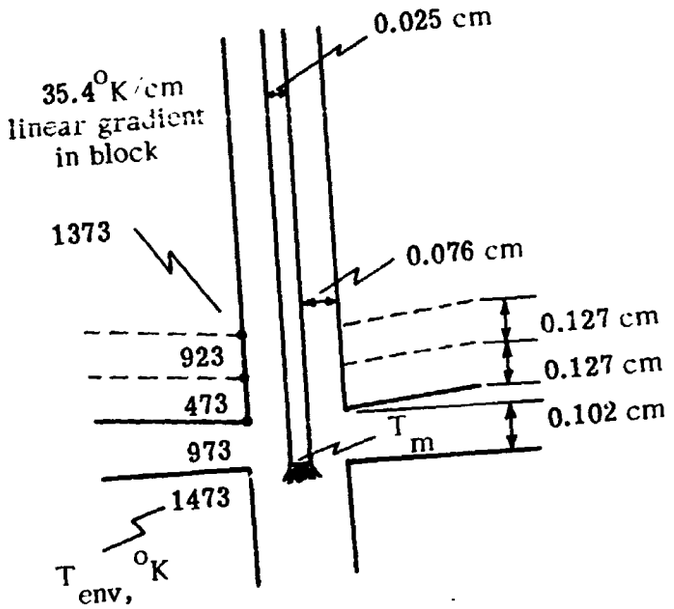

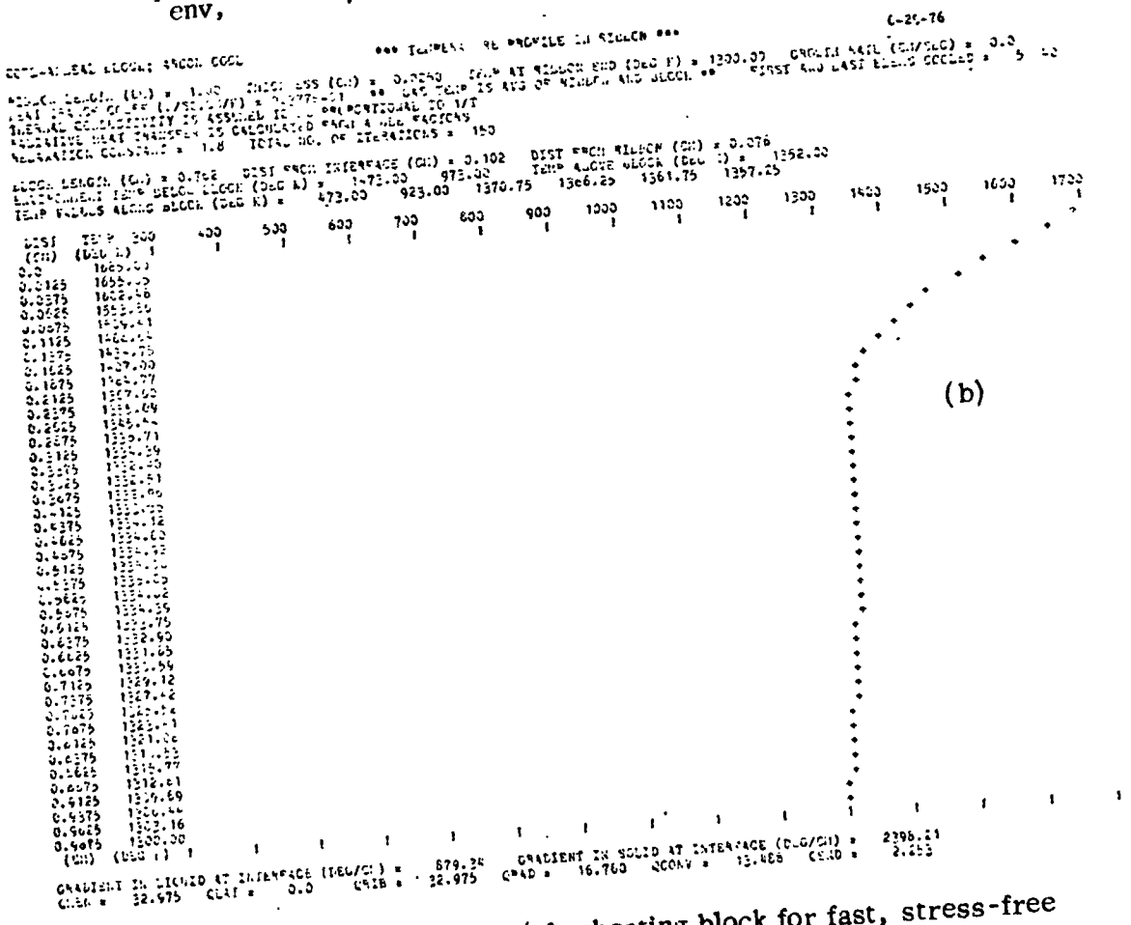

Fig. 21. (a) Schematic of cooling/afterheating block for fast, stress-free ribbon growth. (b) Calculated temperature profile in the first 1 cm of the ribbon for the block in (a).

to be stationary (V_g = 0); thermal interaction between the ribbon and the block is by radiation and conduction through argon. A maximum growth rate of 3 in./min (for a 0.025 cm thick ribbon) can be predicted from this profile. Within the linear gradient zone of the afterheater, the temperature profile in the ribbon soon attains that in the afterheater block.

The above concept for fast, stress-free ribbon growth has been tested and verified on a MTSEC in-house program.[19] Growth rates in excess of 2 in./min and ribbon widths up to 2 in. have been achieved; the residual stress in the ribbons was negligibly low. The cartridge design, with the built-in cooling/afterheating blocks, used in these experiments has been transferred to the current JPL program and will be used in the initial wide growth runs (on Machine No. 1).

(v) Summary

- Residual stress in EFG silicon ribbon crystals results from the plastic deformation the ribbons undergo at the high temperatures. The plastic flow is caused by the excessive thermal stresses in the crystal during growth.

- Thermal stresses result from non-linear temperature distributions in the ribbon. The principal contributor to the thermal stress is the vertical temperature profile; concave (or frowning) horizontal isotherms would tend to decrease the thermal stress. Transverse (or through thickness) gradients in the ribbon probably do not contribute to the thermal stress.

- Thermoelasticity theory, applied to the ribbon geometry, can predict the magnitude of thermal stresses and the extent of plastic deformation at each point in the ribbon. The theory cannot predict the residual elastic strain and stress in the ribbon; the latter involves the inclusion of time-dependent plasticity effects into the theory.

- Stress relaxation occurs rapidly in EFG silicon ribbon at temperatures in excess of 1200°C; almost no relaxation occurs below ~700°C.

- The effect of growth rate on residual stress is twofold: it affects the vertical profile via the specific heat transport in the ribbon, and it influences the extent of stress relaxation which can occur at a given temperature (cf. Table IV).

- The thermal stress in the ribbon during growth, and hence the residual stress, increases with increasing ribbon width; this is in agreement with experimental observations.

- The ribbon thickness affects primarily the vertical profile in the ribbon (dT/dx is proportional to $t^{-1/2}$).

- The possible effects of the thermal stress on the steady-state defect structure[20] and on the density of plastic strain induced imperfections, and the effects of solutes (carbon, impurities, etc.) on the stress have not been considered in detail.

- The theoretical numerical modelling program for the vertical profile in the ribbon has been used extensively to design a cooling/after-heating block for fast, stress-free ribbon growth. Initial experiments using this design have proved to be successful in that growth rates of >2 in./min and ribbon widths up to 2 in. have been achieved with only negligible residual stress in the ribbons.

C. Thin Ribbon Growth

One of the goals of the program is the growth of ribbons of controlled uniform thickness down to 0.1 mm. The impetus for establishing such a goal is based upon the dual requirements of low material usage (low cost) and sufficient thickness of the silicon for adequate solar cell conversion efficiencies. This goal was reviewed[14] in the light of the many known variables that influence ribbon growth, the reliability of crystal growth machine components, solar cell conversion efficiencies and the possible impact on yield and cost. The examination indicated that very thin ribbon growth is probably undesirable and the possible economic advantages of thin ribbons are significantly offset by other factors. The discussion of growth related factors is paraphrased below as an introduction to the experimental effort and as a rationale for its method. Thus, ribbon thickness t is given by a known analytical expression[6,7] of the form:

$$t = f(t_d, s, h_{eff}, \phi_o), \tag{25}$$

where t_d is the thickness of the die top, s is the meniscus height, h_{eff} is the effective height of the growth interface above the liquid level in the crucible and ϕ_o is

the angle between the tangent to the meniscus and the growth axis. Among these parameters, φ_o is a material parameter being related to factors such as the local orientation of the crystal surface. The other parameters, t_d, s and h_{eff} that control ribbon thickness are process or equipment related variables. Consequently, the sensitivity of ribbon thickness to these variables is of concern.

Shape stability in growth can be associated with the magnitude of dt/ds. Low $|dt/ds|$ will result in greater stability. The detailed analysis[14] of Eq. (25) shows that the ribbon thickness is more stable as s or h_{eff} decreases.

A more explicit dependence of the uncertainty in t due to uncertainties in the other geometric or process related variables results from the equation:

$$\Delta t = \left|\frac{\partial t}{\partial t_d}\right| \Delta t_d + \left|\frac{\partial t}{\partial s}\right| \Delta s + \left|\frac{\partial t}{\partial h_{eff}}\right| \Delta h_{eff} + \left|\frac{\partial t}{\partial \varphi_o}\right| \Delta \varphi_o \qquad (26)$$

Δt_d, the change in die top dimension can arise as a result of machining tolerances, which would be more critical as t_d decreases for thinner ribbon growth. In addition, small distortions of the die top due either to thermal effects or due to the formation of SiC particles on the die top would also adversely affect thickness control of thin ribbons. In general, $|\partial t/\partial t_d| \simeq 1$ independent of other variables. Consequently, any changes in t_d are immediately reflected as changes in t.

The change, Δs, in the meniscus height is associated with temperature fluctuations both on a short term and long term basis. In addition, s is also a function of h_{eff}. Present range of control is Δs is $\pm$ 0.05 mm with long time prospects of $\pm$ 0.025 mm.

h_{eff} changes continuously as the melt level in the crucible drops. With melt replenishment, it should be possible to keep Δh_{eff} to within 1.25 mm. φ_o changes by about $\pm 1°$ and is largely related to local crystal orientation effects.

The main contribution to Δt comes from the $|\partial t/\partial s|\,\Delta s$ term, with the next most important contribution coming from the $\partial t/\partial t_d$ term, which is $\cong \Delta t_d$. As s increases (for given t_d and h_{eff}) and thus causes a decrease in t, the error Δt not only increases due to the Δs term but also due to other terms. Increasing h_{eff} also increases the Δs contribution to Δt, offsetting the decrease that occurs due to the other variables. The experimental approaches to thin ribbon growth are thus clearly guided by theory; the controllable empirical parameters are t_d, s and h_{eff}.

t_d was the first variable experimentally approached. Early in the program, one-piece dies were tested to reduce splaying of top edges of the dies[21] and thereby to achieve better dimensional control. The experiments were successful and a variety of one-piece dies were used during the effort to better understand and achieve 'thin ribbon' growth. Open, closed, and plugged end one-piece dies were evaluated; the latter to effect a higher meniscus and improve edge stability.[14]

Characterization of the dies included examining the interaction of the dies with the melt, specifically the formation and distribution of SiC. Silicon carbide particles in ribbons are loci of structural imperfections and high impurity concentration,[28] and are detrimental to solar cell performance. Early in this program, a one-piece die was sectioned, polished, and examined by metallography. The die had been at melt temperature for about five hours and about 18 inches of ribbon was grown from it. A large number of SiC particles were found at the bottom outside of the die (Fig. 22a). Very uniform carbide layers and infiltration of graphite by silicon were found in the capillary channels with very few acicular growths. Carbide layer thickness was ~0.02 mm and penetration depth was ~0.22 mm (Fig. 22b). However, acicular carbides were grown in the feed slot across the top of the die.

Growth runs were made to evaluate dies with minimum t_d. These dies had a capillary slot width of only 0.013 cm and "knife-edges" for a total t_d of 0.013 cm. Vertical 0.09 cm capillary feed tubes are coupled to the slot by a 0.07 cm horizontal bore hole. The first die used filled only with great difficulty. Ribbon growth was very unstable - the resulting ribbon was ~14 mils thick. A post mortem showed a large effective die top thickness due to SiC growth all over the die (Fig. 23). The subsequent run also used a thin t_d die. Filling was facilitated by partially plugging the 0.07 cm hole below the die slot. The seeds used were etched to ~5 mils thickness. The first ribbon slowly increased in thickness from ~0 mils to 8 mils over 7 in. of growth.

The subsequent six starts all behaved the same way. Growth rates were all around 0.6 in./min. Faster rates were not achievable due to the freezing of silicon in the capillary.

The above experience, corroborating many previous observations, indicates that the effective t_d will not be a precisely controllable parameter, growth rates from a small t_d die will be low, and the thin ribbon goal must be achieved through control of h_{eff} and/or s.

(a)

3.2X

(b)

409X

Fig. 22. (a) SiC growth at the bottom of the die. Particles appear to have grown on the top of the residual melt and were loosely adhering to the graphite (die) wall.

(b) Carbide layer and infiltrated zone in one capillary wall.

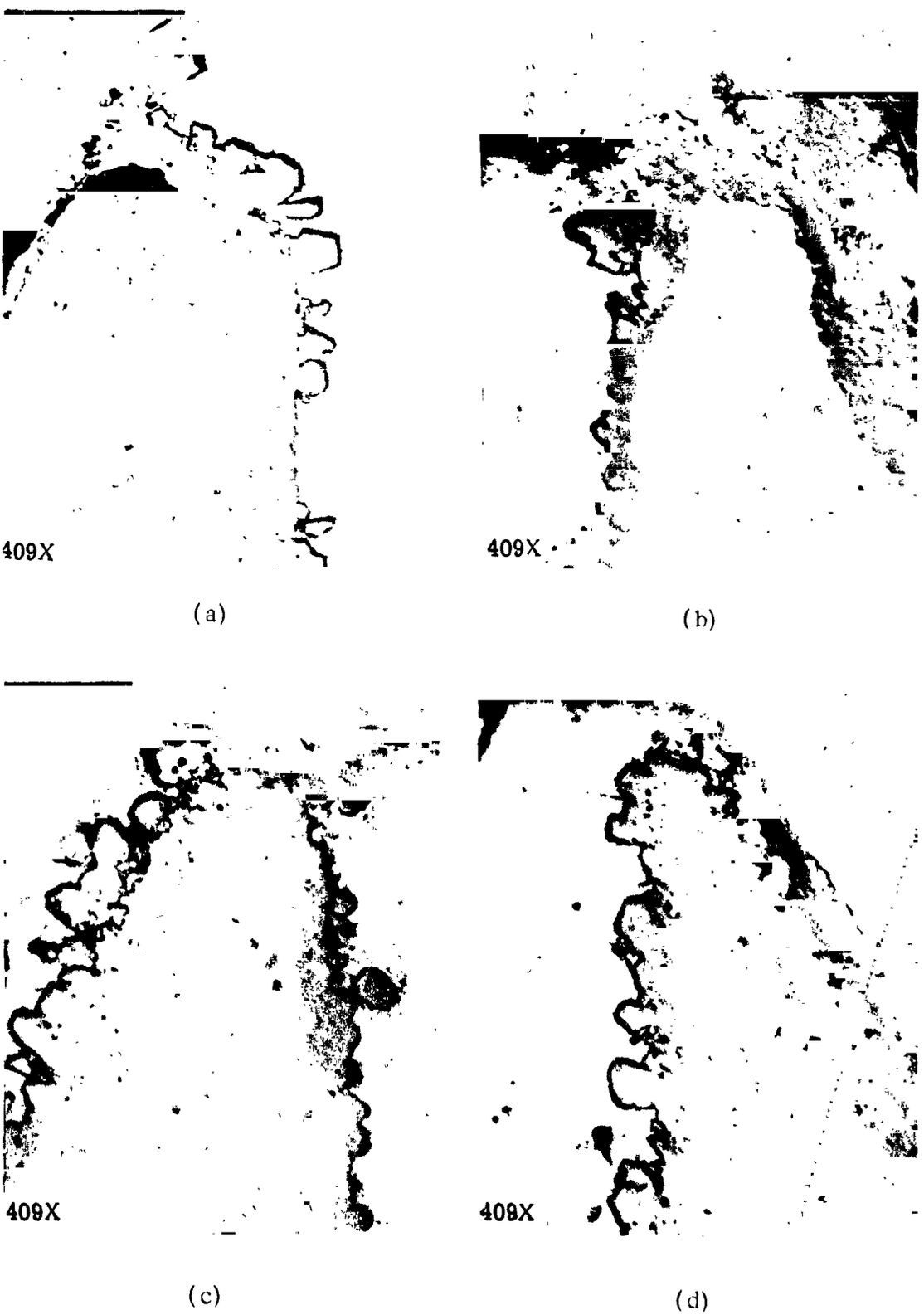

Fig. 23. Top edges, left and right, from the center (a and b) and the end (c and d) of a typical used die showing the effective increase in t_{cl} due to SiC crystal growth.

Two growth runs were made to evaluate the influence of h_{eff} on ribbon thickness. However, meniscus height variations masked any h_{eff} effects. Because fixing h_{eff} and varying the meniscus height is very straightforward, these experiments were next run.

Three growth runs were made to specifically relate meniscus height to ribbon thickness. t_d and h_{eff} were recorded. (The die top dimensions of nine dies were measured using an optical comparator. The mean total die top thickness (t_d) was 14.1 mils. The range was 3.2 mils and the standard deviation was 0.955 mils). Die top thickness at the end of each run but prior to cool down was measured from calibrated Polaroid photomicrographs (Fig. 24a). Dies of 3 radii were used to achieve three very different meniscus heights. The first run was made with a flat die; the second, with a 5" radius die; and the third, with an 8" radius die. Values for meniscus height, Table V, were also obtained from photomicrographs (Fig. 24b, c, d). Values are corrected for the 14^0 viewing angle (actual meniscus height $s = x \cdot \sec 14^0 - 1/2 \tan 14^0 (t_d - t)$, where t is ribbon thickness and x is the apparent meniscus height). h_{eff} was measured after the run was completed.

Values for ribbon thickness were taken with a ball micrometer measuring the center of the ribbon at the point indicated by the ribbon displacement indicator. The observed results are illustrated in Fig. 25 through 27. The experimental data demonstrates a variation of ribbon thickness with meniscus height, as expected from theory (solid lines). The quantitative disagreement between experiment and theory is probably caused by the difficulty in determining the edge-to-edge die dimension (t_d) during growth and by the uncertainty in measuring the meniscus height from the photographs. A 2 mil change in die thickness, for example, can shift the theoretical curves to coincide with the experimental values.

D. Characterization

Silicon ribbons typically contain both crystallographic defects and discrete inclusions. The inclusions are clusters of SiC particles. The crystallographic defects are predominantly twins, intersecting twin boundaries, dislocations and low and high angle grain boundaries. Experiments were carried out to determine if an optimum seed orientation exists which would give rise to single crystal ribbons, and to determine seed - ribbon orientation relationships. Experiments were also

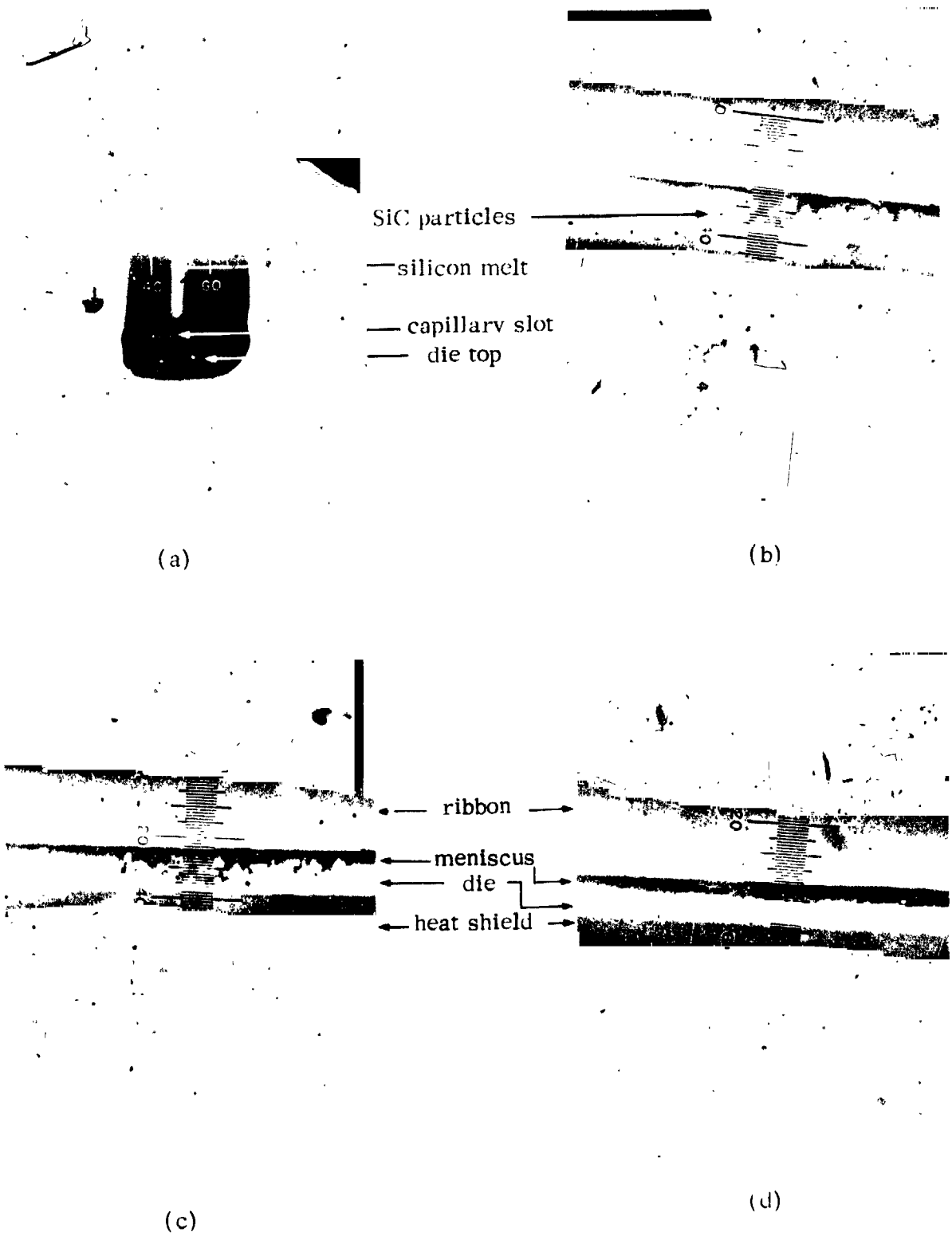

Fig. 24. Die top during ribbon growth: (a) end view; (b, c, d) side view showing die, meniscus, and growing ribbon.

Table V. Meniscus Height Versus Ribbon Thickness
(mils)

Ribbon No. 14-200*		Ribbon No. 14-201**		Ribbon No. 14-202***	
s	t	s	t	s	t
2.4	14.5	8.35	6.75	8.99	12.0
2.4	14.5	6.71	7.5	11.77	7.5
2.78	15.0	7.45	7.25	11.32	8.0
3.4	14.5	8.18	7.0	6.90	12.5
9.1	10.5	7.00	7.5	7.56	12.0
9.06	9.5-10.0	6.13	12	6.8	13.0
7.18	11.5	8.78	6.5	6.60	12.0
3.3	13.5	7.54	8	8.87	11.0
4.15	13.0	6.71	9	11.44	12.5
6.54	10.5	8.81	6	10.4	12.0
5.84	12.25	7.41	7	9.41	11.5
7.03	10.25	7.44	7.25		
		4.10	11		
		5.06	9.5		
		6.71	9.0		

*h_{eff} = 1.87"; die radius = ∞, t_d = 20 mils.
**h_{eff} = 1.57"; die radius = 5", t_d = 16.4 mils.
***h_{eff} = 1.77"; die radius = 8", t_d = 16.5 mils.

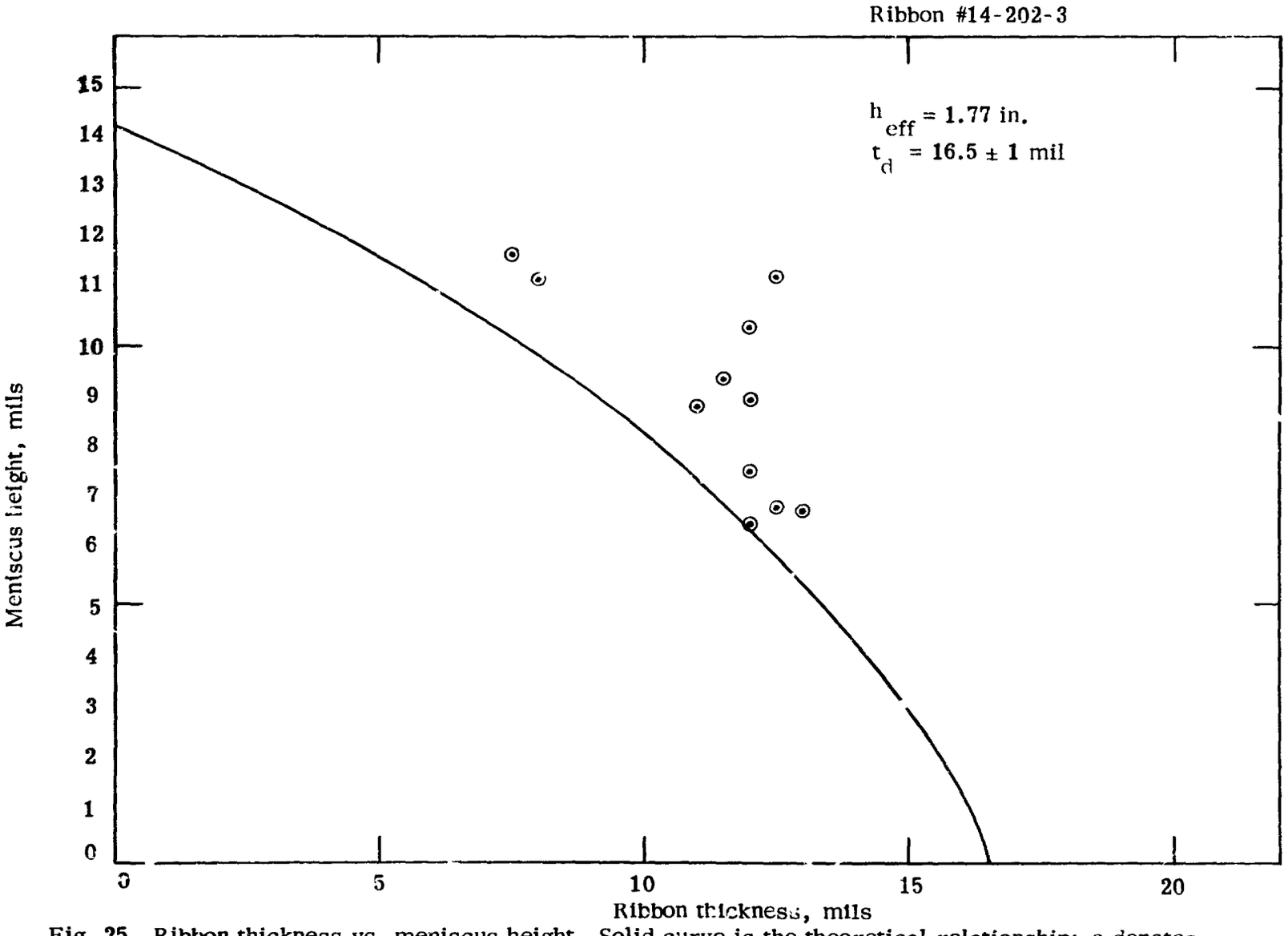

Fig. 25. Ribbon thickness vs. meniscus height. Solid curve is the theoretical relationship; ⊙ denotes experimental results.

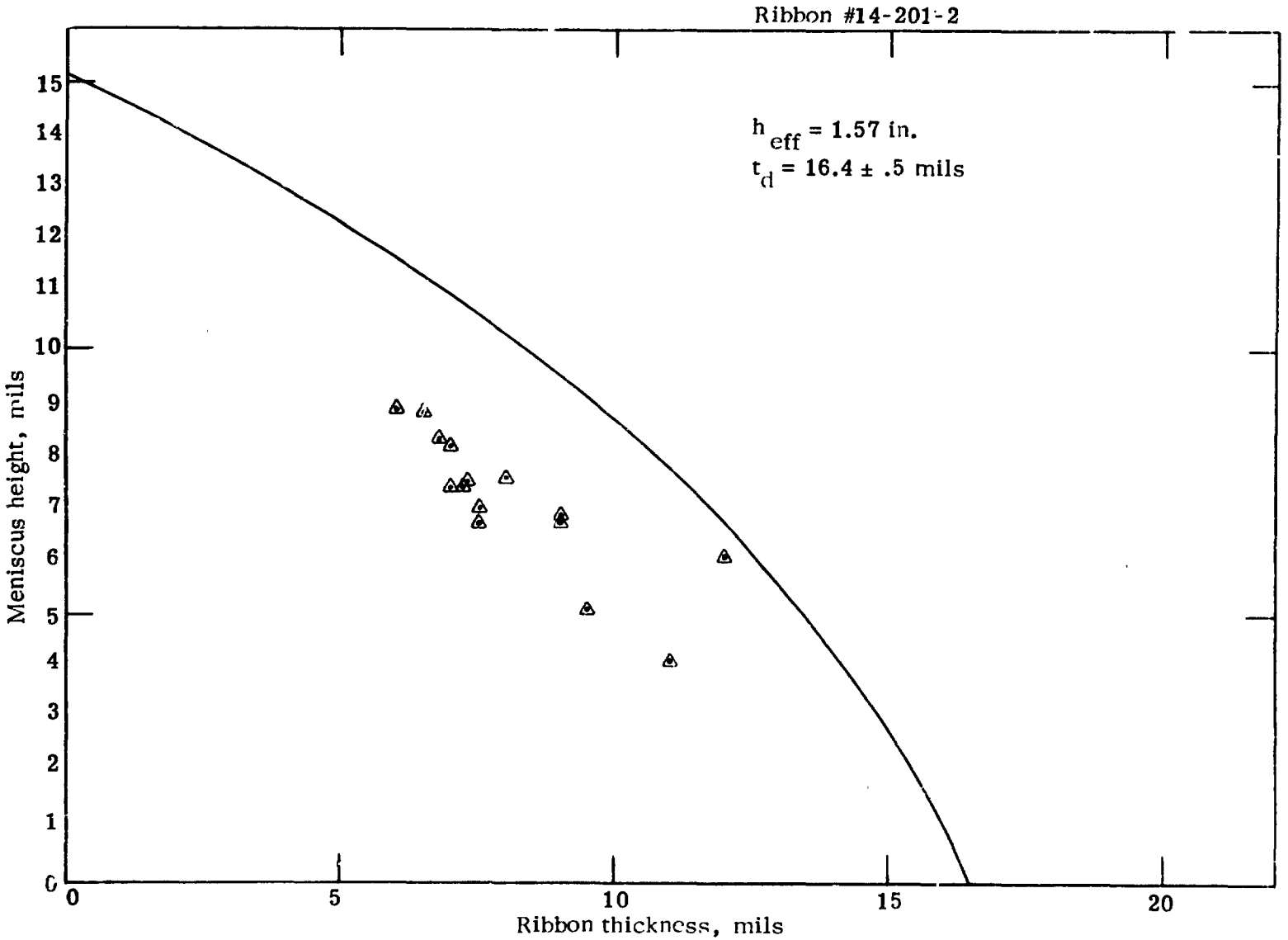

Fig. 26. Ribbon thickness vs. meniscus height. Solid curve is the theoretical relationship; ▲ denotes experimental results.

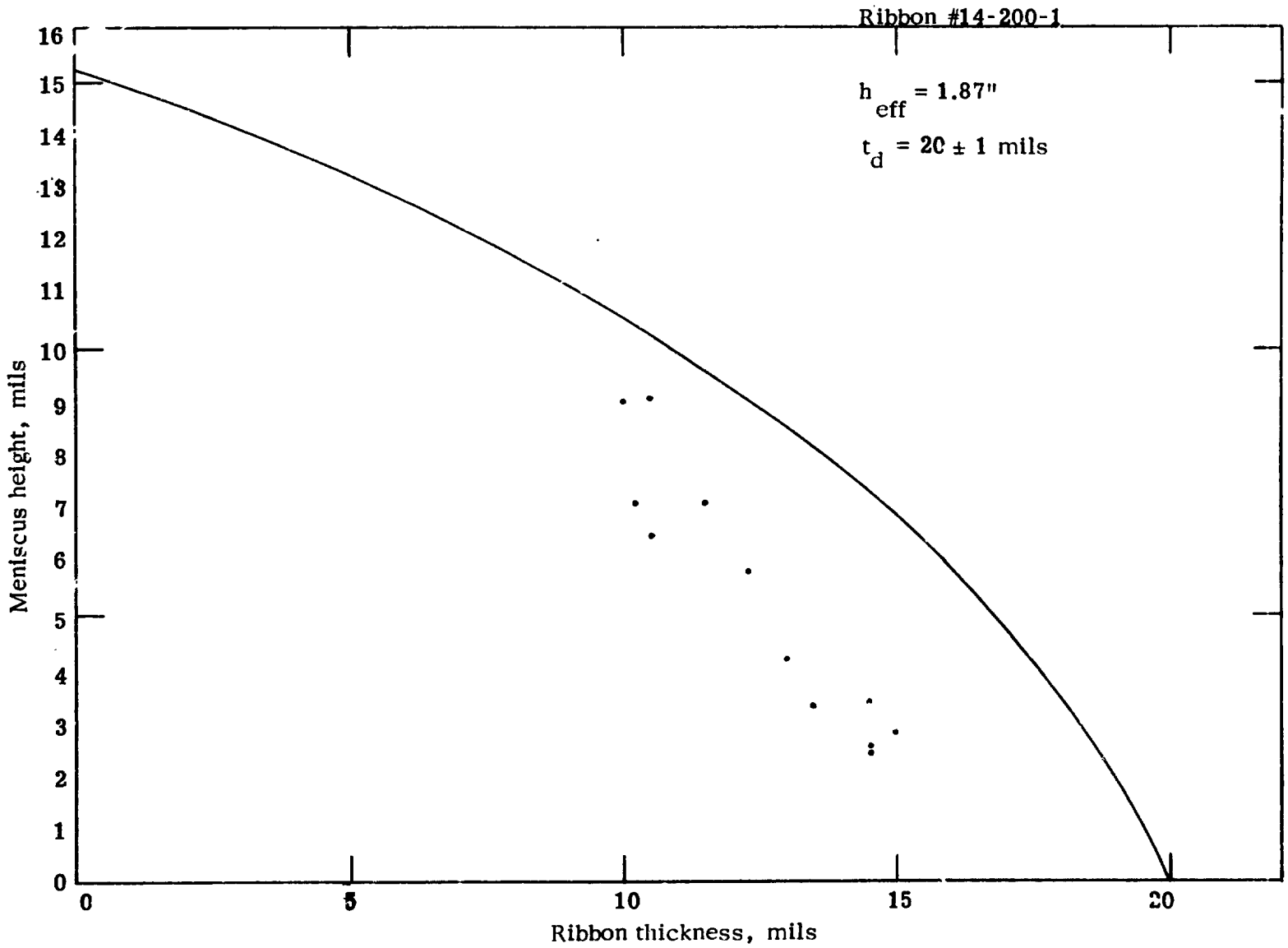

Fig. 27. Ribbon thickness vs. meniscus height. Solid curve is the theoretical relationship; • denotes exper mental results.

undertaken to examine the electrical activity of the various defects present in the as-grown ribbons. Spreading resistance measurements were done on selected samples to assess the influence of the defect species on impurity distribution.

1. Crystallinity and orientation studies

Although single crystals have been grown by the EFG technique the silicon ribbons grown deviate from single crystallinity. However, the ribbons are not composed of variously oriented grains separated by high angle grain boundaries. The sustained growth of long ribbons has been observed to result in an essentially uniform structure consisting of linear parallel boundaries largely parallel to the ribbon edges.

The linear defects are postulated to be predominantly twins with some of the twin boundaries being associated with dislocations. The relatively high densities of twin boundaries with the twin planes being normal to the ribbon surface should result in twin related regions between boundaries. However, X-ray data indicates that the ribbon surface has a predominance of a single orientation. Two possible mechanisms could account for this observation. If the twinned structure is composed of closely spaced twins or twin pairs with the crystal returning to its "untwinned" state immediately following the generation of a twin, the resulting structure would consist of a predominance of a single orientation with a small percentage of the crystal possessing the twinned orientation. The relatively macroscopic sampling procedure of the Laue back reflection technique or the channeling patterns obtained from an SEM might not detect the twinned orientations between closely spaced twins. Some preliminary transmission electron microscopy studies have shown the presence of very closely spaced twins, with twin spacings as low as 250 Å, in these ribbons.

An alternative suggestion is that the linear boundaries are composed of stacking faults which would not give rise to twin reflections in X-ray micrographs. In the limit, a stacking fault is equivalent to a twin pair with an extra plane of atoms (or two extra planes for the diamond cubic structure) between them (for the case of extrinsic faults). Figure 28 is a {110} projection of the diamond cubic structure showing the crystallography of the twin pairs or an extrinsic stacking fault. Either of the above discussed models can account for the observations. However, attempts to more precisely assign one or the other of the mechanisms to explaining the phenomenon requires further investigation.

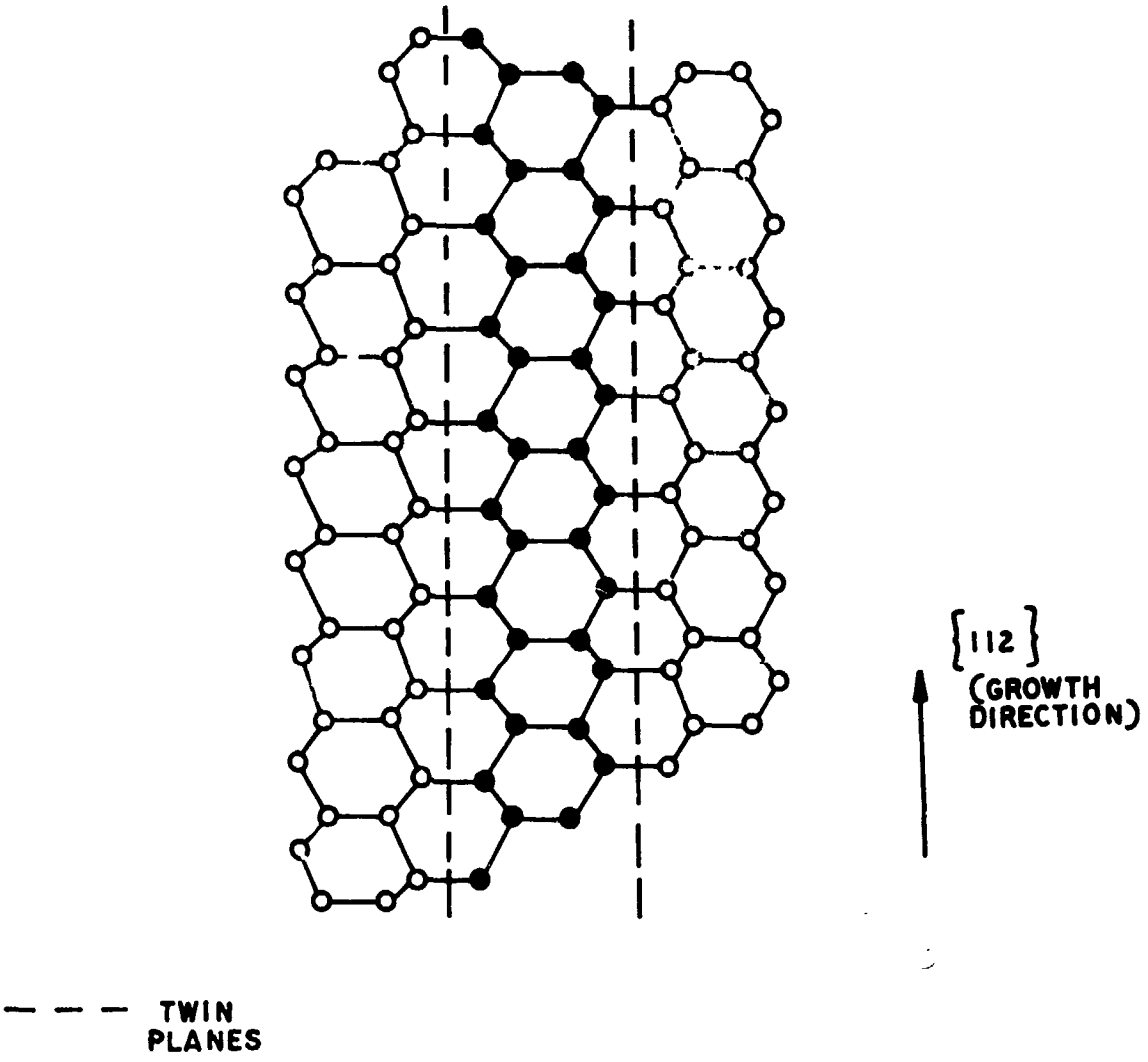

Fig. 28. {110} projection of the diamond cubic structure. The dotted lines represent twin planes. Notice the orientation relationships between the matrix and the twinned region.

Nucleation of the linear boundaries, whether they be twins or stacking faults, is very likely to be related to the presence of carbon in the material. The influence of carbon on the crystallographic quality of both melt grown and vapor deposited crystals of silicon has been well investigated.[22-24] Carbon has been shown to generate growth twins, stacking faults and, at high levels of concentration, dislocations and high angle grain boundaries in silicon crystals and films. It has been suggested that twins observed in epitaxial silicon films are a result of the packing effects of two extra (0001) SiC planes between the (111) planes of silicon. The incorporation of SiC in the form of short chains in the silicon lattice has been suggested as the nucleating mechanism for defects such as stacking faults.[25,26] The closed circles in Fig. 28 suggest the atomic configuration that carbon atoms could assume in the ribbon resulting in the insertion of extra layers composed of carbon atoms which then constitute the observed linear boundaries. Whether continuous incorporation of carbon in the form of sheets of atomic dimensions in the growing crystal is required for the propagation of the observed defect structure is not known at present. It would indeed be sufficient for carbon or SiC to nucleate the twins or stacking faults with propagation occurring as a result of growth.

Whereas the major defect types observed in EFG silicon ribbons are twins (or stacking faults), a small fraction of the structure is composed of linear arrays of dislocations often associated with the twin boundaries. Figures 29(a) and 29(b) show two examples of bands of dislocations. Frequently, deformation induced dislocations are also observed with dislocations piled up against twin boundaries.

Two likely mechanisms can be invoked to explain the morphology of the dislocations. Stress induced or grown-in dislocations can be confined to regions between twins as shown in Fig. 29. The clustering of the dislocations away from the twin bands could be a result of image or surface forces of the twin boundaries exerting a stress on the dislocations resulting in the observed morphology.

Stacking faults can be absorbed by twin boundaries by the displacement of twin planes with a displacement vector of $\frac{a}{6}[11\bar{2}]$ during crystal growth.[27] This mechanism would result in stacking faults bound by partial dislocations of the type $\frac{a}{6}\{112\}$. A high density of overlapping faults in association with the twins would result in the observed high density of dislocations proximal to the twins. An analysis of the nature of the dislocations, i.e., whether the dislocations are of the type $\frac{a}{2}\{110\}$ or partial dislocations bounding stacking faults, should shed more light

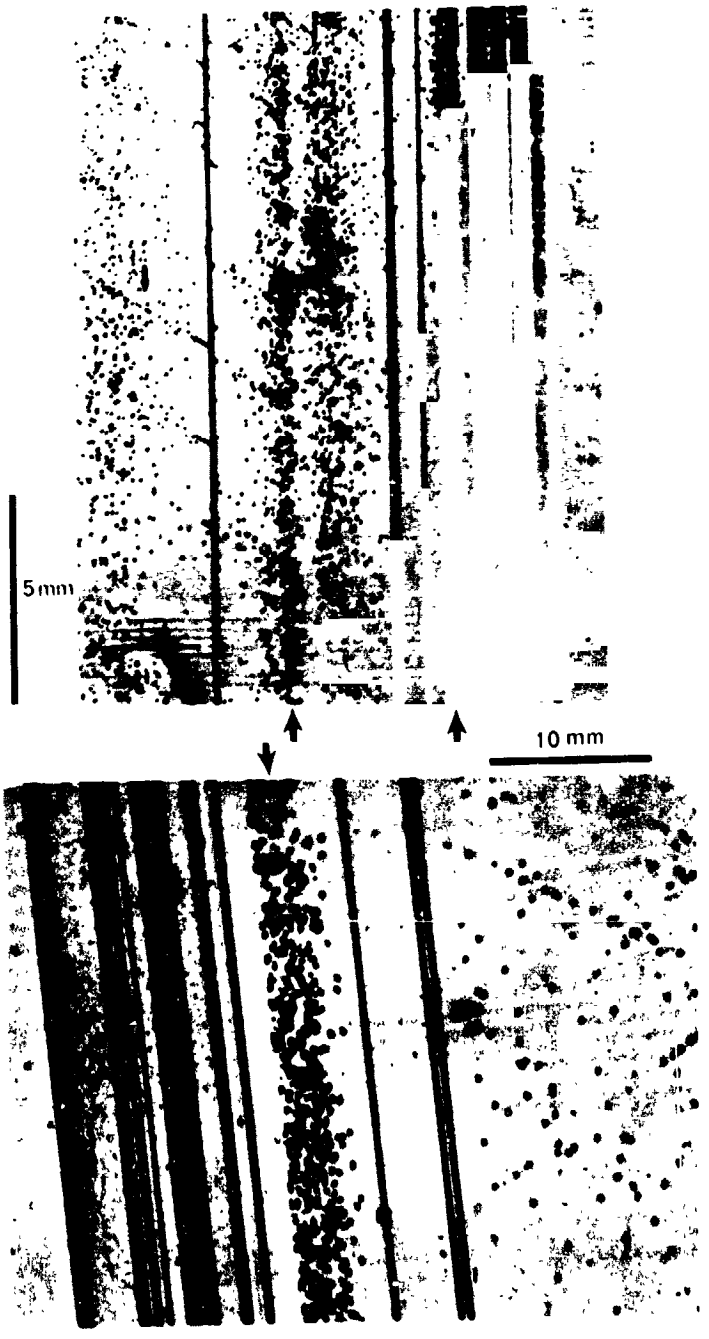

Fig. 29. Linear arrays of dislocations, often associated with twin boundaries. Arrays of dislocations between twin boundaries are stress induced, as shown in (a). In addition, clusters of dislocations, as seen in (a) and (b) are often observed. The region in the immediate neighborhood of the twin is seen to be devoid of dislocations.

on the mechanisms. The attainment of a structure consisting essentially of parallel twins parallel to the ribbon edges suggests that following the establishment of steady-state growth conditions the defect structure of the ribbons essentially reaches a steady-state equilibrium configuration.

Orientation experiments involving variously oriented seeds have been conducted with a view towards determining whether an "equilibrium defect" structure develops in EFG ribbons and if so what the effects of seed orientation would be on the establishment of such a structure.

Table VI lists the seed orientations used as part of the investigation. Seeds with (111) orientations were chosen because (111) planes are the preferred twin planes in diamond cubic materials. It has been reported that EFG silicon ribbons have a preferred surface orientation of (110).[20] (110) is a low index, high-symmetry plane. Hence, (110) seeds with different growth directions were chosen. A ribbon seed was also chosen for comparison with the (110) [211] seed.

Nine ribbon growth runs comprised the growth orientation study - a total of 32 growth attempts were made. The results are characterized below. For the orientation study, the growth process was standardized as nearly as possible. The furnace arrangement included an active one-piece ribbon face heater (this, prior to the state-of-the-art conversion described earlier) as well as the crucible main heater. A flat molybdenum heat shield sat on insulating stand-offs on the face heater. A two-piece graphite die with a 12 in. radius of curvature was used for all these orientation runs. Growth was from a 3 in. diameter quartz crucible contained in a graphite shell. Detailed growth run data and results are presented in previous Technical Progress Reports of this program.[13, 14]

The following observations were made during growth of these ribbons: the defect and surface structure of the ribbons are best where the ribbon is growing stably at full width, and at ~0.8 in./min; (110) [111] growth is very active right after seeding and the structure breaks down dramatically; (111) [110]; (111) [211]; (100) [110] liquid-solid interfaces are unstable and display facetting; (110) [211]

Table VI. Expected Ribbon Surface Orientations and Growth Directions after Twinning.

Seed Orientation	Twinning Plane	Orientation after Twinning	
(110) [1$\bar{1}$1]	(111)	($\bar{1}\bar{1}$4)	[1$\bar{5}$1]
	(1$\bar{1}$1)	(110)	[$\bar{1}$1$\bar{1}$]
	($\bar{1}\bar{1}$1)	($\bar{1}\bar{1}$4)	[5$\bar{1}$1]
	(1$\bar{1}\bar{1}$)	(110)	[1$\bar{5}$]
(100) [011]	(111)	(1$\bar{2}\bar{2}$)	[$\bar{4}\bar{1}\bar{1}$]
	(1$\bar{1}$1)	(12$\bar{2}$)	[011]
	($\bar{1}\bar{1}$1)	(1$\bar{2}$2)	[011]
	($\bar{1}$11)	(122)	[4$\bar{1}\bar{1}$]
(110) [$\bar{1}$12]	(111)	($\bar{1}\bar{1}$4)	[$\bar{7}$12]
	(1$\bar{1}$1)	(110)	[$\bar{1}$12]
	($\bar{1}\bar{1}$1)	($\bar{1}\bar{1}$4)	[172]
	($\bar{1}$11)	(110)	[5$\bar{5}\bar{2}$]
(110) [1$\bar{1}$0]	(111)	($\bar{1}\bar{1}$4)	[1$\bar{1}$0]
	(1$\bar{1}$1)	(110)	[$\bar{1}$1$\bar{4}$]
	($\bar{1}\bar{1}$1)	($\bar{1}\bar{1}$4)	[1$\bar{1}$0]
	(1$\bar{1}\bar{1}$)	(110)	[$\bar{1}$14]
(111) [1$\bar{1}$0]	(111)	($\bar{1}\bar{1}\bar{1}$)	[1$\bar{1}$0]
	(1$\bar{1}$1)	(151)	[$\bar{1}$1$\bar{4}$]
	($\bar{1}\bar{1}$1)	(115)	[1$\bar{1}$0]
	(1$\bar{1}\bar{1}$)	(511)	[$\bar{1}$14]
(111) [$\bar{2}$11]	(111)	($\bar{1}\bar{1}\bar{1}$)	[$\bar{2}$11]
	($\bar{1}$1$\bar{1}$)	(151)	[$\bar{2}\bar{1}$7]
	($\bar{1}\bar{1}$1)	(115)	[$\bar{2}\bar{7}\bar{1}$]
	($\bar{1}$11)	(511)	[$\bar{2}\bar{5}\bar{5}$]

single crystal seeds most commonly lead to growth with twins parallel to the growth direction and a smooth interface; the unstable 'orientation seeking' period between initiation of growth and steady-state growth is greatly reduced when seeded from EFG ribbons, effectively (110) [211], containing twins parallel to each other and to the growth direction (the equilibrium defect structure described below).

A silicon crystal with a known surface orientation, growing along a given crystallographic direction shows first order twin traces on the ribbon surface such as those presented in Fig. 30; Table VI lists the ribbon surface orientations and growth directions following twinning on the appropriate (111) planes for the selected seed orientations. Such twin traces have been seen in that part of the ribbon which is proximal to the seed. However, interactions between primary twins leads to higher order twin generation, with a rapid breakdown of the simple matrix-twin relationships. The crystal achieves the "equilibrium" state wherein a majority of the linear boundaries lie parallel to each other, and parallel to the direction of crystal growth.

In order to establish the "equilibrium" orientation, X-ray Laue patterns were obtained at points on the ribbon, one foot and two feet from the seed. The orientations were determined across the ribbon width at eight equidistant points at each of these regions. As an example, Figs. 31(a) and 31(b) show two X-ray patterns taken two feet from the seed in ribbons 14-149-3 (seed orientation: (111) [110]) and 14-154-3 (seed orientation: (111) [211]). From patterns such as those in Fig. 31, it was deduced that the predominant orientation of EFG silicon ribbon approximates to (110) [211]. Fig. 32(a) is a selected area electron channeling pattern (SAECP) from a region exhibiting the equilibrium structure and is compared to a similar pattern from the (110) [211] seed in Fig. 32(b). Note the similarities in the diffraction patterns. This preferred orientation was observed in all the ribbons after about one foot of growth, irrespective of the seed orientation. Fig. 33 shows the orientation at the end of 2 feet of growth in sections of various seed orientations. Note the clustering of ribbon orientation near the (110) pole. The position at which the equilibrium structure is established was found to be dependent on the seed orientation. Figs. 34 and 35 show regions of ribbons near the seed for the (111) [110] and (111) [211] seed orientations, respectively. These show predominantly first order twin generation. However, the stable defect configuration is not achieved in these cases till much later in the growth process. In contrast, the stable orientation

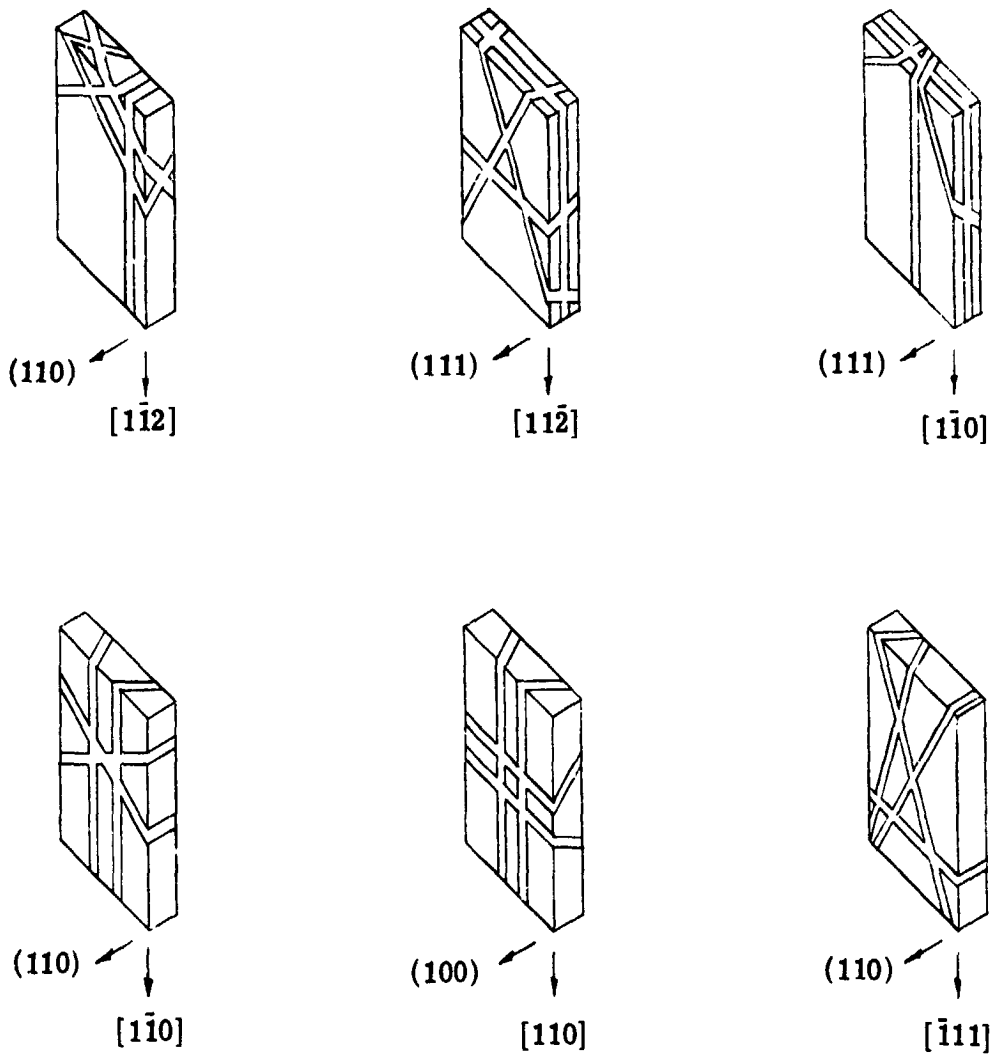

Fig. 30. Schematic of principal twin systems in silicon relative to frequently used seed and growth orientations. (After Leipold, et al. Proc. IEEE Photovoltaic Spec. Conf. Rec. 11th, 1975).

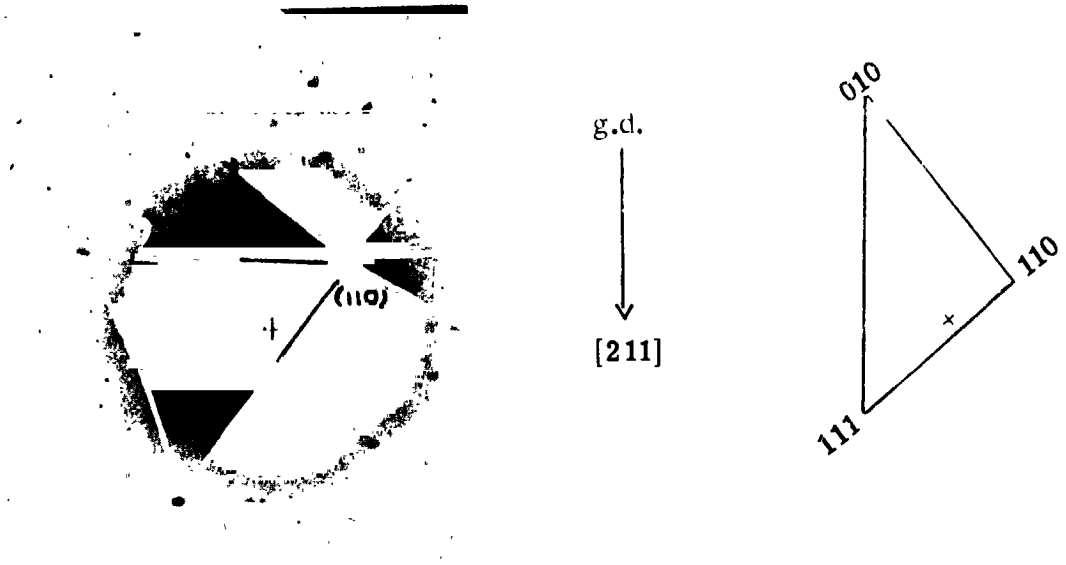

(a)

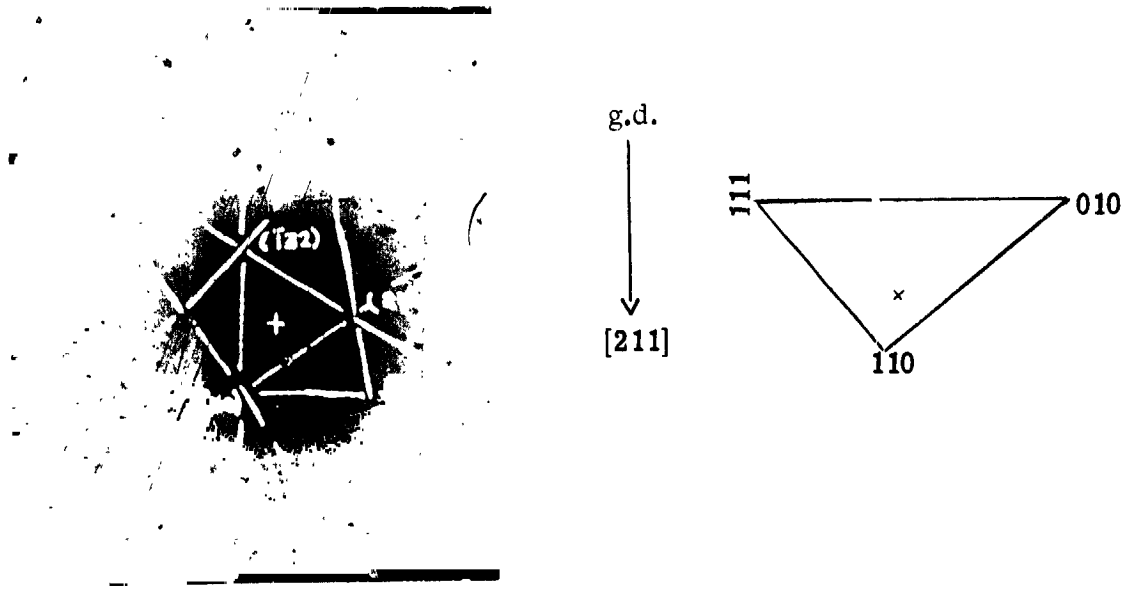

(b)

Fig. 31. Orientation of ribbon two feet from the seed: (a) seed orientation: (111) [110]; (b) seed orientation: (111) [211]. The predominant orientation is close to (110) [211], irrespective of seed orientation.

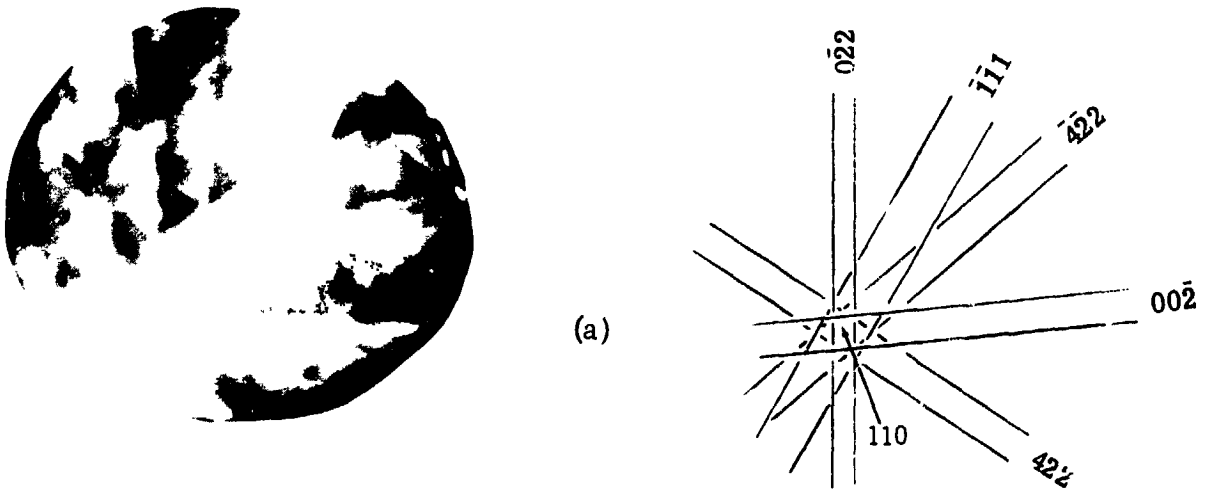

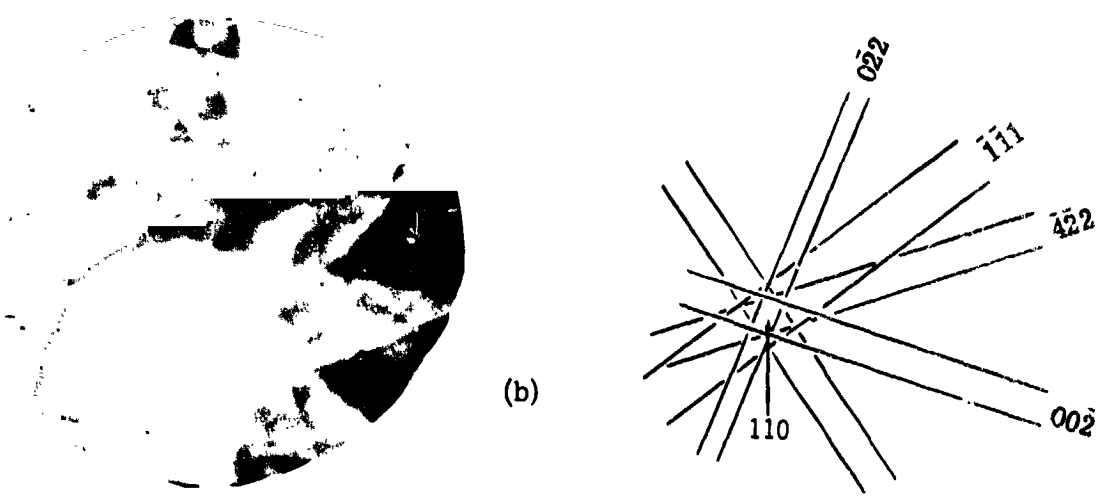

Fig. 32. Selected area channeling patterns from (a) the equilibrium structure and (b) (110) [211] seed. Note the similarity in the two patterns, suggesting that the equilibrium structure is close to a (110) [211] orientation.

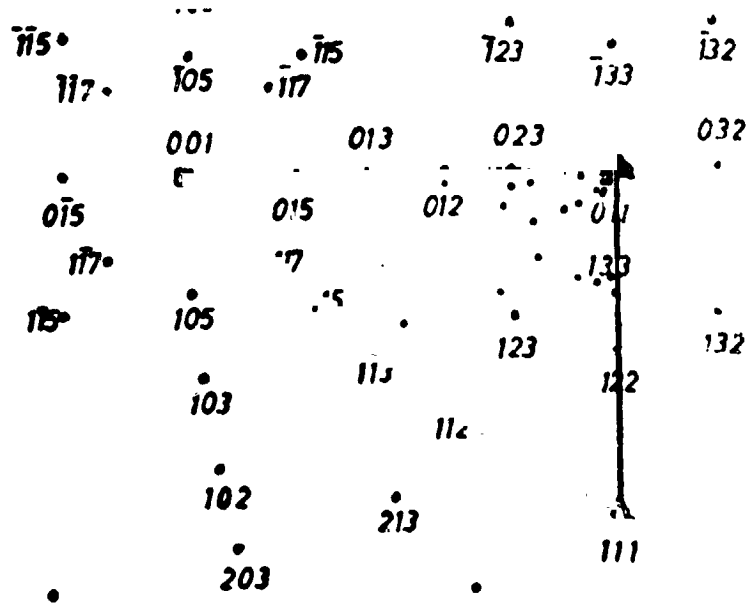

Fig. 33. Orientations of ribbons grown from the various seeds. The ribbon samples were two feet from seed. Spots in stereographic projection correspond to the ribbon surface orientation. Notice the clustering near the (110) pole.

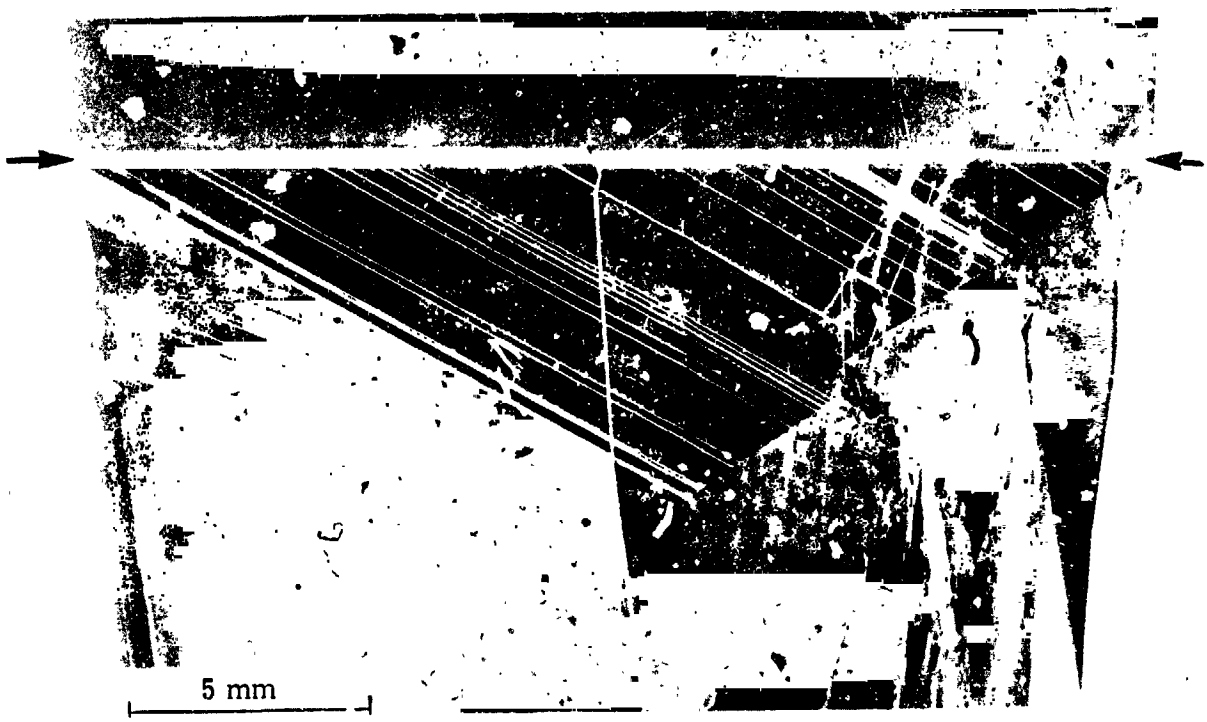

Fig. 34. First order twin generation in ribbon next to seed (orientation of seed: (111) [110]). This seed orientation gives rise to intersecting boundaries initially. However, twin reactions lead to the generation of parallel twins and the equilibrium structure, as the crystal grows. Arrow indicates seed-crystal interface.

Fig. 35. First order twin generation in ribbon next to seed (orientation of seed: (111) [211]). Arrows indicate seed-crystal interface. Note that there are no parallel boundaries, parallel to the crystal growth direction. Parallel boundaries form as crystal grows, and the equilibrium structure is eventually attained. Note also the generation of slip bands in both ribbon and seed.

forms immediately after seeding when either the (110) [211] seed or a ribbon seed is used. Figures 36 and 37 show ribbon starts using such orientation seeds.

In order to further examine the twinning orientations possible, a region close to the seed was chosen since the initial twin traces should correspond to first order twins making comparisons with theoretical predictions feasible. The seed orientation was (111) [110]. Figure 38 is an example of such a region. It was found that the orientation of regions 1 and 2 was (111), while region 3 had a (511) orientation. Thus region 3 is a first order twin obtained after twinning on the (111) planes. Regions 1 and 2 have the same orientation. This can be due to (i) both regions being related in a matrix-twin relation, or (ii) the linear boundary separating the two areas may be composed of multiple twins. A high magnification photograph of the twinned region does not clearly reveal the multiple-twin nature of the boundary.

In addition to twins and dislocations, discrete particles and clusters of particles of SiC are also observed in ribbons grown with the use of carbon dies.[28] These particles are postulated to be formed as a result of the rejection of supersaturated carbon by the solidifying liquid, the attendant precipitation of the carbon in the form of SiC on the die top and the subsequent incorporation of the particles in the growing ribbon as a result of the particles reaching the solid-liquid interface and being extracted by the solid. Although by employing a high meniscus, the incorporation of SiC particles can be minimized in the initial stages of growth, with sustained growth the particle dimensions eventually approach the dimensions of the meniscus and particle incorporation is resumed. The influence of the particles on the electrical properties of the ribbons has been investigated and it has been determined that the electrical activity of the particles is largely a function of the presence of lifetime reducing impurities around them.

2. Electrical characteristics

With the relatively high density of defects and the presence of lifetime reducing impurities the electrical characteristics of EFG ribbons are not comparable to conventional Czochralski crystals. Typical minority carrier diffusion lengths in these crystals range from 20 μM to 70 μM with typical Czochralski values being generally in excess of 100 μM. The importance of these numbers lies not in their lower magnitudes but in their relative non uniformity. The non uniformity of diffusion length will impact the yield of the final product. In order to assess the contribution of the various defect types to the reduction in the diffusion length, a variety of

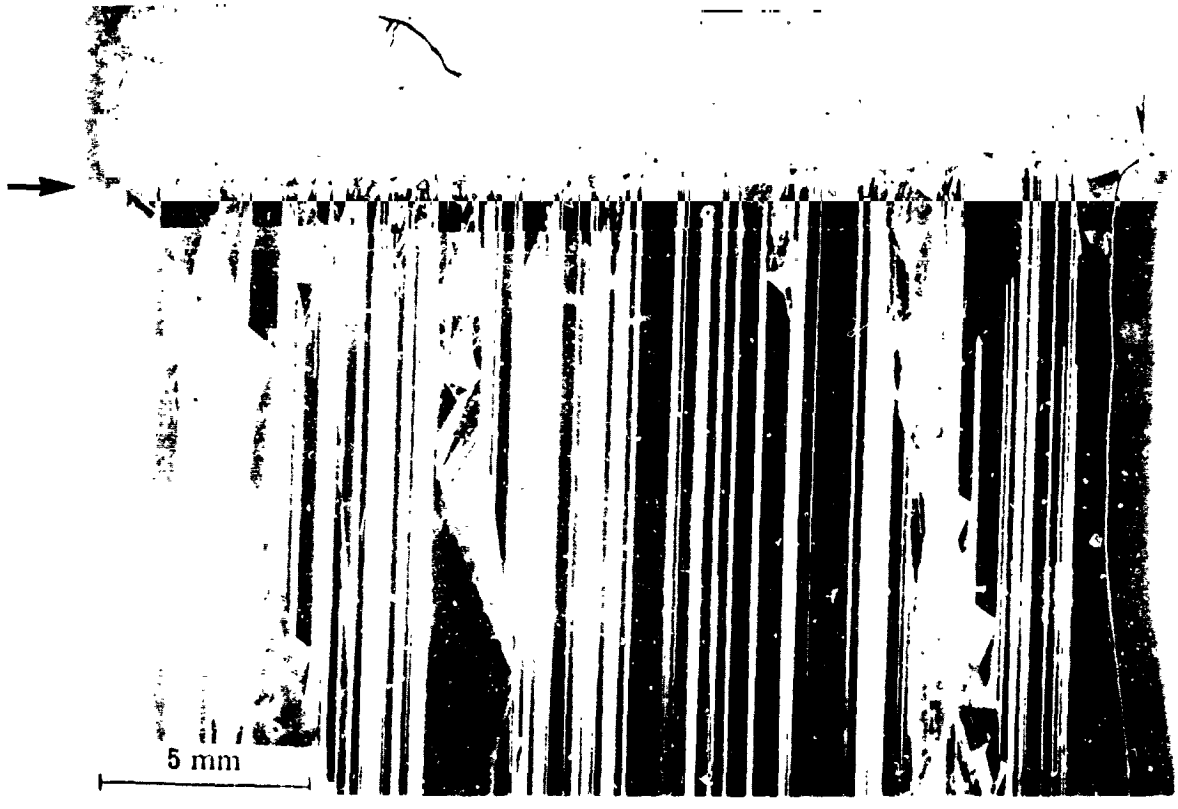

Fig. 36. Generation of parallel twin boundaries next to the (110) [211] seed. Arrows indicate seed-crystal interface. The (110) [211] seed orientation gives rise to parallel twins immediately after seeding. The few intersecting boundaries seen transform, as a result of twin interactions, into the equilibrium structure as the ribbon grows.

Fig. 37. Generation of parallel twin boundaries next to the ribbon seed. Arrows indicate the seed-crystal interface. As can be seen, the linear boundaries in the seed propagate into the growing ribbon. Observe some of the intersecting boundaries generating parallel twins. The structure very quickly attains the equilibrium orientation in this case.

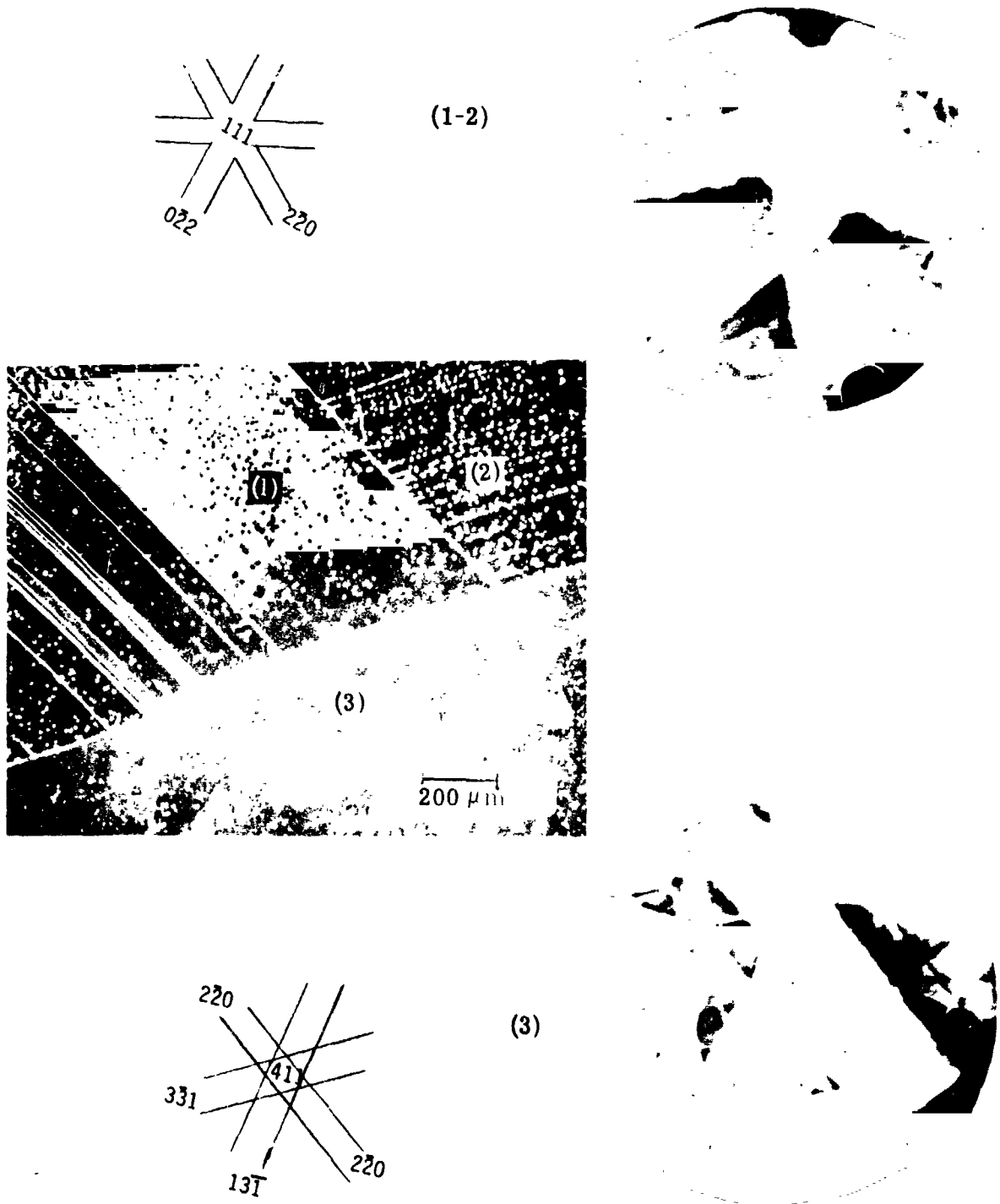

Fig. 38. Region of ribbon near the seed. Seed orientation was (111) [110]. Primary twinning on (111) planes can be seen. Regions 1 and 2 have the same orientation, i.e., (111), while region 3 has the (511) orientation. These orientations conform to those expected for the given seed orientation.

experimental techniques have to be utilized. Details of many of the measurements made have been presented elsewhere.[29-32] In this section a brief discussion of the electrical activity of the linear boundaries and a discussion of solar cell characteristics will be presented.

3. Electrical activity of defects

The influence of the linear boundaries on electrical parameters and solar cell characteristics has been investigated to determine the degree to which the defects adversely affect the conversion efficiencies of solar cells.[29,31] A very effective method for the investigation of the electrical activity of crystallographic defects in semiconductors is the use of the scanning electron microscope operated in the electron beam induced current (EBIC) mode.[33] This technique has been extensively utilized for the investigation of EFG ribbons.[28,34] Figures 39(a) and (b) show examples whereby the EBIC technique permits the imaging of electrically active defect boundaries. In Fig. 39(a) are shown secondary electron and EBIC images of a region of a solar cell fabricated in a silicon ribbon. The secondary electron display shows very little structure on the ribbon surface whereas the EBIC image shows a number of dark line defects which correspond to linear boundaries which are electrically active, the dark contrast (or dark-white contrast)[35] being a result of local recombination of beam generated carriers. Figure 39(b) shows a magnified EBIC image of another solar cell where the two types of defect boundaries discussed in the previous section are identifiable. Linear twin boundaries displaying sharp contrast and the arrayed bands of dislocations which also function as regions of strong recombination are observed. The sharply delineated twin bands are also seen to be associated with dislocations. This fact is more clearly evident in Fig. 40. Figure 40(a) is an EBIC image of a region of a solar cell. A single linear boundary is observed to function as a region of strong recombination. Figure 40(b) is a secondary electron display of the preferentially etched surface of the same region as in (a). The arrows identify the electrically active boundary in the micrographs. In addition to the single electrically active boundary, a high density of electrically inactive boundaries is observed in (b) with none of them functioning as recombination centers as evidenced by their non-detectability with the EBIC mode of observation. Close examination of Fig. 40(b) permits the distinction between electrically active and electrically inactive boundaries to be made. The electrically active boundary is found to be composed of

(a)

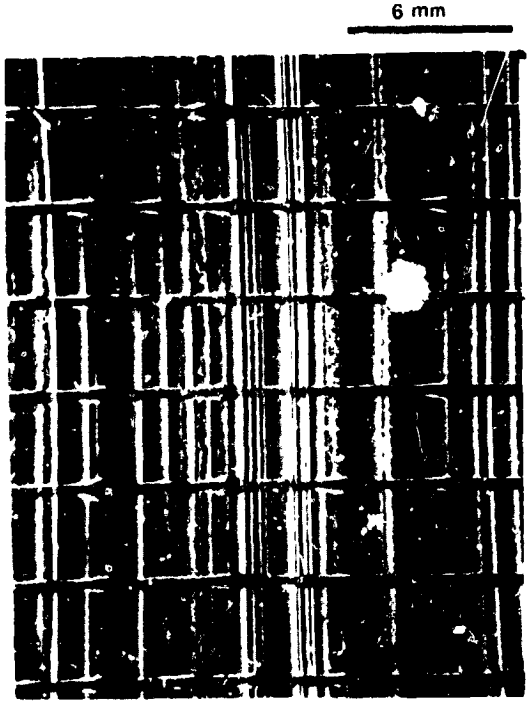

(b)

Fig. 39. (a) Secondary electron and EBIC images of a solar cell. Note the lack of structure in the secondary electron image (picture on the left). The same area, in the EBIC mode, reveals marked contrast associated with regions of carrier recombination. In (b) are seen two types of defects that lead to strong recombination: twin bands with associated dislocations, and dislocation arrays.

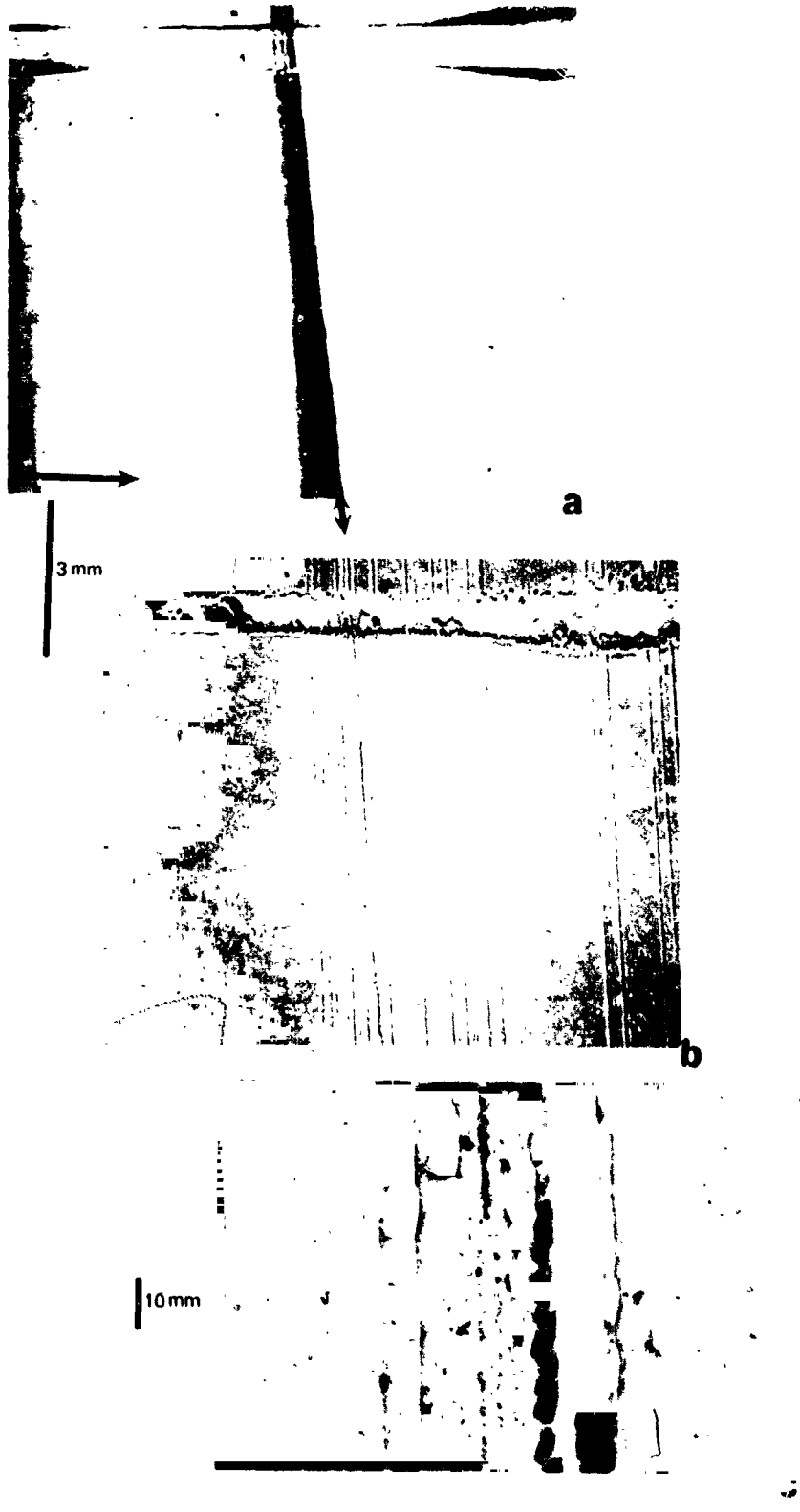

Fig. 40. EBIC (a) and secondary electron (b) images of a region of a solar cell. Only a single linear boundary, as shown by arrow, is electrically active. Other linear boundaries are electrically inactive. A higher magnification image of the electrically active boundary in (c) shows that this boundary has dislocations associated with it.

dislocations possibly in association with twins, whereas no dislocations are observed in the vicinity or at the other linear boundaries. Figure 40(c) is a higher magnification secondary electron image of the electrically active boundary showing the high density of etch pits due to dislocations. Both arrayed dislocations as well as discrete randomly dispersed dislocations have been observed to reduce the beam generated current in these crystals whereas the twins are largely electrically inactive.

The strong recombination contrast observed at the defect boundaries is related to defect impurity association at these regions. Although clean, undecorated dislocations have been postulated to function as donors and acceptors in silicon it is very unlikely that significant recombination can occur in the absence of an impurity at the dislocations. It has been documented that strong EBIC contrast is observed only when the defects are associated with impurities.[35-37] Consequently the dislocation arrays which are the primary electrically active defect species in the ribbons are undoubtedly decorated with a deep level impurity (or impurities) rendering them electrically active.

With decorated dislocations and dislocation arrays being implicated as the principal lifetime reducing defect types in EFG ribbons, the avenues of approach to be followed for quality improvements are discernable. An overall reduction in the undesirable impurity content in these crystals should result in significant improvement. In addition to reducing the impurity content of graphite dies the approach is largely one of increasing component and machine purity. A reduction in the dislocation density with particular reference to arrayed dislocations should also improve electrical quality. The methods to be adopted to reduce the dislocation density would largely be determined by the mechanisms responsible for the introduction of dislocations in these crystals. If dislocation generation is related to thermal stress in the crystals during growth, the establishment of appropriate thermal environments can reduce the dislocation density. On the other hand if dislocation introduction is a result of the presence of carbon in the crystals with perhaps the dislocations largely being partial dislocations in association with stacking faults the solution to the problem becomes much less tractable. Evidence to date, although insufficient, suggests that a significant fraction of the dislocations are stress induced.

An unanswered question is the effect of carbon in terms of directly influencing the electrical behavior of EFG ribbons. Although carbon, unlike oxygen, is a neutral impurity in silicon, the high growth rates characteristic of the EFG process may result in the occupancy of carbon atoms in other than substitutional sites, or the association of carbon with oxygen, vacancies or other impurities resulting in electrically active complexes. Further work is required to assess the importance of such effects if they exist.

4. Impurity distribution

The large surface to volume ratio of the ribbons and the high vertical temperature gradients present during growth have an effect on the distribution of the dopant and impurities through the thickness of the ribbons. In addition, the position of the feeds slots in the die which convey the liquid to the die top affect the distribution of impruities and the dopant across the width of the ribbons.[6] For steady-state growth with a quiescent liquid and sufficient temperature gradient in the liquid to avoid constitutional supercooling, each solute will have a concentration profile in the liquid from a maximum of C_o/k_o at the interface, decreasing exponentially to C_o, the concentration in the melt. The concentration decreases to 1/e of its maximum value at a distance D/V_g from the interface, where D is the diffusion coefficient of the solute in the liquid and V_g is the growth rate. The question to be resolved is whether the lateral flow of melt in the growth film causes any significant lateral movement of the solute, either impurity or dopant, resulting in concentration gradients of the solute across the ribbon width or through the thickness. Examination of this effect for various solutes and various die geometries has shown that a heterogeneous distribution of impurities is possible in EFG ribbons as a result of liquid flow effects.[6]

In addition to liquid flow effects, solid state diffusion of impurities to surfaces (both external and internal as represented by defects) is possible. By employing the surface photovoltage technique of determining the minority carrier diffusion length in EFG ribbon solar cells, it has been determined that the minority carrier lifetime is generally different in the near surface regions of the material as compared to that in the bulk.[30] This suggests that an impurity gradient through the thickness can exist in these crystals.

In order to examine the variations in concentration of the impurities along the width and through the thickness of ribbons spreading resistance measurements were undertaken.

A bevel was ground and the surface polished using standard polishing techniques. The bevel angle used was $2^{0}52'$, which leads to an apparent magnification on the bevelled surface of 20. The length of the bevelled region was typically 5 to 6 mm. If the thickness of the ribbon is 0.2 to 0 25 mm (0.008 to 0.010 inches), this would correspond to approximately 0.2 mm (0.008 inches) of the thickness of the material removed. Two types of scans were made:

1. along the ribbon width (approximately 2.54 cm),

2. across the thickness and along the bevel, with L, C, and R referring to left, center and right scans respectively.

The scheme followed is shown in Fig. 41. Probe steps of 10, 25 and 50 μm were employed; both single- and double-probe scans were used. Carrier concentration was plotted, from Irvin's curves,[38] as a function of distance traversed.

Figure 42 shows the carrier concentration in a ribbon grown from unbaked graphite dies. The ribbon was doped with boron to yield a resistivity of 1 Ω-cm, which corresponds to carrier concentrations of 2×10^{16} to 3×10^{16} atoms/cc. The spreading resistance data shows the carrier concentration varying along the ribbon width by as much as two orders of magnitude. This is to be expected in silicon grown from impure dies, where a preferential segregation of impurities to structural defects may occur. Use of purified graphite components, reduces the fluctuations in resistivity (or, carrier concentration), as shown in Fig. 43. Small fluctuations in carrier concentration can be decreased by appropriate high temperature anneal or gettering during solar cell fabrication. Fig. 44(b) shows the profile in a sample from the same ribbon as in Fig. 44(a), after high temperature (~950°C) junction fabrication leading to the formation of a n^{+} (phosphorus) layer. The junction depth was approximately 0.5 μm observed through the thickness of the material.

In order to examine the factors responsible for variations of resistivity in the material, samples were examined by optical microscopy after final polishing and after a preferential silicon etch. The region marked on the right in Fig. 42 was re-examined by using 10 μM probe steps (see Fig. 45a); the polished surface was also observed with an optical microscope. The surface relief in the optical micrograph of Fig. 45(b) occurs due to the variation in chemical polishing characteristics with resistivity. The presence of a grain boundary leads to an increase in

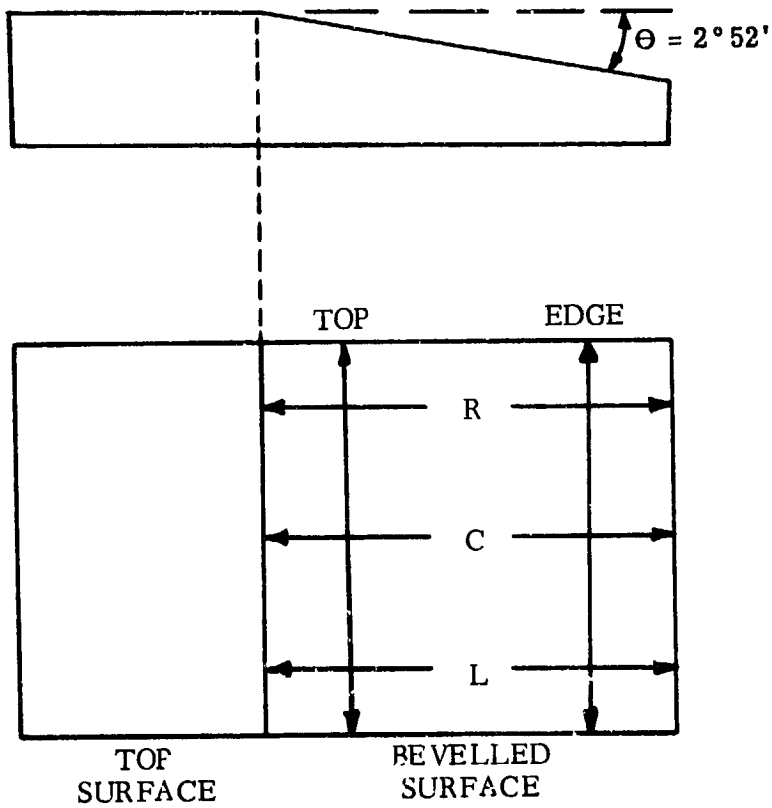

Fig. 41. Scheme followed for spreading resistance measurements. L, C and R refer to traces down the bevelled surface, i.e., into the sample bulk.

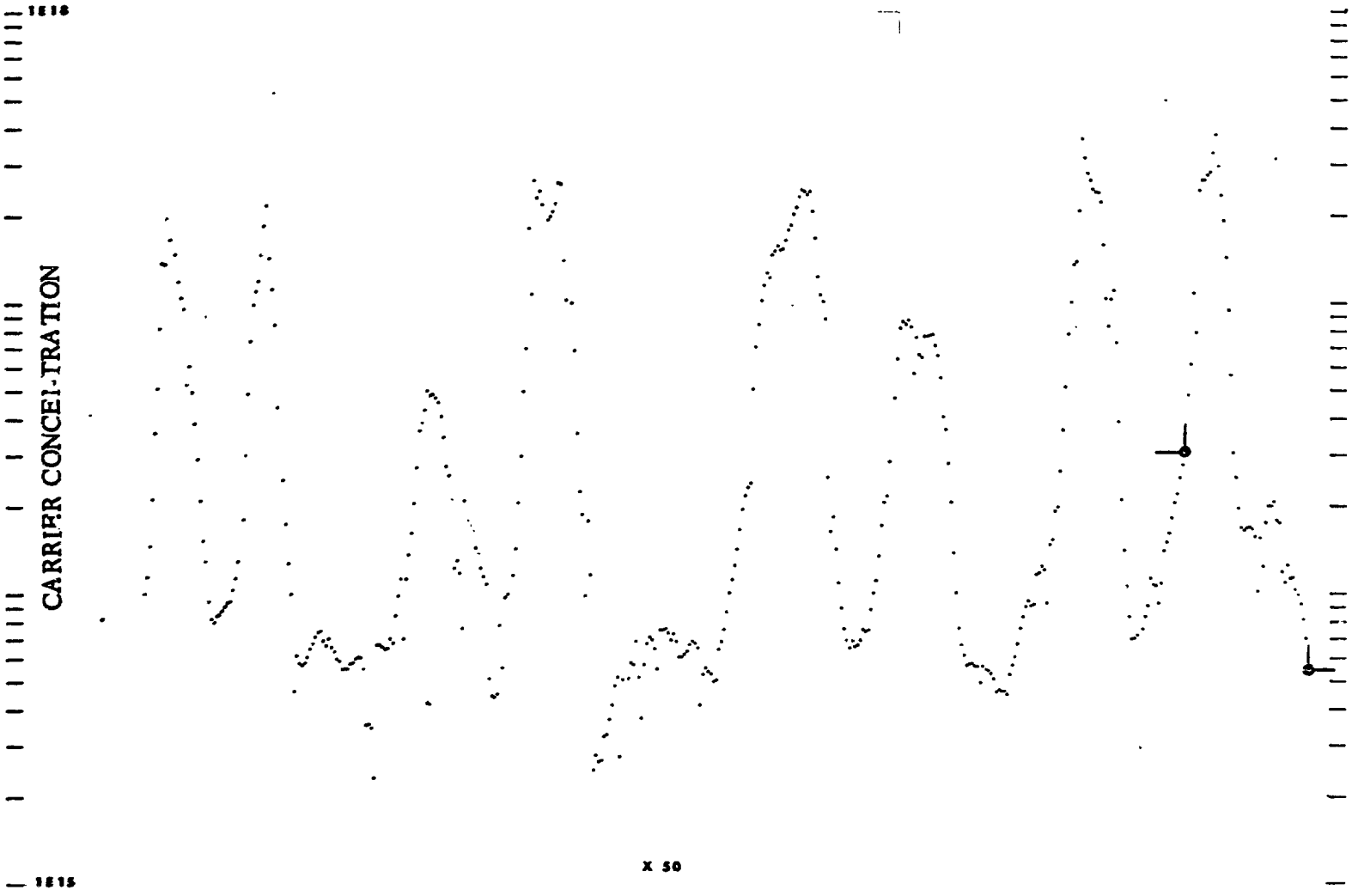

Fig. 42. Carrier concentration along the ribbon width. Ribbon was grown using unbaked graphite components. Probe steps are 50 μM apart. Note the large fluctuations in carrier concentration.

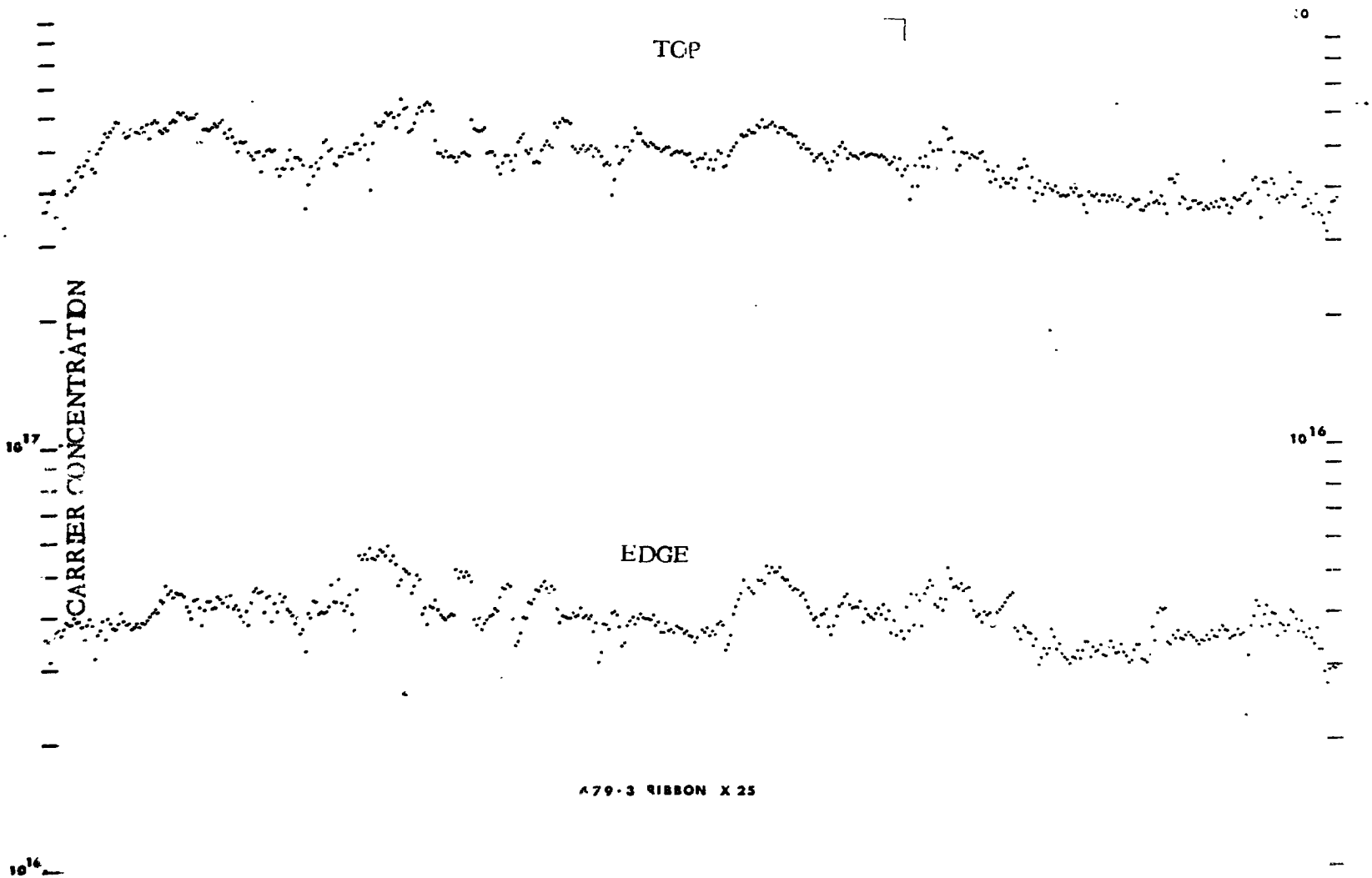

Fig. 43. Carrier concentration along ribbon width when ribbon is grown from baked graphite components. The amplitude of fluctuations in carrier concentrations are smaller than in ribbon grown from unbaked components. ('Top' and 'Edge' are defined in Fig 41).

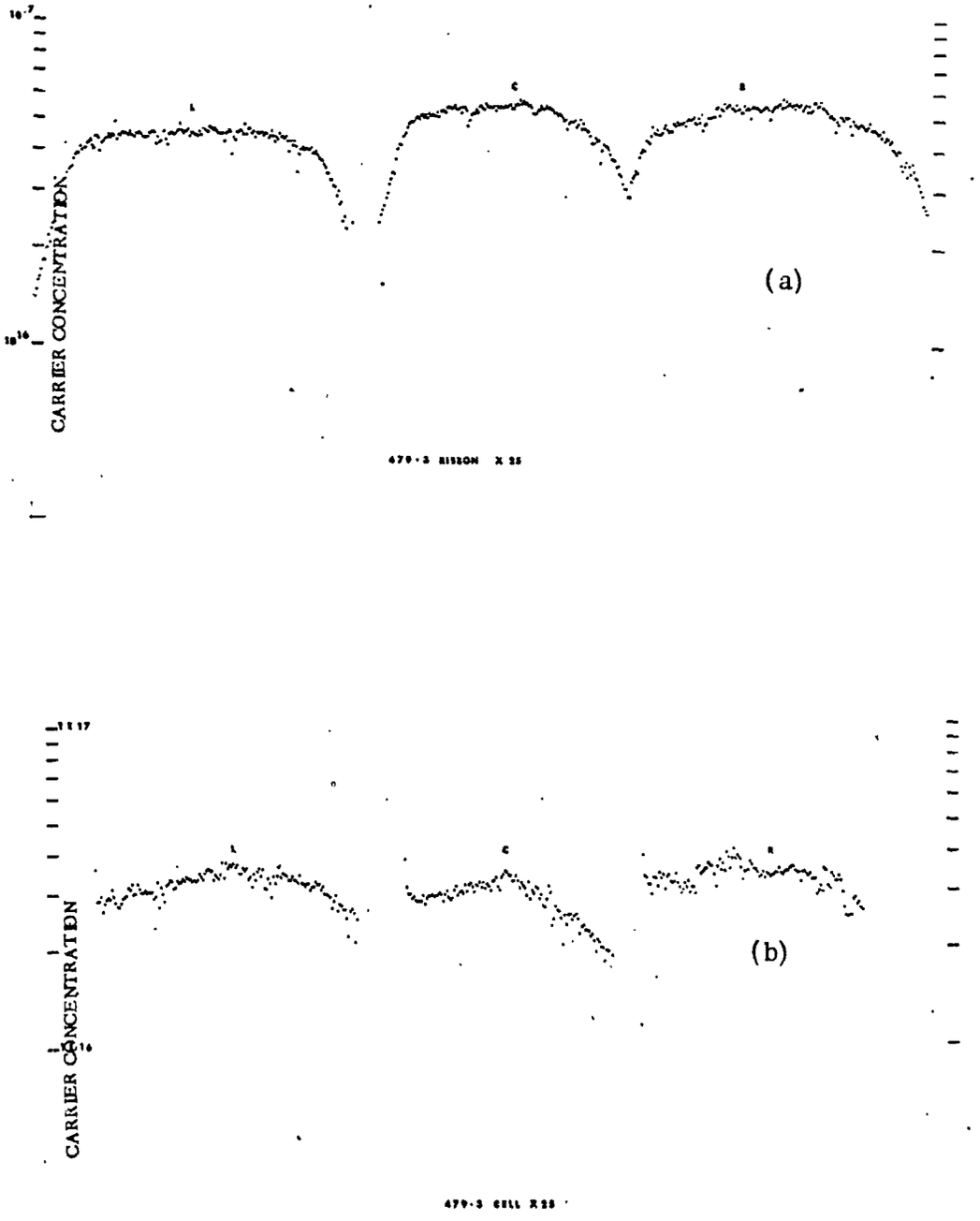

Fig. 44. Spreading resistance profile of as-grown ribbon. (a) shows the variation in carrier concentration, at three places, along the thickness of ribbon. Solar cell fabrication reduces the bulk concentration gradient, as seen in (b).

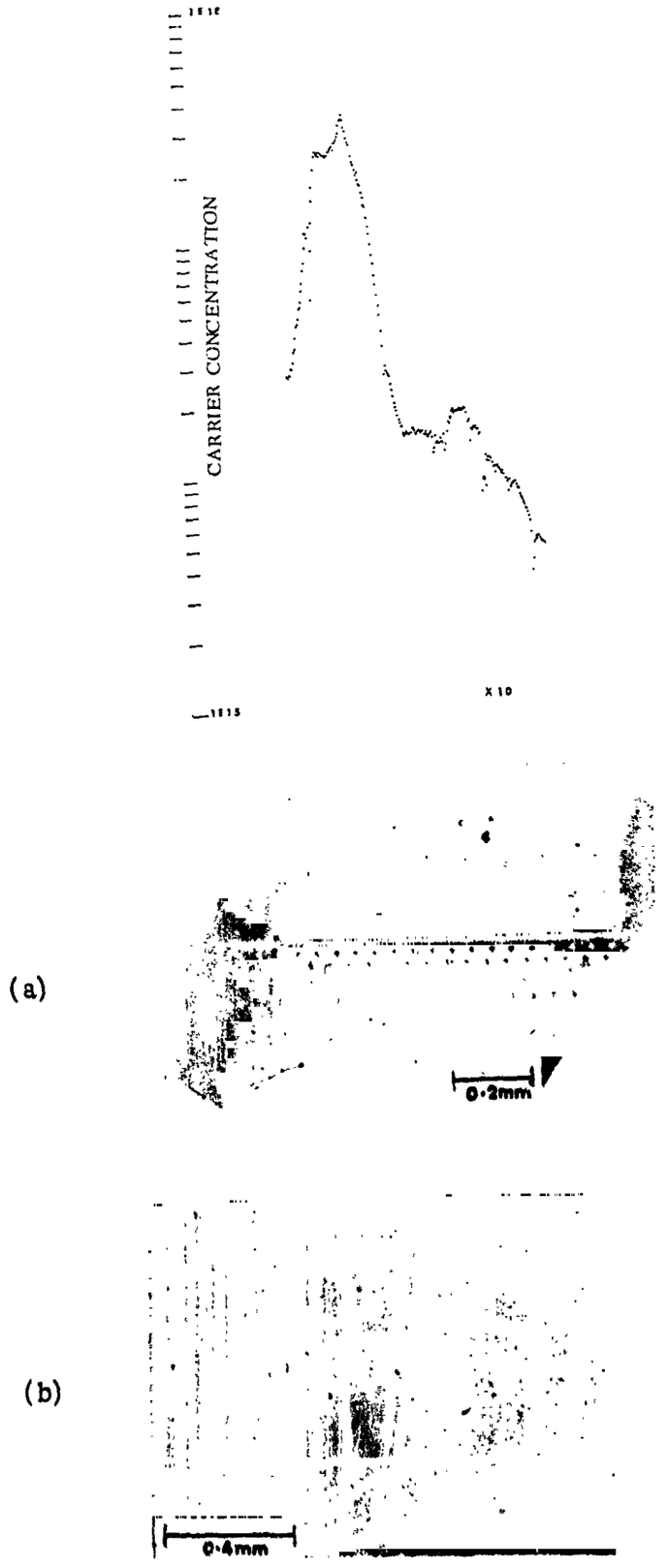

Fig. 45. (a) Magnification of spreading resistance plot of right hand region of Fig. 42. Probe steps are 10 μM apart. (b) shows surface relief on as-polished ribbon surface, showing presence of a grain boundary. (c) is the same area after preferential etching. Notice that not all grain boundaries cause a change in carrier concentration.

carrier concentration. Fig. 45(c) shows an optical micrograph of the same area after preferential etching. Note the presence of grain boundaries and dislocations, which do not seem to change the resistivity markedly. Thus, not all grain boundaries act as gettering sites for impurities. However, grain boundaries that do not change the resistivity appreciably (Fig. 46c) may act as effective recombination sites as evidenced in Fig. 46(b), which is a Schottky barrier EBIC scan of the same area, preferentially etched, as in Fig. 46(a).

It was observed that the carrier concentration both increased and decreased near grain boundaries. It is possible that such variations may be due to the differences in the nature of the grain boundaries. The regions of a ribbon with high dislocation densities showed a general reduction of the carrier concentration.

E. Problems

None.

F. Plans

Technical milestones for the last six months of this program include achieving growth rates of 7.5 cm/min (March 31, 1977), growth of 7.5 cm wide ribbon (Feb. 28, 1977), growth of 0.1 mm thick ribbon (Nov. 30, 1976) (Table VII). Emphasis on achieving the last of these goals is reduced. The programs to achieve high growth rates and wide ribbon described in the body of this report will continue on Machines JPL No. 2 and JPL No. 1 respectively. Concurrent studies of ribbon stress, solar cell characteristics, feasibility of melt replenishment and system purity will supplement the growth efforts.

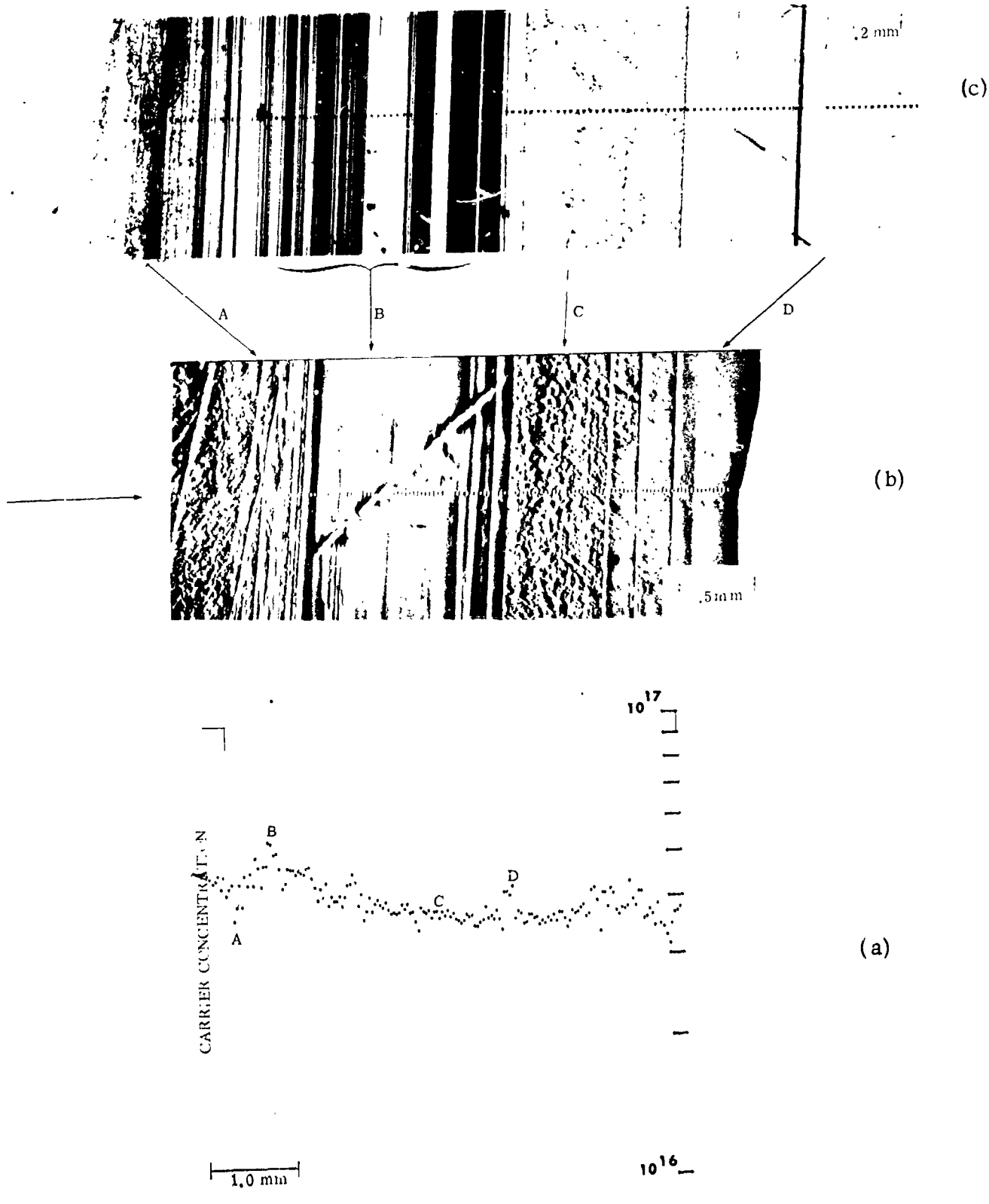

Fig. 46. Comparison between defect morphology (a) Schottky barrier EBIC scan (b) and spreading resistance (c). Crystallographic defects that act as effective recombination centers do not necessarily change carrier concentration.

III. REFERENCES

1. A.D. Morrison, "Scale-Up of Program on Continuous Silicon Solar Cells", Final Report, NSF Grant GI 43873, September, 1975.

2. LSSA Project, First Annual Report, JPL Doc. No. 5101-3, ERDA/JPL-1012-76/5 (August, 1976).

3. T. Surek, "Thermal Stress in Silicon Ribbon Structures", Proc. of LSSA Task 2 Seminar, Jet Propulsion Laboratory, July 27, 1976.

4. G.F. Hurley and J.T.A. Pollock, Met. Trans. 3, 397 (1972).

5. W.R. Runyan, "Silicon Semiconductor Technology", McGraw-Hill (New York, 1965).

6. B. Chalmers, et al., "Continuous Silicon Solar Cells", Final Report No. NSF/RANN/SE/GI-37067 X/FR/75/1, August, 1975.

7. J.C. Swartz, T. Surek and B. Chalmers, J. Electron. Mater. 4, 255 (1975).

8. "Handbook of Heat Transfer", edited by W.M. Rohsenow and J.P. Hartnett, McGraw-Hill (New York, 1973).

9. W.M. Kays, "Convective Heat and Mass Transfer", McGraw-Hill (New York, 1966).

10. B.A. Boley and J.H. Weiner, "Theory of Thermal Stresses", John Wiley (New York, 1960).

11. G. Horvay, J. Appl. Mechanics 75, 87 (1953).

12. G. Horvay, J. Mech. Phys. Sol. 5, 77 (1957).

13. A.D. Morrison, et al., "Large Area Silicon Sheet by EFG", Second Quarterly Progress Report, ERDA/JPL 954355/76-1 (March 1976).

14. A.D. Morrison, et al., "Large Area Silicon Sheet by EFG", Third Quarterly Progress Report, ERDA/JPL 954355/76-8 (June 1976).

15. T. Surek and D. Bliss, Mobil Tyco Solar Energy Corp., unpublished research (1975).

16. H.E. Bates, Mobil Tyco Solar Energy Corp., unpublished research (1975).

17. J.R. Patel and A.R. Chaudhuri, J. Appl. Phys. 34, 2788 (1963).

18. A. Seeger and K.P. Chik, Phys. Stat. Sol. 29, 455 (1968).

19. D.N. Jewett and B.H. Mackintosh, Mobil Tyco Solar Energy Corp., unpublished research (1976).

20. L.C. Garone, C.V. Hari Rao, A.D. Morrison, T. Surek and K.V. Ravi, Appl. Phys. Lett. 29, 511 (1976).

21. A.D. Morrison, "Large Area Silicon Sheet by EFG", 1st Quarterly Progress Report, ERDA/JPL 954355 December, 1975.

22. A.L. Booker and B.A. Joyce, Philos. Mag. 14, 301 (1966).

23. Y. Avigal and M.S. Schieber, J. Cryst. Growth, 9, 127 (1971).

24. P. Rai-Choudhury, J. Electrochem. Soc. 118, 7 (1971).

25. D.P. Miller, S.B. Watelski and C.R. Moore, J. Appl. Phys. 34, 2813 (1964).

26. L.D. Dyer, J. Electrochem. Soc. 118, 957 (1971).

27. S. Mendelson, Acta. Met. 13, 555 (1965).

28. C.V. Hari Rao, H.E. Bates and K.V. Ravi, J. Appl. Phys. 47, 2614 (1976).

29. K.V. Ravi, H.B. Serreze, H.E. Bates, A.D. Morrison, D.N. Jewett and J.C.T. Ho, IEEE Photovoltaic Specialists Conference Record 11, 280 (1975).

30. A.K. Sood, G.M. Freedman, R.O. Bell, F.V. Wald, Presented at the Electrochemical Society Meeting, Washington, D.C., May 2 - 7 (1976) to be published in the Proceedings of the International Symposium on Solar Energy.

31. H.B. Serreze, J.C. Swartz, G. Entine and K.V. Ravi, Mat. Res. Bull. 9, 1421 (1976).

32. A.K. Sood, C.V. Hari Rao, H.E. Bates and K.V. Ravi, Recent News Paper No. 224, Spring Meeting of the Electrochemical Society, Toronto (1975).

33. C.J. Varker, T.E. Everhart and A.J. Gonzales, 2nd International Conference on Ion Beam Science and Technology, New York (1966) (Wiley, N.Y., 1966).

34. L.C. Garone, C.V. Hari Rao and K.V. Ravi, Mobil Tyco Solar Energy Corporation (unpublished research).

35. K.V. Ravi, C.J. Varker, C.E. Volk, J. Electrochem. Soc. 120, 533 (1973).

36. C.J. Varker and K.V. Ravi, J. Appl. Phys. 45, 272 (1974).

37. H. Menninger, H. Raidt and G. Voigt, Phys. Stat. Sol.(a) 35, 639 (1976).

38. J.C. Irvin, Bell System Tech. J., 41, 387 (1962).

APPENDICES

1. An Updated Program Plan

   Table VII, unchanged.

2. Man Hours and Costs

Previous man hours were 3976 and cost plus fixed fee was $142,659. Man hours for July plus August were 1269 and cost plus fee was $48,587. Man hours and cost for September are estimated to be 659 and $25,645 respectively. Therefore, third quarter man hours are estimated to be 1928 and cost plus fee to be $74,227. Cumulative three quarter man hours and cost plus fixed fee are estimated to be 5904 and $216,886, respectively.

3. Engineering Drawings and Sketches Generated during the Reporting Period

   Figures 47-53.

4. Summary of Characterization Data Generated during the Reporting Period

Spreading resistance data on ribbons grown from unpurified dies shows a large degree of scatter, whereas the use of purified dies results in a more uniform distribution of resistivity in the ribbons. Correlations have also been obtained among spreading resistance measurements, EBIC data and optical microscopy.

5. Action Items Required by JPL

   None

6. New Technology

   No reportable items of new technology.

   No cumulative new technology.

Table VII. Updated Program Plan

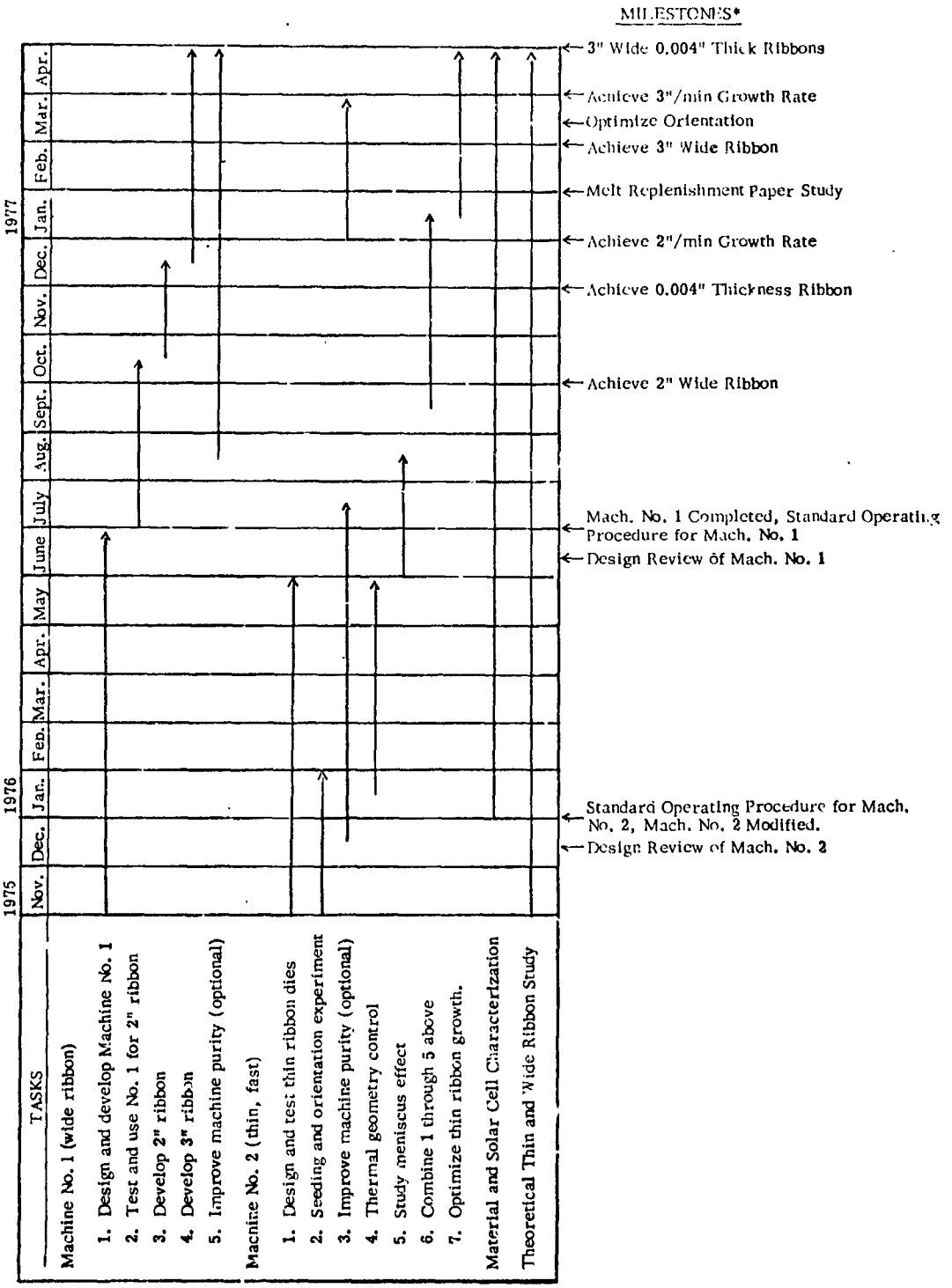

*Financial and Technical Reports Solar Cells and Samples will be delivered as per the Delivery Schedule of this contract.

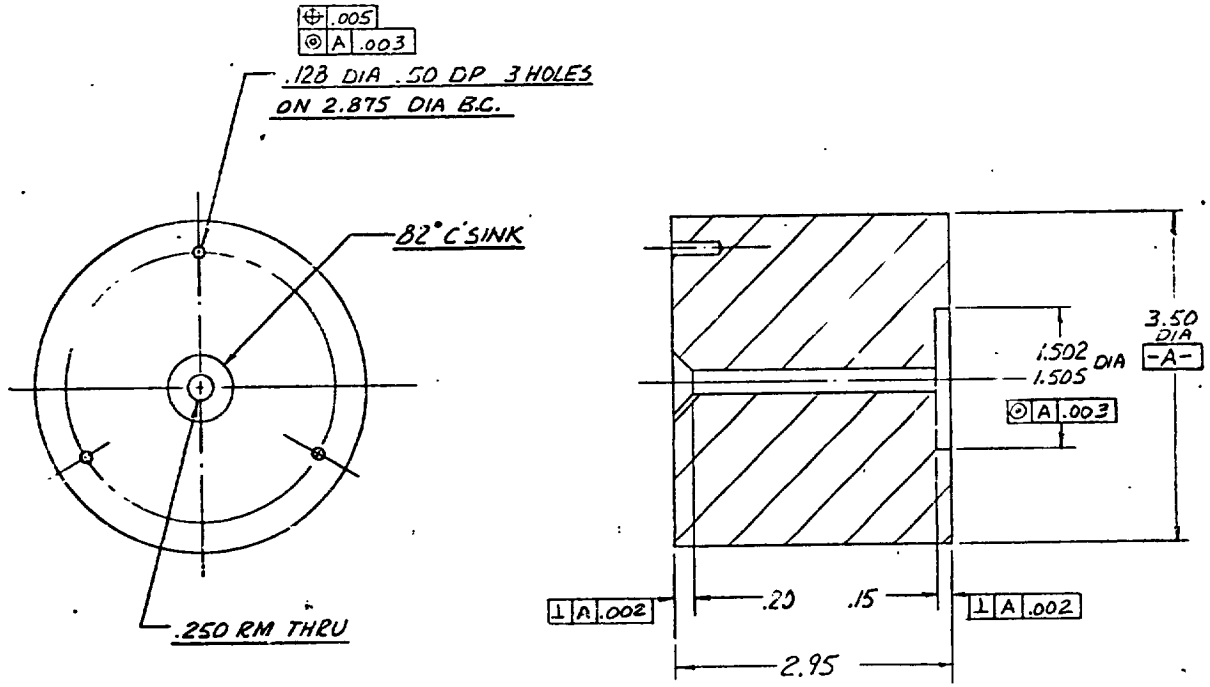

THESE DRAWINGS & SPECS ARE THE PROPERTY OF MOB'L TYCO SOLAR ENERGY CORP. & SHALL NOT BE REPRODUCED, COPIED OR USED AS THE BASIS FOR MANUFACTURE OR SALE OF APPARATUS WITHOUT EXPRESSELY WRITTEN AUTHORIZATION FROM MOBIL TYCO SOLAR ENERGY CORP.	UNLESS OTHERWISE SPECIFIED DIMENSIONS ARE IN INCHES TOLERANCES: ANGLES ± 1° · FRACTIONS ± 1/64 · 2 PLACE ± .010 · 3 PLACE ± .005 SURFACES: 63 √ MICRO-INCHES NEXT ASSEMBLY	DR C TAYLOR DATE 11-25-75 CHK APPD APPD APPLICABLE DOCUMENTS	Mobil Tyco Solar Energy Corporation PEDESTAL BASE
FINISH —"	MATERIAL: POCO GRAPHITE DFP-2	—	SIZE B · 10639 · REV SCALE 1-1 · SHEET 1 OF 1

Fig. 47. Pedestal Base.

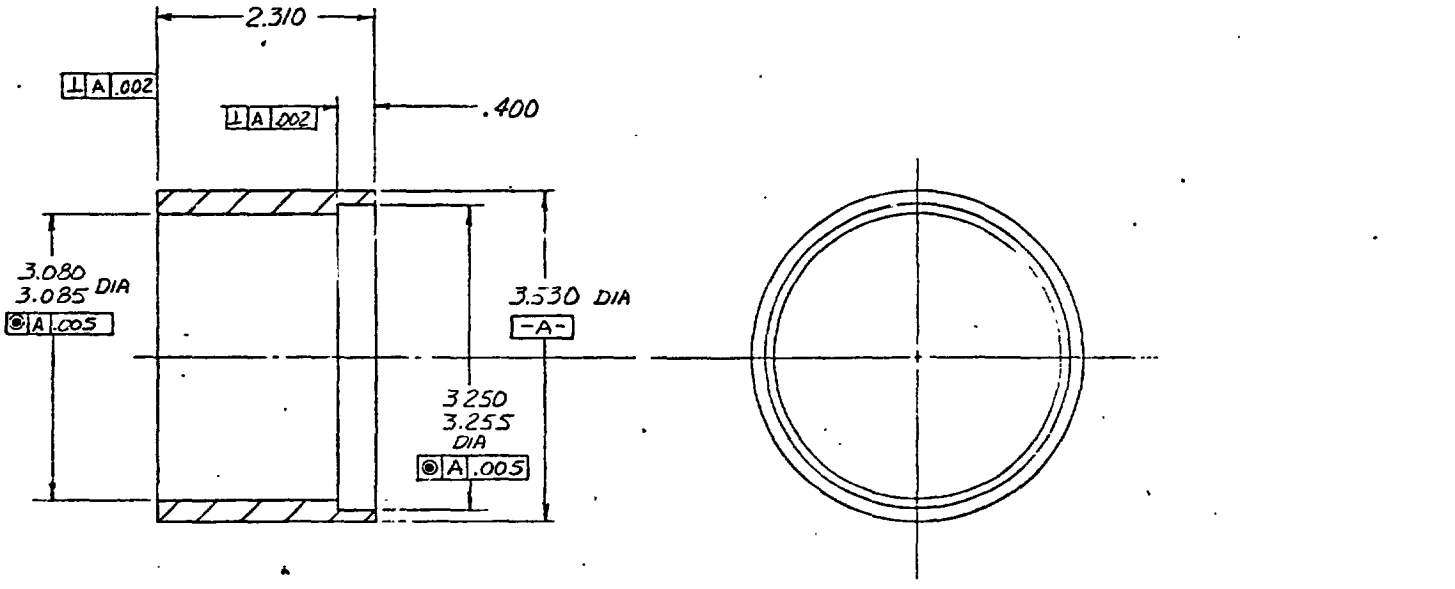

THESE DRAWINGS & SPECS ARE THE PROPERTY OF MOBIL TYCO SOLAR ENERGY CORP & SHALL NOT BE REPRODUCED, COPIED OR USED AS THE BASIS FOR MANUFACTURE OR SALE OF APPARATUS WITHOUT EXPRESSELY WRITTEN AUTHORIZATION FROM MOBIL TYCO SOLAR ENERGY CORP	UNLESS OTHERWISE SPECIFIED DIMENSIONS ARE IN INCHES TOLERANCES: ANGLES ±; FRACTIONS ± 1/64; 2 PLACE ± .010; 3 PLACE ± .005 SURFACES: 63 √ MICRO-INCHES NEXT ASSEMBLY	DR C TAYLOR 11-25-75 DATE CHK APPD APPD APPLICABLE DOCUMENTS	Mobil Tyco Solar Energy Corporation SUSCEPTOR SHELL
FINISH	MATERIAL: POCO GRAPHITE DFP-2		SIZE B 10640 RE SCALE 1-1 SHEET

Fig. 48. Susceptor Shell.

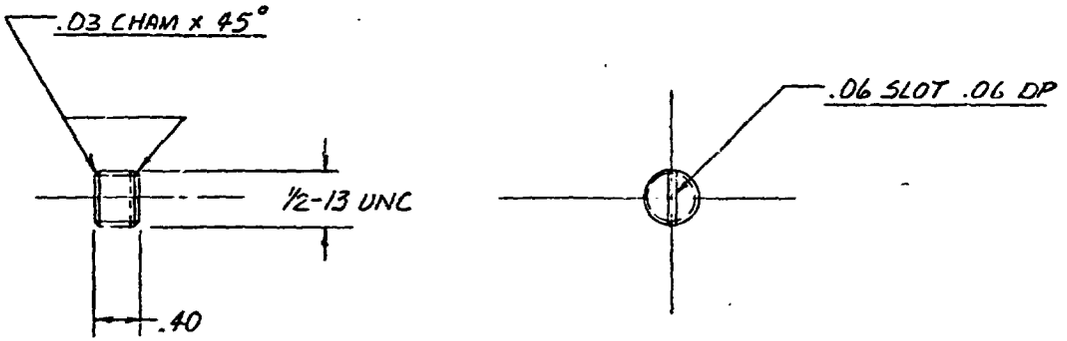

2 REQ'D

THESE DRAWINGS & SPECS ARE THE PROPERTY OF MOBIL TYCO SOLAR ENERGY CORP. & SHALL NOT BE REPRODUCED, COPIED OR USED AS THE BASIS FOR MANUFACTURE OR SALE OF APPARATUS WITHOUT EXPRESSELY WRITTEN AUTHORIZATION FROM MOBIL TYCO SOLAR ENERGY CORP.	UNLESS OTHERWISE SPECIFIED DIMENSIONS ARE IN INCHES TOLERANCES: ANGLES ±; FRACTIONS ±; 2 PLACE ±.010; 3 PLACE ±.005 SURFACES: 63 √ MICRO-INCHES NEXT ASSEMBLY	DR. TAK 2 11-20-75 DATE CHK APPD APPD APPLICABLE DOCUMENTS	Mobil Tyco Solar Energy Corporation DIE HOLDER PLUG
FINISH: ———	MATERIAL: POCO GRAPHITE DFP-2	———	SIZE B; 10641; REV SCALE 1-1; SHEET 1 OF

Fig. 49. Die Holder Plug

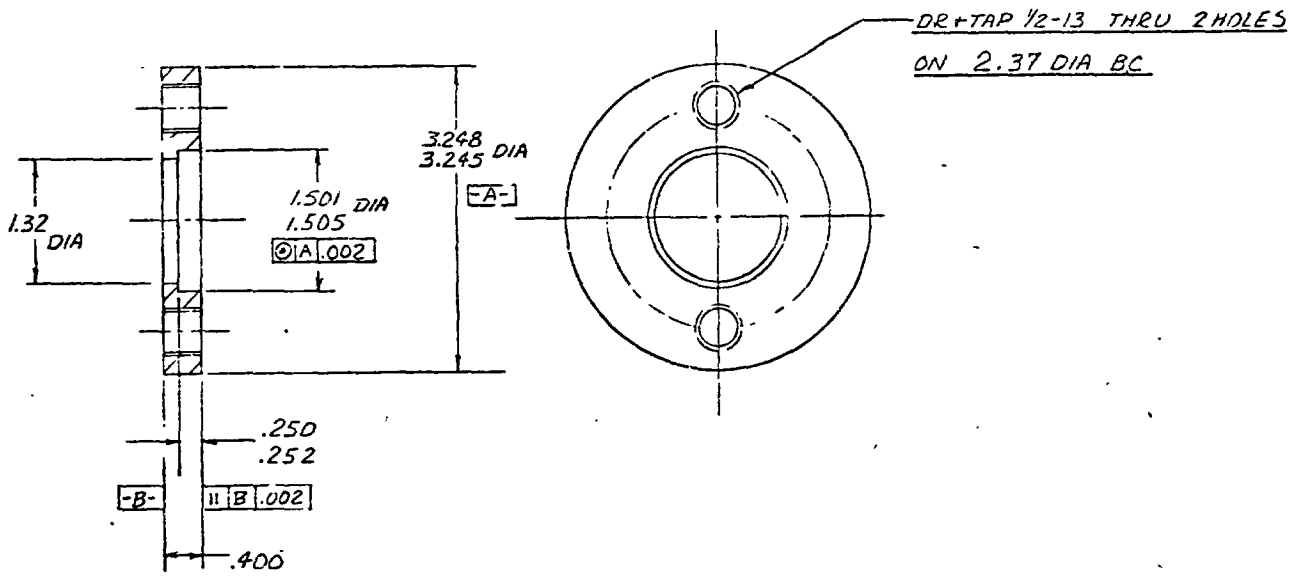

THESE DRAWINGS & SPECS ARE THE PROPERTY OF MOBIL TYCO SOLAR ENERGY CORP & SHALL NOT BE REPRODUCED, COPIED OR USED AS THE BASIS FOR MANUFACTURE OR SALE OF APPARATUS WITHOUT EXPRESSELY WRITTEN AUTHORIZATION FROM MOBIL TYCO SOLAR ENERGY CORP.	UNLESS OTHERWISE SPECIFIED DIMENSIONS ARE IN INCHES TOLERANCES: ANGLES ±, FRACTIONS ±, 2 PLACE ±.01, 3 PLACE ±.005 SURFACES: 63 √ MICRO-INCHES NEXT ASSEMBLY	DR C Tarr 1-20-75 DATE CHK APPD APPD APPLICABLE DOCUMENTS	Mobil Tyco Solar Energy Corporation DIE HOLDER SIZE B · 10642 · REV SCALE 1-1 · SHEET · OF
FINISH: ———	MATERIAL: POCO GRAPHITE DFP-2	———	

Fig. 50. Die Holder.

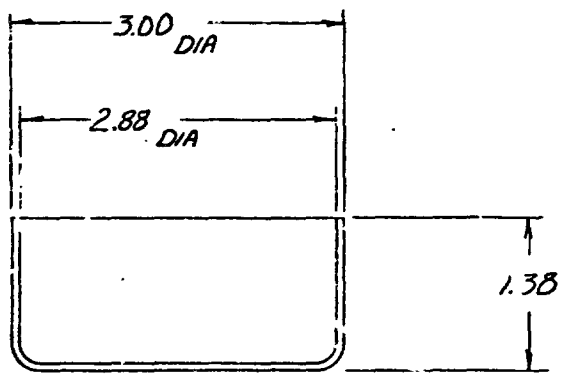

THESE DRAWINGS & SPECS ARE THE PROPERTY OF MOBIL TYCO SOLAR ENERGY CORP. & SHALL NOT BE REPRODUCED, COPIED OR USED AS THE BASIS FOR MANUFACTURE OR SALE OF APPARATUS WITHOUT EXPRESSELY WRITTEN AUTHORIZATION FROM MOBIL TYCO SOLAR ENERGY CORP.	UNLESS OTHERWISE SPECIFIED DIMENSIONS ARE IN INCHES TOLERANCES: ANGLES ±; FRACTIONS ± 1/64; 2 PLACE ± .020; 3 PLACE ± .005 SURFACES: √ MICRO-INCHES NEXT ASSEMBLY	DR C TAYLOR 11-25-75 DATE CHK APPD APPD APPLICABLE DOCUMENTS	Mobil Tyco Solar Energy Corporation QUARTZ CRUCIBLE (SHORT) SIZE B; 10651; REV SCALE —; SHEET OF
FINISH — MATERIAL QUARTZ			

Fig. 51. Quartz Crucible (short)

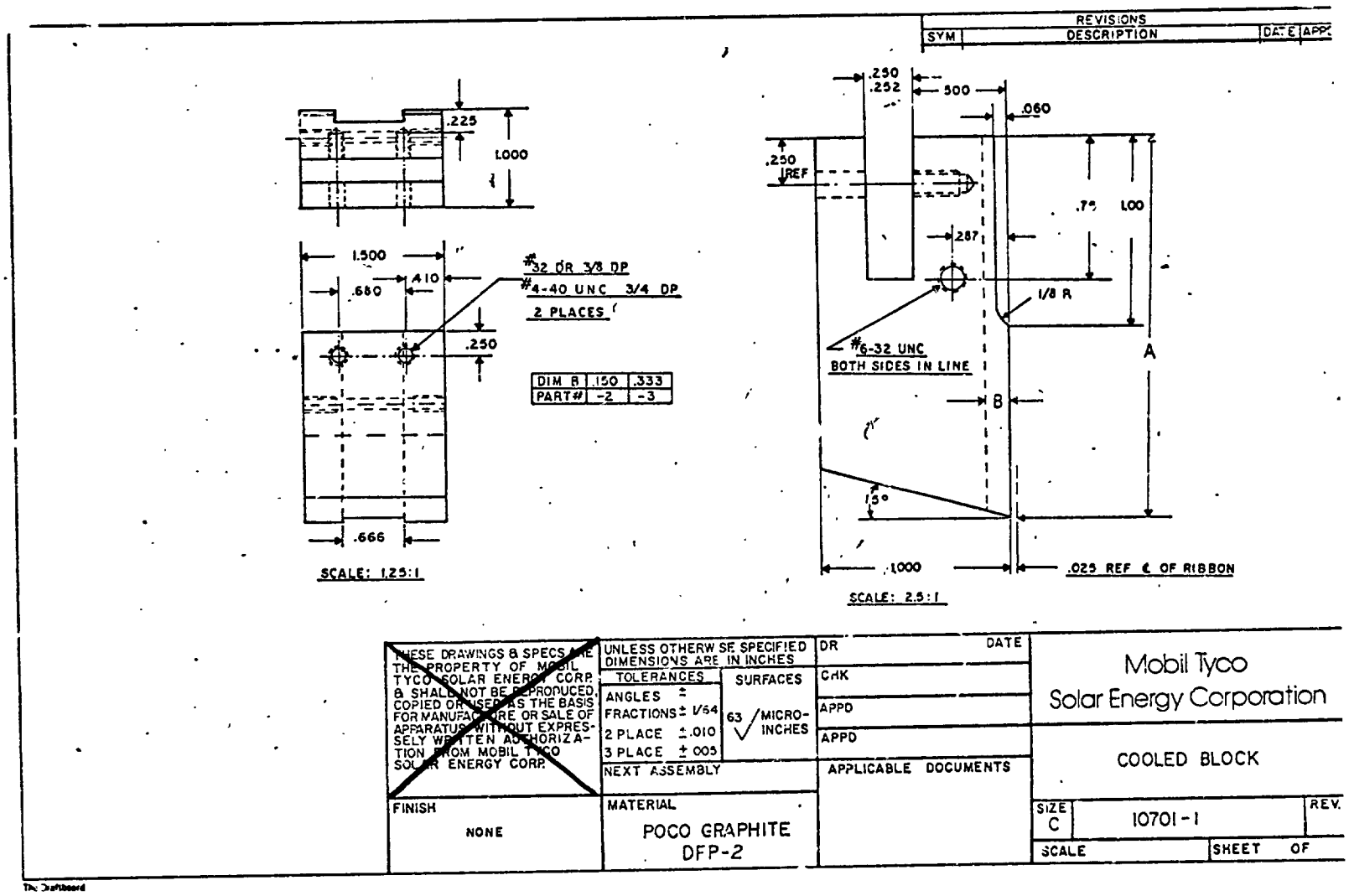

Fig. 52. Notched cold shoes.

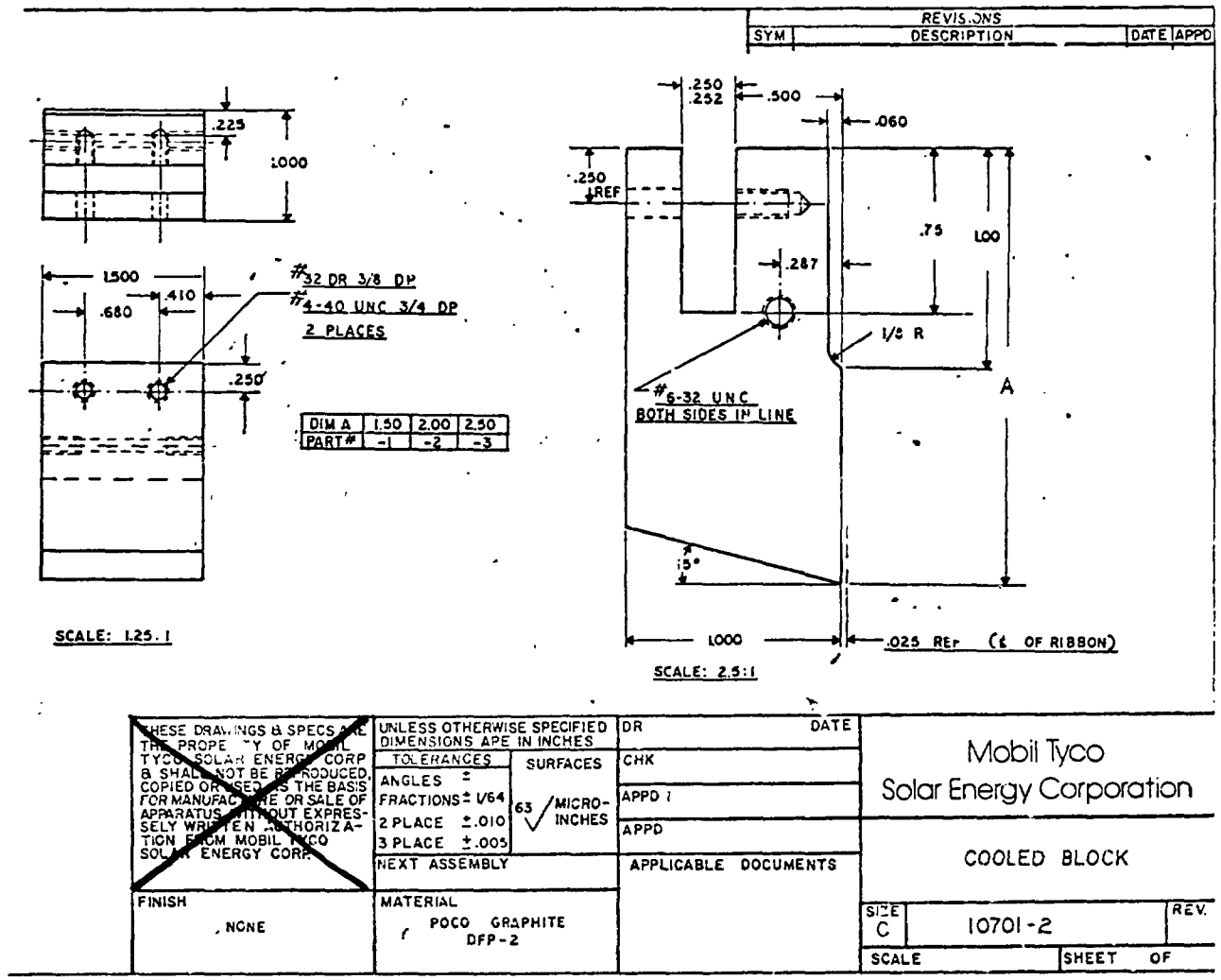

Fig. 53. Cooled graphite block (note 3 values of dimension A).